

Combination of the Virtual Magnet Method and Topology Optimization and its effects on embedded permanent magnet synchronous machine

**eingereicht an der Technischen Universität Wien
Fakultät für Elektrotechnik und Informationstechnik**

zur Erlangung des akademischen Grades

Master of Science

im Rahmen des Studiums Energie- und Automatisierungstechnik

unter der Leitung durch

Ass.-Prof. Andrea Roberto Insinga

DTU, Department of Energy Conversion and Storage

&

Univ.Prof. Dr.sc. Silvan Schmid

TU Wien, Institut für Elektrotechnik und Informationstechnik

Wien, im Juni 2023

Combination of Virtual Magnet Method and Topology Optimization and its effects on embedded permanent magnet synchronous machine

Master Thesis
June, 2023

By
Daniela Havlicek

Copyright: Reproduction of this publication in whole or in part must include the customary bibliographic citation, including author attribution, report title, etc.

Published by: DTU, Department of Energy Conversion and Storage, Anker Engelunds Vej, Building 301, 2800 Kgs. Lyngby Denmark
<https://www.energy.dtu.dk/>

Approval

I hereby declare that this master's thesis is entirely my own work. I have conducted the research, collected and analyzed the data, and written the content presented herein without any unauthorized external assistance or collaboration.

Daniela Havlicek - e1326298



.....
Signature

27. 6. 2023

.....
Date

Abstract

English

The aim of this thesis was to show that the combination of the Virtual Magnet Method and Topology Optimization Method can be applied together for different geometrical settings. It could be shown to use both for 2D geometries such as sextupole, quadrupole magnet, magnetic refrigeration and a simplified motor model, all using permanent magnets. Furthermore, the combined approach was used to demonstrate it works for more complex models. So it was applied on a partly existing COMSOL Multiphysics model of a 2D permanent magnet synchronous motor model, where it was used to design an own rotor model by using the combined approach. The torque and air gap flux density of the motor was analyzed, as well as their harmonics. Comparable results were achieved, compared to the original existing model of an embedded permanent magnet rotor. In conclusion, this opens possibilities to use this approach for more diverse analysis for permanent magnet optimization.

German

Das Ziel dieser Arbeit war es zu zeigen, dass die Kombination der Virtual Magnet Methode und der Topology-Optimierungsmethode für verschiedene geometrische Gegebenheiten zusammen angewendet werden kann. Es konnte gezeigt werden, dass beide für 2D-Geometrien wie Sextupol, Quadrupolmagnet, magnetische Kühlung und ein vereinfachtes Motormodell, die alle Permanentmagnete verwenden, verwendet werden können. Außerdem wurde der kombinierte Ansatz verwendet, um zu zeigen, dass er auch für komplexere Modelle funktioniert. So wurde er auf ein teilweise vorhandenes COMSOL Multiphysics-Modell eines 2D-Permanentmagnet-Synchronmotors angewandt, wo er zur Auslegung eines eigens designten Rotors unter Verwendung des kombinierten Ansatzes verwendet wurde. Es wurden das Drehmoment und die Luftspaltflussdichte des Motors sowie deren Oberschwingungen analysiert. Es wurden vergleichbare Ergebnisse erzielt, verglichen mit dem ursprünglichen Modell eines eingebetteten Permanentmagnet-Rotors. Dies eröffnet die Möglichkeit, diesen Ansatz für vielfältigere Analysen zur Optimierung von Permanentmagneten zu nutzen.

Acknowledgements

Andrea Roberto Insinga, Ass. Prof.

Supervisor from DTU, Denmark.

I would want to express my gratitude to Andrea Insinga for his support and exceptional mentorship throughout the completion of my thesis.

Schmid Silvan, Univ.Prof. Dr.sc.

Supervisor from TU Vienna.

I am immensely grateful to Silvan Schmid for his instrumental role in facilitating a successful collaboration between two universities, making this research possible.

I would like to express my gratitude to my family and friends for their unwavering support and encouragement, which have been a source of strength throughout my thesis process.

Contents

Preface	ii
Abstract	iii
Acknowledgements	iv
List of symbols	2
1 Introduction	2
1.1 Motivation and Problem definition	2
1.2 Previous Work and focus of the thesis	3
2 Theoretical Background	5
2.1 Maxwell Equations and Magnetostatic Relations	5
2.2 Material properties	12
3 Optimization Methods	17
3.1 Topology Optimization Method	17
3.2 Virtual Magnet Method - Continuous approach	18
3.3 Virtual Magnet Method - Segmented approach	20
3.4 Differences in methods	21
4 Optimization methods applied on simplified geometries	23
4.1 COMSOL Multiphysics - 2D modelling	23
4.2 Models of simplified geometries	28
5 Synchronous Machines	75
5.1 Permanent Magnet Synchronous Machines	76
5.2 Embedded Surface Mounted Permanent Magnet Synchronous Machines with COMSOL	78
6 Conclusion and Outlook	97
6.1 Limitations of the thesis	97
6.2 Conclusion	97
6.3 Outlook	98
Bibliography	101
List of figures	112
List of tables	112

List of Symbols

Abbreviations

MMA Method of Moving Asymptotes

RAMP Rational Approximation of Material Properties

RMS Route Mean Square

SIMP Solid Isotropic Material Penalization

THD Total Harmonic Distortion

TOM Topology Optimization Method

VMM Virtual Magnet Method

Coordinate symbols

d, q axes of rotor specific coordinate system

r, φ, z Cylindrical coordinate system

x, y, z cartesian coordinate system

Geometrical symbols

Λ integration area

Mathematical expressions

$\alpha[\mathbf{X}]$ functional of vector field \mathbf{X}

$\hat{\mathbf{X}}$ normalized vector

∇ divergence

\mathbf{X} vector

$\delta_{i,j}$ Kronecker Delta

$\langle \mathbf{X} \rangle$ average of vector \mathbf{X}

$\|\mathbf{X}\|$ vector norm

$\mathcal{H}(x)$ One-dimensional Heavyside function

\underline{X} complex parameter

$\underline{\underline{X}}$ tensor

\tilde{X} space vector

X scalar

Other symbols

ϕ magnetic flux

Θ magnetomotive force (MMF)

Ξ objective function for TOM

Physics constants

μ_0 vacuum permeability

c_0 vacuum speed of light

Scalars

χ magnetic susceptibility

δ air gap length between rotor and stator

\mathcal{M} Magnetic field strength relation, figure of merit

μ_r relative permeability

ω rotational speed

ρ charge density

ρ_s surface charge density

σ electrical conductivity

τ_p pole pitch

f electric frequency

l_d specific inductance in d - direction in dq coordinate system

l_q specific inductance in q - direction in dq coordinate system

n mechanical rotational speed

p number of pairs of poles

V_m magnetic scalar potential

Tensors

$\underline{\underline{\delta}}$ unit tensor

$\underline{\underline{p}}_{=el}$ Maxwell stress tensor

Vectors

\mathbf{A} magnetic vector potential

\mathbf{B}_r remanent magnetic flux density

\mathbf{B} magnetic flux density

\mathbf{D} electric flux density = displacement current density

\mathbf{E} electric field density

\mathbf{H}_c coercivity magnetic field strength

\mathbf{H} magnetic field strength

\mathbf{J}_s surface current density

\mathbf{J} current density

\mathbf{M}_s Saturation Magnetization

\mathbf{M} Magnetization

1 Introduction

1.1 Motivation and Problem definition

The importance of permanent magnets ranges from their use in industry, different applications of energy conversion and conservation. As many of them are reliant on the energy product of the magnets, which strongly depends on certain characteristics of the magnets, there is a strong interest in investigation of optimized permanent magnets and researching for improved versions.

First mentions of magnetic materials was the so-called lodestone, basically consisting out of magnetite, Fe_3O_2 . In its natural appearance, it shows a magnetic state. This stone was used in the ancient days to magnetise iron needles, mainly used for compasses, which was the first reported use of artificially created magnets.

William Gilbert started reporting three different ways of producing artificial magnets, starting in the 17th century, followed by Sturgeon in the 19th century, who invented electromagnets. He showed through experiments with different alloys that their properties are reasoned not only by their constituents' properties. Further investigations of magnetic materials were made in Japan, as well as Germany and England. Heusler discovered alloys, which appeared to show better properties than magnets at this time, therefore named Heusler alloys. Japanese scientists Takei and Kato invented magnets out of powdered oxides, which can be seen as vanguards of ferrite nowadays [1].

There are growing appeals for increasing the energy product, already started in the 20th century with upcoming new forms of permanent magnets such as *ferrite* or *rare-earth intermetallic compounds*. The increasing value of energy product as well as ratio between coercivity and magnetism lead to new applications using permanent magnets such as actuators, electric motors and electromechanical accessories [2].

According to [3], permanent magnet applications can be split up into groups of static or dynamic behaviour, depending on if the working point in the second quadrant of the hysteresis loop is moving or fixed at a certain point. E.g. for uniform fields with static working point magnets are used for Magnetic Resonance Imaging or alignment of magnetic powder. If the field is nonuniform within a static point, then it can be used for e.g. beam control or radiation sources. For dynamic working points and e.g. time varying fields, magnetometers use this effect [3]. Certain limits are then set in terms of coercivity for the specific magnet material, but as well depending on the specific application, a certain geometry is required [3].

For the several mentioned applications, permanent magnets need to show their magnetic effect in order to make the application work properly. The foremost problem is the fact that those magnets play an immense part of the performance as well of the costs of the whole application. For instance, as mentioned in [2], producing thin film permanent magnets for e.g. permanent magnet synchronous machines is conflicting as the main part of the permanent magnets within the rotor is to guide the flux into the air gap and then the stator. This is however only possible when the magnets has a certain thickness compared to the lateral dimensions of the magnetic system.

Another main limitation would be the working temperature of e.g. NdFeB and ferrite that have high remanence values and which collides with the temperature requirements of some induction motors. Therefore, a switch for some applications is made to other

high temperature SmCo types [3]. In terms of compactness, temperature resistance and acoustics, permanent magnets need to fulfill as well more requirements when it comes to electric automobiles [3].

As demonstrated in [4], permanent magnets were increasing in demand within the years of 2005 until 2020, although the regression of 2009 until 2011, higher demand was denoted as more renewable energy resources were build. For instance, expanding amount of wind power plants, high efficiency motors, electric bikes or air conditioning. Higher demand of rare earth elements that occur in permanent magnets raised the prices, as the it exceeded the availability of it. The global magnet market in terms of use and cost focuses on hard ferrite and NdFeB magnets. As [4] forecasts, the demand for 2030 of NdFeB magnets will double the amount that is used in 2020. This big increase lead to questions of supply guarantee, but as well the huge dependency of the magnet market in China for global output, as still 80% of rare earth magnets such as NdFeB magnets are expended from there. A large number of alternative approaches have been investigated over the last two decades to overcome this problem.

This thesis should contribute to a sustainable and more efficient way of analysing permanent magnet shape, especially for areas of wind energy turbine motors or motors used for electric vehicles.

1.2 Previous Work and focus of the thesis

Already in [2], ideas where mentioned of using *exchange spring magnets*, having recoil curves with high permeability and achieving almost remanence point for back loop, to have a beneficial ratio of cost to performance of the magnet, as the amount of rare earth magnet is reduced.

Only a few studies have shown that the Virtual Magnet Method can be applied on simplified geometries, especially magnetic refrigeration, like in [5], [6]. No study to date has examined this method applied on applications like quadrupole or sextupole magnets, as well as more complex models like permanent magnet synchronous machines. Using Topology Optimization Method, in [7] it has been applied for a specific machine type, however not in combination with the Virtual Magnet Method. In particular, no study has shown that both methods can be combined, only a comparison within the two methods has been presented in [8], and this combination applied on more complex models has also not been yielded.

This thesis considers the field of combining the Virtual Magnet Method and Topology Optimization Method as the main subject of its study. Therefore, it deals with applying both on permanent magnets for different use cases. In comparison to other techniques used so far it has the big advantage of combining the strengths of both methods in order to get a more precise output than by applying only one of the methods. One practical advantage of the method is that it can be used for any suitable geometrical application, even if the composition of it is more complex, as used in chapter 5 for Permanent Magnet Synchronous machines, there is the possibility to break the geometry down to more easy sub-parts and apply the combined approach on it. It has as well significant benefits in expanding and varying the methods to have several possible combinations depending on the main optimization goal. This gives rise to a broad field of future possible optimization possibilities, as it is decoupled from specific material use as well.

2 Theoretical Background

This chapter will provide the basic physical laws that build the basis for the following investigations and to understand and interpret the results properly.

2.1 Maxwell Equations and Magnetostatic Relations

The most common form of the Maxwell's equations is the differential, local form, presented by equation 2.1a until 2.1d [9]:

$$\nabla \times \mathbf{E} = -\frac{\partial \mathbf{B}}{\partial t} \quad (2.1a)$$

$$\nabla \cdot \mathbf{B} = 0 \quad (2.1b)$$

$$\nabla \times \mathbf{H} = \mathbf{J} + \frac{\partial \mathbf{D}}{\partial t} \quad (2.1c)$$

$$\nabla \cdot \mathbf{D} = \rho \quad (2.1d)$$

$$\nabla \cdot \mathbf{J} = -\frac{\partial \rho}{\partial t} \quad (2.1e)$$

Faraday's Law, defined by equation 2.1a, combines the curl of the electric field with the negative time derivative of the magnetic flux density. Equation 2.1d is named *Gauss's Law*, saying that the divergence of the electric flux density equals to the charge density. The *Ampere-Maxwell Law* is expressed by equation 2.1c, showing that the curl of the magnetic field strength is equal to the current density and the additive term of displacement current density, which was added by Maxwell to include non-stationary cases in this equation [9]. Equation 2.1b defines that magnetic charges do not exist, so that the divergence of the magnetic flux density is equal to zero. Therefore, this equation is often expressed as *Magnetic Charge Absence* [9], [10].

The local Maxwell equations for magnetostatics are stated here, especially relevant for chapter 4 [9]:

$$\nabla \times \mathbf{E} = \mathbf{0} \quad (2.2a)$$

$$\nabla \cdot \mathbf{B} = 0 \quad (2.2b)$$

$$\nabla \times \mathbf{H} = \mathbf{J} \quad (2.2c)$$

$$\nabla \cdot \mathbf{D} = \rho \quad (2.2d)$$

The linear constitutive relations, expressed as:

$$\mathbf{D} = \epsilon_0 \epsilon_r \mathbf{E} \quad (2.3a)$$

$$\mathbf{B} = \mu_0 \mu_r \mathbf{H} \quad (2.3b)$$

serve to draw the connection between the two pairs of fields, \mathbf{E} and \mathbf{B} as well as \mathbf{H} and \mathbf{D} , in order to define a physical dynamic system including interpretations for energy and momentum [9], [11].

Using the relations explained in this chapter, the following will combine them to define field conditions on the edges of two different materials.

2.1.1 Boundary conditions

Assuming that the surface between two materials with diverse relative permeabilities can be expressed by applying Stoke's Theorem on equation 2.1c and Gauss's Theorem on equation 2.1b, resulting in boundary conditions for H_t and B_n as follows, assuming that 1 and 2 stands for material 1 with permeability μ_{r1} and material 2 with permeability μ_{r2} respectively. The indexed t and n stands for the tangential and normal components of the corresponding vectors, \hat{s} defines the normalized tangential vector and \hat{n} the normalized normal vector to each of the boundaries, illustrated in figure 2.1 and expressed in equations 2.4 for the magnetic field strength and 2.5 for the magnetic flux density [9], [12].

$$\int_{\partial A'} \mathbf{H} \cdot \hat{s} \, ds = \int_{A'} \mathbf{J} \cdot \hat{n} \, dA' \quad (2.4a)$$

$$\mathbf{H}_{2t} - \mathbf{H}_{1t} = -\mathbf{K}_m \quad (2.4b)$$

, where \mathbf{K}_m serves as the surface current density [12].

$$\int_A \mathbf{B} \cdot \hat{n} \, dA = 0 \quad (2.5a)$$

$$\mathbf{B}_{2n} - \mathbf{B}_{1n} = 0 \quad (2.5b)$$

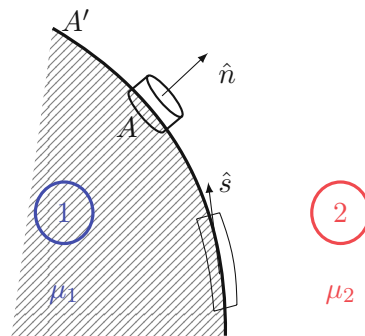


Figure 2.1: Cylinder with surface area A and normal vector \hat{n} defines the boundary conditions for B , the bottom rectangle for H with the perpendicular vector \hat{s} [13]

Magnetic vector and scalar potential

For magnetostatics, two main laws exist, mentioned in equation 2.2c and 2.2b. In order to solve them, magnetic potentials can be defined. If no currents exist, then the magnetic scalar potential V_m can be used, however if there are currents, then the magnetic vector potential A needs to be used [13]. As the virtual magnet method does not work for existing currents, those specifications without currents are considered afterwards.

The magnetic scalar potential V_m , defined in equation 2.6a and illustrated in figure 2.2, can be used to express the magnetic field strength through a scalar field. First of all, it

needs to fulfill equation 2.2b, see equation 2.6b, with respect to the constitutive relation in 2.26, explained in more detail in chapter 2.2.1. Equation 2.6d can be especially defined as magnetic charge density [13].

$$\mathbf{H} = -\nabla V_m \quad (2.6a)$$

$$\nabla \cdot \mathbf{B} = 0 = \nabla \cdot (-\mu_0 \nabla V_m) \quad (2.6b)$$

$$\nabla \cdot (\mu_0 \nabla V_m) = \mu_0 \nabla \cdot \mathbf{M} \quad (2.6c)$$

$$-\nabla \cdot \mathbf{M} = \rho_m \quad (2.6d)$$

$$\hat{\mathbf{n}} \cdot \mathbf{M} = \sigma_m \quad (2.6e)$$

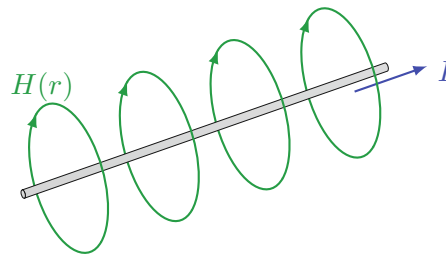


Figure 2.2: Example for an irrotational field \mathbf{H} caused by the direct current I , depending on the distance vector r from the wire. Figure adapted from [14] and [15].

The second requirement is fulfilling Ampere's Law 2.2c with the scalar potential, however assuming to have no currents, so $\mathbf{J} = \mathbf{0}$, as seen in equation set 2.7. This is automatically fulfilled as the curl of a gradient field is always zero [14].

$$\nabla \times \mathbf{H} = \mathbf{0} = \nabla \times (-\nabla V_m) \quad (2.7)$$

In order to define the vortex field \mathbf{B} through another vector field \mathbf{A} , the magnetic vector potential, shown in equation 2.8a, the expression needs to fulfill the same two equations like mentioned for the scalar potential before [16]. The relation states that the vortex field \mathbf{B} can be defined as the vortex density of \mathbf{A} . The curl of \mathbf{A} is used in equation 2.8b, applied for equation 2.2b, and illustrated in figure 2.3, including the direct validity of this relation, as the divergence of a vortex field is always zero, implying solenoidality of the magnetic field [14].

$$\mathbf{B} = \nabla \times \mathbf{A} \quad (2.8a)$$

$$\nabla \cdot \mathbf{B} = 0 = \nabla \cdot (\nabla \times \mathbf{A}) \quad (2.8b)$$

The second equation 2.2c to be satisfied with equation 2.8a is expressed in 2.9a, including again the constitutive relation 2.26. Equation 2.9c defines the curl of the magnetisation as the magnetic current density \mathbf{J}_m , which appears in the macroscopic observation of the magnetic field. Furthermore, equation 2.9d expresses the surface current density \mathbf{K}_m . Latter specifically is needed to describe fields caused by permanent magnets, as it states that for volumes with random shape, \mathbf{K}_m defined on a surface of a volume equals the uniformly magnetisation within this volume [13].

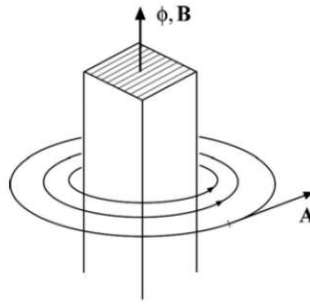


Figure 2.3: Schematic figure for representing the magnetic vector potential A and the relation to the vector field B [14].

$$\nabla \times \mathbf{H} = \mathbf{J} = \nabla \times \frac{1}{\mu_0} (\nabla \times \mathbf{A}) \quad (2.9a)$$

$$\nabla \times \frac{1}{\mu_0} (\nabla \times \mathbf{A}) = \mathbf{J} + \nabla \times \mathbf{M} \quad (2.9b)$$

$$\nabla \times \mathbf{M} = \mathbf{J}_m \quad (2.9c)$$

$$\mathbf{M} \times \hat{\mathbf{n}} = \mathbf{K}_m \quad (2.9d)$$

Relation between magnetic potential definition and boundary conditions

In most cases to define boundary conditions for electro- or magnetostatics, the Poisson's equation is used. This one was mentioned in equation 2.6c and approximately suitable for equation 2.9b, as they both show the *source* on the right-hand side which causes the magnetic field. The Laplace equation would then be the trivial solution zero, so the homogeneous solution [14].

If the boundary has a defined potential, then it is either 0, so a homogeneous boundary condition, or it is unequal to 0, then named *Dirichlet* boundary condition. The third version can be expressed as the change of the potential at the boundary, called *Neumann* boundary condition [14]. As for the virtual magnet method only the definition of the magnetic scalar potential can be applied, therefore the boundary conditions are expressed now with V_m . For both above mentioned boundary conditions, Dirichlet and Neumann, can be revealed through both potential definitions [17]. By using the magnetic scalar potential for current-free regions, the curl-free state of \mathbf{H} , or having no magnetomotive force along any curve within an idealised magnetic body, they represent constant magnetic potential within this area, so they need to be current-free inside. The surface of such a body can be defined as a perfect magnetic conductor, as it serves as an equipotential surface, like the one of iron [11].

2.1.2 Poynting's Theorem and related energy aspects

Lenz's Law builds the basis of interaction when a magnetic field which changes induces electric current into a conductor, who then counteracts to this applied magnetic field, so the conductor tries to manipulate the induced magnetic field [12].

The Lorentz Force, which can be an outcome of the Lenz Law, can be expressed as follows [10]:

$$\frac{\mathbf{F}}{q} = \mathbf{E} + \mathbf{v} \times \mathbf{B} = \mathbf{E}' \quad (2.10)$$

, saying the relation between the velocity v of a point mass with its charge q , resulting in a force applied on that mass particle. Here it is stated as the force related to the charge, in order to define an electric field \mathbf{E}' , which defines the right-hand side of the equation. It means that this field would be seen from an observing system moving with the geometry. Therefore, this field expression can be inserted in the following equation

$$\mathbf{J} = \sigma(\mathbf{E} + \mathbf{v} \times \mathbf{B}) + \mathbf{J}_e \quad (2.11)$$

, meaning that the current density \mathbf{J} consists of an external applied current density \mathbf{J}_e and \mathbf{E}' which represents the field that causes the force on the charged particle from equation 2.11 [18].

In respect of the detailed analysis of permanent magnet synchronous machine types in chapter 5, the origin of the resulting torque will be derived here from the force densities and the Maxwell stress tensor expression.

Considering the work which is done by the Lorentz force term in 2.10, then it results in

$$dW = dq(\mathbf{E} + \mathbf{v} \times \mathbf{B}) \cdot d\mathbf{l} = dq(\mathbf{E} + \mathbf{v} \times \mathbf{B}) \cdot \mathbf{v} dt \quad (2.12)$$

$d\mathbf{l}$ would define a distance of the displaced charge dq with its velocity v within the volume Λ . The change of energy of the charge within a certain volume Λ and exchanging expressions of dq with ρd^3r leads to the integral over the volume [19]:

$$\frac{dW}{dt} = \int_{\Lambda} (\mathbf{E} + \mathbf{v} \times \mathbf{B}) \cdot \mathbf{v} \rho d^3r = \int_{\Lambda} (\mathbf{E} \cdot \mathbf{J}) d^3r \quad (2.13)$$

, using the relation of 2.10 to express the integrand with \mathbf{J} . By replacing exactly the current density by the Ampere's Law in 2.1c, then it results in [19]

$$\mathbf{E} \cdot \mathbf{J} = \mathbf{E} \cdot \left(\frac{1}{\mu_0} (\nabla \times \mathbf{B}) - \epsilon_0 \frac{\partial \mathbf{E}}{\partial t} \right) \quad (2.14a)$$

$$\mathbf{E} \cdot \mathbf{J} = -\frac{1}{2} \frac{\partial}{\partial t} (\epsilon_0 \mathbf{E}^2 + \frac{\mathbf{B}^2}{\mu_0}) - \nabla \cdot \frac{\mathbf{E} \times \mathbf{B}}{\mu_0} \quad (2.14b)$$

Inserting expression 2.14b into the work integral, and using the divergence theorem which basically relates a volume integral of a divergence to a surface integral, it leads to [19], [11]:

$$\int_{\Lambda} (\mathbf{E} \cdot \mathbf{J}) d^3r = -\frac{d}{dt} \int_{\Lambda} \frac{1}{2} (\epsilon_0 \mathbf{E}^2 + \frac{\mathbf{B}^2}{\mu_0}) d^3r - \int_{d\Lambda} \left(\frac{\mathbf{E} \times \mathbf{B}}{\mu_0} \right) d\Lambda \quad (2.15)$$

If the minus sign would be placed on the left side of the equation, it would be immediately evident that this volume integral defines the *Joule losses*, also called energy losses, as power flows out of the electromagnetic system within the volume Λ . The expression in 2.15 is called the Poynting's Theorem, defining the energy conservation generalised for an electromagnetic system. Especially the second surface integral on the right side of the equation includes an expression which is named *Poynting vector*, usually defined as

$$\mathbf{S} = \frac{\mathbf{E} \times \mathbf{B}}{\mu_0} = \mathbf{E} \times \mathbf{H} \quad (2.16)$$

, therefore the surface integral expression of \mathbf{S} can be explained as the energy flux which comes out of the observed volume, so the rate of energy change through the surface of Λ [19], [11].

By taking equation 2.12 and changing it to, with respect to the index m as the material subsystem and el as the electromagnetic subsystem, :

$$f_m = -f_{el} = \rho_{el}(\mathbf{E} + \mathbf{J}_{el} \times \mathbf{B}) \quad (2.17)$$

, one can modify it further by inserting \mathbf{J}_{el} , the modified Ampere's Law 2.1c, ρ_{el} as the modified Gauss's Law 2.1d, modified Faraday's Law 2.1a and a vector identity for vector field \mathbf{f}

$$\mathbf{J}_{el} = \frac{1}{\mu_0} \nabla \times \mathbf{B} - \epsilon_0 \partial_t \mathbf{E} \quad (2.18a)$$

$$\rho_{el} = \epsilon_0 \nabla \cdot \mathbf{E} \quad (2.18b)$$

$$\nabla \times \mathbf{E} + \partial_t \mathbf{B} = \mathbf{0} \quad (2.18c)$$

$$\mathbf{f} \times (\nabla \times \mathbf{f}) - \mathbf{f}(\nabla \cdot \mathbf{f}) = \nabla \cdot \left(\frac{1}{2} f^2 \underline{\underline{\delta}} - \mathbf{f} \otimes \mathbf{f} \right) \quad (2.18d)$$

in order to get the following, including the definition for $\underline{\underline{\delta}}$ as the unit tensor, Kronecker Delta, and using the magnetic charge free statement 2.1b:

$$f_{el} = \partial_t(\epsilon_0 \mathbf{E} \times \mathbf{B}) + \nabla \cdot \left[\left(\frac{\epsilon_0}{2} E^2 + \frac{1}{2\mu_0} B^2 \right) \underline{\underline{\delta}} - \epsilon_0 \mathbf{E} \otimes \mathbf{E} - \frac{1}{\mu_0} \mathbf{B} \otimes \mathbf{B} \right] \quad (2.19a)$$

$$w_{el} = \frac{\epsilon_0}{2} E^2 + \frac{1}{2\mu_0} B^2 \quad (2.19b)$$

$$\underline{\underline{p}}_{el} = w_{el} \underline{\underline{\delta}} - \epsilon_0 \mathbf{E} \otimes \mathbf{E} - \frac{1}{\mu_0} \mathbf{B} \otimes \mathbf{B} \quad (2.19c)$$

From the version in 2.19a, one part can be abbreviated to 2.19c, named as *momentum flux density*, more precisely as in general the negative signed version as *Maxwell stress tensor*, containing the energy density expression 2.19b [11], [19], [20].

The Maxwell stress tensor can now be used to define the related torque within an electromagnetic system related to a point \mathcal{P} [20],[11], [19]:

$$T(\mathcal{P}) = \int_{dV} (r_{\mathcal{P}} \times f_{el}) dA \quad (2.20a)$$

$$T(\mathcal{P})_{mag} = \int_{dV} \frac{1}{\mu_0} r_{\mathcal{P}} \times (\mathbf{n} \cdot \mathbf{B} \mathbf{B} - \frac{1}{2} B^2 \mathbf{n}) dA \quad (2.20b)$$

With those mentioned definitions in 2.20, especially 2.20b for dominant magnetic systems, a proper reference can be made in chapter 5 to explain mechanical effects caused in the machine by the electromagnetic field.

2.1.3 Multipole Expansion for analysing Quadrupole and Sextupole fields

In order to understand chapter 4.1.3, this subchapter should provide a brief description of how quadrupole and sextupole fields are analysed.

Assuming to have a magnetic field $\mathbf{B} = (B_x, B_y, B_z)$, with respect to the three Cartesian coordinates x, y, z , regarding B_z as constant, then the other two components can be defined with complex numbers as [21]:

$$B_y + iB_x = C_n \cdot (x + iy)^{n-1} \quad (2.21a)$$

$$n = 1, 2, 3... \quad (2.21b)$$

$$B_y + iB_x = B_{ref} \cdot \sum_{n=1}^{\infty} (a_n + ib_n) \cdot \left(\frac{x + iy}{R_{ref}}\right)^{n-1} \quad (2.21c)$$

The first equation above states that the magnetic field density can be split up into a real and imaginary part, as well expressed by the right-hand side with the complex factor C_n , that needs to satisfy $div\mathbf{B} = 0$, as well as $curl\mathbf{B} = \mathbf{0}$, like mentioned in 2.1b and 2.1c, with respect to zero current density, so assuming to have a charge- and current-free space, in order to be a valid solution for the maxwell equations.

This factor can serve, if expressing equation 2.21a within a sum expression, as a scaling factor of how intense the specific observed field occurs, however only considering the chosen n expression [21].

The exponent and index n expresses different fields: $n = 1$ defines a dipole field, $n = 2$ a quadrupole and $n = 3$ a sextupole expression. Depending on when to specify the parameters a_n and b_n , the reference values, reference radius R_{ref} and a reference field B_{ref} , need to be determined as well [21].

Out of the mentioned expressions, the derivative for the non-screwed version in 2.22a and the screwed version in 2.22b is shown as:

$$\frac{\partial^{n-1} B_y}{\partial x^{n-1}} = (n-1)! \frac{B_{ref}}{R_{ref}^{n-1}} \cdot a_n \quad (2.22a)$$

$$\frac{\partial^{n-1} B_x}{\partial x^{n-1}} = (n-1)! \frac{B_{ref}}{R_{ref}^{n-1}} \cdot b_n \quad (2.22b)$$

The quadrupole field can be expressed by two components, one for each direction in the two-dimensional space. If Cartesian coordinates are considered, the x and y component are individually composed [22]:

$$2 \cdot x \cdot y = \pm r^2 \quad (2.23a)$$

$$B_x = a_2 \cdot y \quad (2.23b)$$

$$B_y = a_2 \cdot x \quad (2.23c)$$

The horizontal focus works simultaneously reducing the focusing in the other direction. An ideal quadrupole shows the hyperbolic contours, as can be seen in equation 2.23a,

not screwed, including r as the aperture radius here. For the individual axes x and y , the equations below show that they do not depend from each other, including the scaling factor a_2 for quadrupoles. Considering the possible harmonics appear with $2 * n$, with respect that $n = 2, 6, 10, 14...$ [22]. A similar explanation can be made for the sextupole field for a sextupole magnet, in the non-screwed way:

$$3 \cdot x^2 \cdot y - y^3 = \pm r^3 \quad (2.24a)$$

$$B_x = a_3 \cdot (xy) \quad (2.24b)$$

$$B_y = a_3 \cdot (x^2 - y^2) \quad (2.24c)$$

In this case, the field expression in equation 2.24c is not independent of direction, therefore as well called non-linear elements, compared to the before mentioned quadrupole magnet, which behaves linearly. The field varies quadratically from the distance of the center, including the scaling factor a_3 for sextupoles. With respect to the occurring harmonics, here the following can appear: $n = 3, 9, 15, 21, \dots$, again showing the $2n$ characteristic [22].

2.2 Material properties

2.2.1 Constitutive relations and hysteresis behaviour

Equation 2.3b expresses the relation between the magnetic flux density and the magnetic field strength, with relative permeability indicated by μ_r and vacuum permeability by μ_0 . The fields B and H are in the following relation with the magnetisation M [23]:

$$B = \mu_0(H + M) \quad (2.25)$$

, or in another way expressed as:

$$H = \frac{1}{\mu_0} B - M \quad (2.26)$$

The occurrence of the magnetisation, M , is caused by the atomic change of current density due to an external magnetic field B [9]. Therefore, the relation between the magnetization and the magnetic field strength can be expressed as follows [23]:

$$\chi \cdot H = M \quad (2.27a)$$

$$\chi = \mu_r - 1 \quad (2.27b)$$

Equation 2.27b relates the magnetic susceptibility χ with the relative permeability μ_r . The above relations assume isotropic magnetic behavior. Therefore B , H and M are all parallel to each other, and μ_r , μ and χ are scalars [23].

However, if the material is anisotropic, the equation needs to be modified using the permeability tensor $\underline{\underline{\mu}}$ [11, 5]:

$$B = \underline{\underline{\mu}} \cdot H + B_r \quad (2.28)$$

The equation above includes the remanent flux density, B_r , which is only non zero for permanent magnets. If the magnetisation is approximately constant over the relevant range of values of H , then it results in $\mu_0 M \approx B_r$ [24]. This is discussed in detail in chapter 2.2.3.

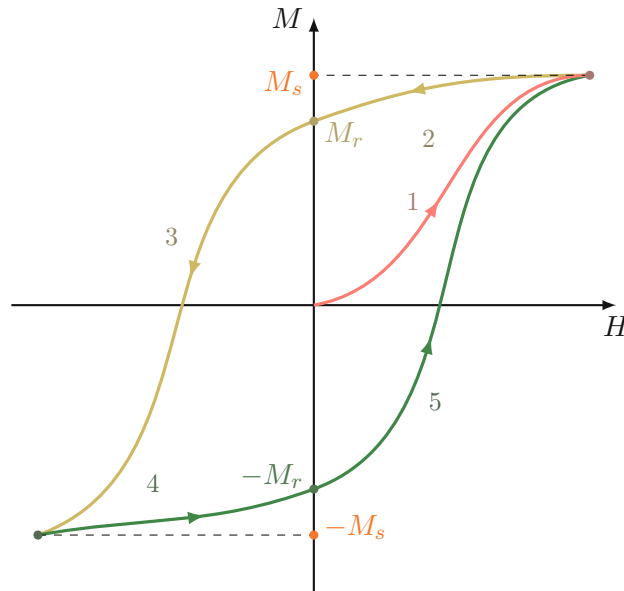


Figure 2.4: Schematic figure of MH curve and significant marks, adaption from figure in [23], [25]

Figure 2.4 shows an idealised hysteresis curve with the relation of M over H . Before explaining the exact parts of this curve, the expression *Bloch-walls* describe the boundary between two spontaneously magnetized areas with different orientation [23].

For the innermost part of the orange curve, also named as initial magnetisation, reversible Bloch-wall movements still exist. The following, more steep path of the initial curve already includes non-reversible wall movements. If the H field is more increased, the curve shows again reversible wall movements, and then tends to reach the saturation point, also defined with the saturation magnetisation M_s . From this point on, reducing the field strength again, leads to another curve part, plotted in yellow. The point where the field returns to zero is named as the remanence magnetisation point. Through applying an opposing field, the curve can continue in the second quadrant, leading to the so-called coercivity field strength H_c . Within this second quadrant, hysteresis curves for permanent magnets are specially shaped as a *knee*, as the progression tends to be very steep from a certain point towards H_c , further mentioned in chapter 2.2.3. If possible, by enlarging the opposing field, the negative saturation magnetisation can be reached. For enlarging the field again, the curve runs towards positive magnetisation again. These steps of a hysteresis is called a maximal gained hysteresis [23].

2.2.2 Ferromagnetism

Materials can be divided into three main groups because of their magnetic behaviour, which include diamagnetism, paramagnetism and ferromagnetism [9]. As this thesis mainly worked with ferromagnetic materials, the focus will be laid on this type.

Compared to the other forms of magnetism, ferromagnetic materials show a high magnetisation after only applying small external H . The effect reflects in the occurring M_s , which is called the *magnetisation saturation*. Figure 2.5 shows this behaviour as well as

the positive value for χ which can take values of 10^5 and a value for μ_r much larger than one.

Ferromagnetic materials own permanent magnetic moments, which orient each other parallel due to strong interactions within the atomic lattice, also named as spontaneous magnetisation. This leads to parallel orientation within certain areas inside the material, called magnetic domains or Weiss domains. To the outside they compensate each other almost completely, although by applying already a small field strength, the material reacts and shows alignment within the domains. Due to already existing orientation of magnetic moments, the material behaviour is not reversible, but can be defined with a hysteresis curve [9], [23].

Compared to the former explained versions, ferromagnetic materials are dependent on temperature change. The magnetisation, as shown in figure 2.5, decreases until the Curie temperature T_C is reached, which signalizes a change in the magnetic behaviour. After reaching this temperature, the material properties change to paramagnetic ones [9]. The name for the temperature comes from the general definition of the *Curie's Law* which implies the inverse temperature dependency $1/T$. The need to modify this law leads to the *Curie-Weiß-Law*, which counts especially for ferroelectric materials, as the magnetic moments show interactions among them [23].

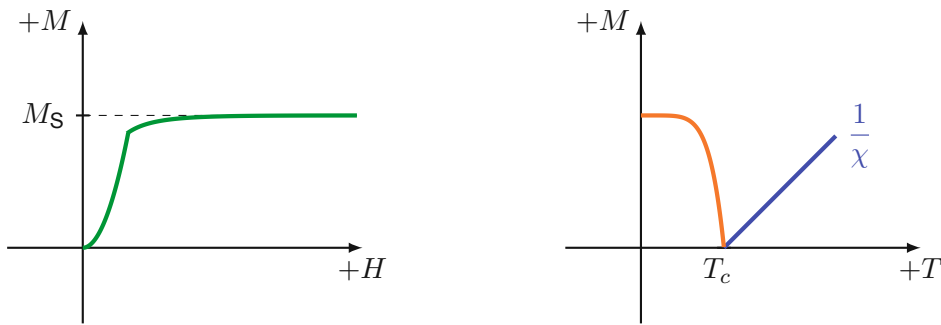


Figure 2.5: Approximated behaviour of ferromagnetic material, figures adapted from [23] and [26]

2.2.3 Permanent Magnets

Permanent magnets can serve magnetic flux density lines without any electric excitation. Especially their shape influence the shape of the occurring field lines [9].

For this type of material, the following equation is used to define their behaviour in the easy axes [24]:

$$B_M = \mu_0 \cdot H_M + B_r \quad (2.29)$$

Permanent magnets, often named as hard magnetic materials, can be split up into three main groups. First group include the AlNiCo magnets, which stands for aluminium, nickel and cobalt. They are identified by their high remanence flux density B_r and relatively low coercivity field strength H_c . The second group covers ferrite like strontium ferrite with a high B_r , compared to AlNiCo magnets, however H_c is lower. The third group contains rare-earth magnets such as NdFeB magnets, consisting of neodymium, iron and boron, which show high values in both B_r and H_c . For the magnetising process a high magnetic field strength is needed, which means at least $2 \cdot H_c$, especially for already high existing H_s of $3 \cdot H_c$ the resulting B_r is $4 \cdot H_c$.

In figure 2.6, a typical hysteresis loop can be seen for permanent magnets, represented by $M(H)$ with M_s , defining the magnetic saturation. H_{CM} stands for if M inside the magnet goes towards zero [27].

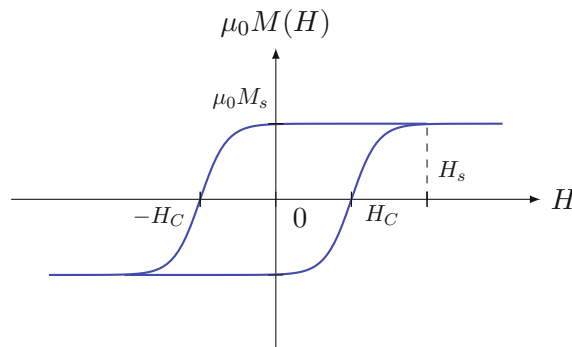


Figure 2.6: Hysteresis curve for rare-earth permanent magnets, adapted from [27].

As equation 2.29 shows, it includes the definition of the working point, which is defined with B_M and H_M . It can be generated out of the above mentioned relation and the air gap function, defined as

$$B_M = -\mu_0 \frac{h_M}{\delta} \cdot H_M \quad (2.30)$$

, including δ for the length of the air gap (in general to define magnetic circuit, but also applicable for synchronous machines between rotor and stator, see chapter 5) and h_M for the height of the magnet [24], [27].

In a simplified assumption of no magnetic leakage flux between the neighbour magnets on a rotor with different magnetic orientation and same air gap and magnet surface, the magnetic flux density is the same for surface mounted magnets as within the air gap. However, as permanent magnet synchronous machines are rotationally symmetric and the surfaces differ between the air gap and the magnet surface, normally B_M is smaller than the remanence flux density B_r , as demagnetization effects occur with an increasing factor of δ/h_M , inversely proportional to the slope of the air gap function [27].

3 Optimization Methods

Taking the example of a loaded beam from [28], in order to find a good balance between the needed amount of material and the needed stiffness, an optimization problem needs to be formulated to generate the optimum out of it. Basically, it can be stated as a minimization problem

$$\min_{\gamma} \Xi(\gamma) \quad (3.1)$$

, using γ here as the variable for a *design vector* which, inserted in the *objective function* $\Xi(\gamma)$, should be minimized. How γ then is chosen defines the type of optimization. If it includes variables that influence the geometry like length or depth, it is called a *parametric optimization*. If γ influences the outside shape of the object, it is called a *shape optimization*. *Topology Optimization* would then be, if γ defines a function that defines each point within the object to be solid or void [28].

Compared to the other two options, Topology Optimization is more flexible as any kind of shape can be approached. Therefore, it is interesting to see how the combination with the Virtual Magnet Method influence the output in a different way rather than using an optimization approach that is already fixed in some restrictions.

3.1 Topology Optimization Method

Topology Optimization Method gives ideas for compositions that would have not been obvious to design [29], [28]. Mentioned in [30], various shapes where optimized for different objectives and resulted in geometries that appear similar to some objects evolved over centuries of years by nature. Examples shown there were a cube optimized that resembled an apple, or leafs and roots structures were generated. As stated in [31], Topology Optimization was mainly used for mechanical optimization problems, but was increasingly enlarged for problems to be solved for permanent magnets. Some common examples of applications for an unusual usage of this method are electrical machines, as there will be a more detailed discussion about a specific type of machine in chapter 5. Another example would be designing magnets for magnetic resonance imaging systems, as well as actuators with cores in c-shape.

In general, the Topology Optimization Method is an iterative problem and can be mathematically expressed as a minimization problem, based on the simplified version in 3.1, as follows [30], [32], [33]:

$$\Xi(\mathbf{u}(\boldsymbol{\rho}), \boldsymbol{\rho}) = \sum_i \int_{\Lambda_i} \xi(\mathbf{u}(\rho_i), \rho_i) dV \quad (3.2a)$$

$$s.t. : G_0(\boldsymbol{\rho}) = \sum_i \nu_i \rho_i - V_0 \leq 0 \quad (3.2b)$$

$$s.t. : G_j(\mathbf{u}(\boldsymbol{\rho}), \boldsymbol{\rho}) \leq 0, \quad j = 1 \dots M \quad (3.2c)$$

$$s.t. : \rho_i = 0 \text{ or } 1, \quad i = 1 \dots N \quad (3.2d)$$

u expresses a state field, satisfying a (non)linear state equation. The objective function is displayed as an integral over a local function $\xi(\mathbf{u}(\rho_i), \rho_i)$. In 3.2, the area Λ is divided

into finite elements and therefore the density distribution correlates to N elements, 3.2d, and then ρ displays the vector of the design variable of dimension N and includes the material distribution. It can either be 0, if within the area of Λ it should be void, or 1, if there should be material. The definition of Ξ describes, like in the beginning of this chapter, the objective function, depending on the constraints coming with $G_0 \leq 0$, defining the volume constraint, and M other possible constraints $G_i \leq 0$. This number of additional constraints is set because for real life applications there are mostly additional constraints to the volume. Even though some problems might not have a volume constraint or have no volume to optimize, it might be a guidance for the main optimization goal to fulfill.

[32].

There are several different variations of Topology Optimization methods, such as phase field, homogeneous or level-set method, ESO (evolutionary structural optimization), GA (genetic algorithm) or PSO (particle swarm optimization). The homogeneous density approach is one of the most used ones and as well used within this thesis. It will be explained in detail in chapter 4 [30].

3.2 Virtual Magnet Method - Continuous approach

The Virtual Magnet Method can be used to optimize permanent magnet assemblies, and is predicated on the reciprocity theorem. This theorem defines two regions, labeled with 1 and 2. Number 1 stands for the system with the "real" magnet, which is to be optimized, number 2 defines the virtual case, as it does not exist physically, only as a mathematical construction. Therefore, the expression in equation 3.3 shows the field distribution in area 1 which maximizes the objective functional $u(x)$. The functional \mathcal{S} behaves linearly with regard to the magnetic field strength H_1 . Here it must be pointed out that the following statements are based on equation 2.28 and their constraints like no free currents within the region [5].

$$\mathcal{S}[H_1] = \int dV H_1(x) \cdot u(x) = \int dV H_1(x) \cdot B_{r2}(x) \quad (3.3)$$

Equation 3.3 includes an expression for an objective representing the desired magnetic vector field, $u(x)$, whereas x denotes any point in this given vector field [5],[8]. In order to create a maximum integral expression in 3.3, for a fixed value of $B_{r1}(x)$, it needs to be aligned with $H_2(x)$ for every x inside the design region. The former is though caused by $B_{r2}(x)$, as can be seen in equation 3.4.

More precisely, the principle of equivalence of magnetic energy can be explained by:

$$\int dV H_2(x) \cdot B_{r1}(x) = \int dV H_1(x) \cdot B_{r2}(x) \quad (3.4)$$

As an illustrative example, a Halbach cylinder like demonstrated in figure 3.1a and 3.1b, is given, to interpret the reciprocity theorem better. The idea for this representative field of an Halbach cylinder was taken from [31].

A Halbach cylinder can be defined, mostly assumed as infinitely long, cylinder with magnetic material surrounding a bore realised as an air gap [34]. Therefore, as shown in figure 3.1a, the vector field u , marked as black arrows, is only defined within the area of Ω , which denotes the inner circle, while outside it is zero, hence minimizes the integration area. Figure 3.1b shows the result of the virtual magnet method for the desired uniform

field in the bore $u(x)$. The resulting magnetic vector field lines are held in green, the red arrows represent the magnetic remanence flux density within the magnet area.

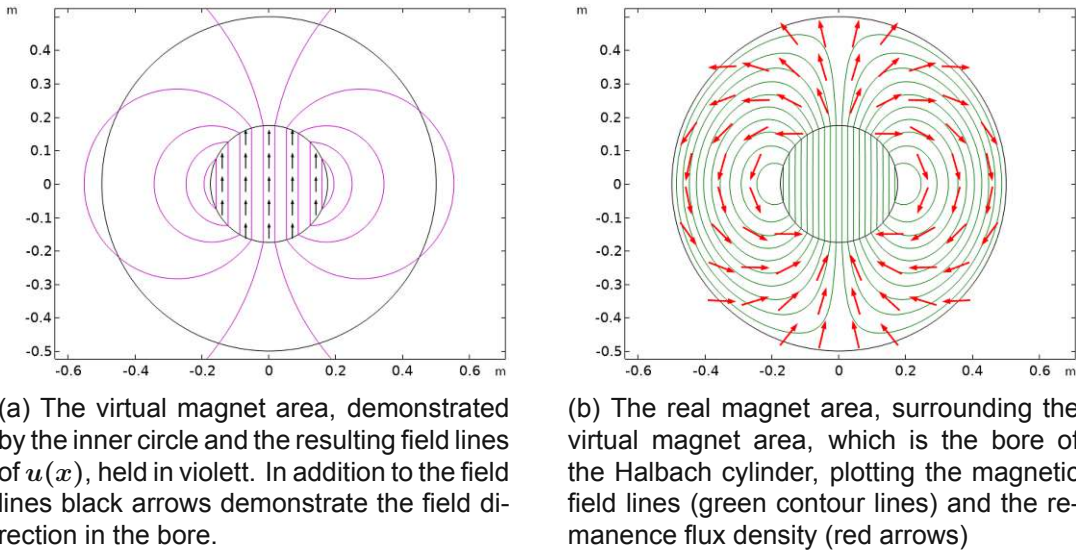


Figure 3.1: Virtual Magnet Method applied on the circular area for an optimized field in the y direction over an averaged field in the inner circle [8]

Equation 3.4 states that the energy owned by magnetic flux sources, represented by B_{r1} , of system 1 when it is located in a field which is generated by the flux sources of system 2, represented by H_2 corresponds exactly with the energy owned by magnetic flux sources, represented by B_{r2} , of system 2 when it is located in a field which is generated by the flux sources of system 1, represented by H_1 [6]. In other words, inside the air gap, a virtual magnet is placed to produce a remanent flux density in the area around, which consists of permanent magnet material.

3.2.1 Border considerations between magnet and other material and optimal energy efficiency

Regarding the left side of equation 3.4, an alignment between the remanence flux density norm and the magnetic field strength results in an expression as the following:

$$\|H_2(x)\| \|B_{r1}(x)\| \geq 0 \quad (3.5)$$

Equation 3.5 includes the origin why a different remanence in the area outside of the magnet area cannot influence the optimal chosen remanence direction for the magnet itself [5]. All the above mentioned effects are a conclusion of given linearity between the physical parameters $B_{r1}(x)$ and $H_1(x)$, and S and $H_1(x)$ respectively. Aside this relation, regarding equation 3.4, it was indirectly assumed that the magnetic susceptibility, the relation between the magnetic field strength and magnetisation, equals in the real and virtual system, which results in a not predictable state of how the material will be distributed ideally. A simplification can be though made if one of the materials consists of air, the other one of permanent magnet material, as then the area with especially rare earth permanent magnets show no susceptibility, therefore in advance, no apportionment of material needs to be done [5].

As mentioned before, $B_{r1}(x)$ and $H_2(x)$ are aligned, and S behaves linear towards $B_{r1}(x)$, hence an ideal distribution of magnet material would be by placing it in regions

with a high value of the normalized virtual magnet field. Resulting out of this fact, the ideal border between air and magnet material can be defined as the equipotential surface of the virtual scalar field $H_2(\mathbf{x})$ [5].

Regarding chapter 5, where the geometrical model consists of permanent magnet material, air and soft magnetic material such as iron, it is important to mention which impact this material has for ideal border conditions. As the remanence in the permanent magnet field area is always directed perpendicular to the region contiguous to it, filled with a high permeable material, e.g. soft iron, the remanence must then be as a consequence directed perpendicular to the border between the two materials. Therefore, it is indirectly clarified which orientation the remanence must have when two regions filled with permanent magnet material and soft iron are adjacent to each other [5].

A main figure of merit for magnet structures and later used for discussing results, is the magnetic efficiency factor [35]:

$$\mathcal{M} = \frac{\int_{\Lambda} dV \|\mathbf{B}_1(\mathbf{x})\|^2}{\int_{\Lambda_m} dV \|\mathbf{B}_{r1}(\mathbf{x})\|^2} \quad (3.6)$$

Equation 3.6 provides an expression for the ratio between the stored energy in the field and the possible maximum energy provided by the magnet material. Its maximum value to be achieved is 0.25 [35], which is explained in more detail in [36].

The integral regions Λ , used for the air gap with μ_0 and Λ_m as the magnet region with a uniform permeability of μ , should not overlap. Combining them although should result in the total observed area, except those parts with a very high permeability. B_{r1} of the real system should be proportional additionally to the fact of being aligned to H_2 .

If all the above mentioned restrictions can be applied, then the magnetic system is energy efficient to its maximum. Fulfilling the fact of the proportionality and the uniformly defined permeability inside the magnet area, it adds up to that B_{r1} is defined as a non-rotational zero-divergence field [5].

Regarding the before remarked optimal border condition, this can be asserted through:

$$\mathbf{H}_2 = -\nabla V_{m2} \quad (3.7)$$

The right-hand side of equation 3.7 defines an equipotential surface of the magnetic scalar potential V_{m2} of the virtual system, as explained in chapter 2.1.1, which creates the magnetic field strength of the virtual system, H_2 [5].

Making use of the idea of the optimal border as defined in equation 3.7 is done for chosen geometries in chapter 4 [8].

3.3 Virtual Magnet Method - Segmented approach

For certain applications, a segmentation of the magnet area into uniformly magnetized blocks is needed. Therefore, this method offers a segmented approach as well, where the ideal remanence of each segment is defined by the field of the virtual magnet, where the average over the volume of the concerning segment is taken, if its border is predefined already. The border definition has to be taken from the optimization process directly only if the segment shapes are not defined in advance [5],[8].

As for simplicity reasons, further investigations here will focus only on the continuous approach of the Virtual Magnet Method. Possible amplifications with a segmented approach and Topology Optimization will be discussed in chapter 6.

3.4 Differences in methods

As there is an increasing need to find an optimized magnetization direction with Topology Optimization, it is interesting to investigate whether it can be combined in some aspects with the Virtual Magnet Method or identify some aspects which can be investigated in future research, as already touched on in chapter 1.

This sub-chapter should give an overview over the main differences and common aspects of both mentioned methods. In [8] the aspect of achieving a global optimum which is of high quality is an aspect which can be ignored for this thesis, as only examples are mentioned here where, if segmentation within Virtual Magnet Method would be applied, the segmentation is that low so that the results show an appropriate value of confidence for a global optimum. Another bullet point in [8] which does not have to be considered here is the dependence of simulation time for three-dimensional problems, as here the focus lies on two-dimensional models only.

Two aspects where both methods agree with each other are those of being able to work with any kind of permanent magnet shape and that there are no geometrical constraints.

The following conditions though disperse between the two methods. The first condition is that the Topology Optimization Method needs shapes that are regularized, whereas the Virtual Magnet Method does not hypothesize it. Furthermore, former delivers an ideal shape of parts consisting of iron, which is not the case when using the Virtual Magnet Method. The last big aspect which differs with the former, is that Topology Optimization can work with objective functionals that are not linear, as well as the constitutive relations do not need to be linear as well.

As clearly highlighted in [8], Virtual Magnet Method offers a more reliable and fast optimization compared to Topology Optimization, however former guarantees more flexibility in many aspects.

In the following two chapters, both methods will be investigated first individually, then a combination will be done for more simple geometries, as it is interesting to see if some of the limits and strengths of each method can be combined in an optimal way [8].

4 Optimization methods applied on simplified geometries

As mentioned in [6], some examples of this paper are used here to show how the Virtual Magnet Method and the Topology Optimization Method is applied. First, it is explained how to implement both methods separately in COMSOL for chosen examples, then the combination of both methods is delineated for two specific examples.

4.1 COMSOL Multiphysics - 2D modelling

To perform both optimization simulations on different geometric objects, the simulation software COMSOL Multiphysics is used. This framework works for finite element approaches as serves as a numerical implementation [35]. As for a first approach of combining the two methods, it was decided, for reasons of faster reproduction and shorter simulation time, to limit to only to 2D models, as also mentioned as a disparity between them [8]. Additionally, like mentioned in [5], models in two dimensions can be assumed if one direction has no specific change in its physical state compared to the other two directions. Therefore, the following models are expected to be infinitely long in one direction.

4.1.1 Realising Virtual Magnet Method in COMSOL Multiphysics

To realise the Virtual Magnet Method, in detail explained in chapter 3, the relevant equations 2.2c, 2.8a and 2.11, explained in chapter 2, are applied to the whole area of the created object. Within the object, two different areas need to be differentiated: one part for the real system, the other one for the virtual system.

For the virtual system, the magnetization is applied to the design area. On the other hand, for the real system, the magnetization is applied to the virtual area, also field area, as the optimization objective depends on the magnetic field over that area.

In the following sub-chapters they will be named as R_m for the real (magnet) system, the virtual (magnet) system will be named as R_g .

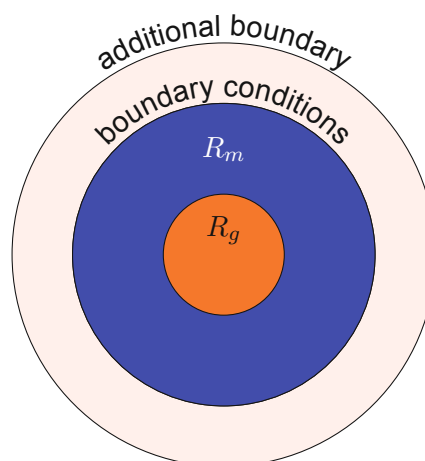


Figure 4.1: Schematic explanation of area correlation for Virtual Magnet Method [5]

Aside of that, setting the right boundary conditions, as mentioned in chapter 2, is important as the electromagnetic laws need to be valid not only within the object, but also on

the edges. Additionally, they serve as boundaries to differentiate the object from its surrounding, mostly air, but also for some simulations inside the object they help to clarify the different physical states of the materials used. Figure 4.1 reveals the correlations.

4.1.2 Realising Topology Optimization Method in COMSOL Multiphysics

To implement Topology Optimization Method for the following examples with permanent magnet material and soft iron, the node "Topology Optimization" is applied on the designed component in COMSOL. The so-called "Density Model" comes along with certain constraints and variables, where it can be defined, how many materials and under which constraints certain materials should be used or not used. Moreover, it can be specified if these constraints are given for every mesh edge point or it can be defined for the complete element of the mesh itself. As stated in [37], the name "density model" explains that a defined interpolation function is used by control parameters in order to define the framework for the desired material specifications.

The Density Model of Topology Optimization makes use of the Helmholtz filter. This type of filter is used in general to even input data in order to use it with lower noise level. It basically solves the partial differential equation as follows [38]:

$$\nabla \cdot (-R^2 \nabla g) + g = D \quad (4.1)$$

Equation 4.1 defines the data input with D , with g the filtered data and R stands for the filter radius, which biases how improved the solution can be and if reduced amount of steps achieve the same result [38].

Therefore, it can be well applied for Topology Optimization, as illustrated in equation 4.2 [37]. The analogon of input data D would be θ_c , which is fed to the differential equation. The output data g is shown as θ_f , the filter radius is similarly named as R_{min} . The indexed expression *min* shows that the radius is often chosen as the edge size of the mesh by default [37].

$$\theta_f = R_{min}^2 \nabla^2 \theta_f(x) + \theta_c \quad (4.2)$$

$$0 \leq \theta_c \leq 1 \quad (4.3)$$

Equation 4.3 shows the span of θ_c . The one-dimensional Heaviside function $\mathcal{H}(x)$, displayed in figure 4.2, should give an idea of how θ_c would act for a one-dimensional problem. The filter aspect can be seen in this figure as the step function is smoothed by the other two exponential expressions held in orange and yellow.

Another relevant parameter for Topology Optimization using the density method is gray-scaling. It can be minimized by *projection*, which is the definition for a smooth step function.

Within figure 4.2, the significance of two parameters that result in figure 4.4 can be explained: β , defines how steep the function in orange and yellow is, so how sharp the difference between the two main values will be, in order to reduce gray-scaling. It is also directly called steepness of the projection. θ_β defines where the projection point is set, which means where the function changes from one value to the other one.

The volume factor θ , as shown in figure 4.4 on the right side, can be expressed as [37]:

$$\theta = \frac{\tanh(\beta(\theta_f - \theta_\beta)) - \tanh(\beta\theta_\beta)}{\tanh(\beta(1 - \theta_\beta)) - \tanh(\beta\theta_\beta)} \quad (4.4)$$

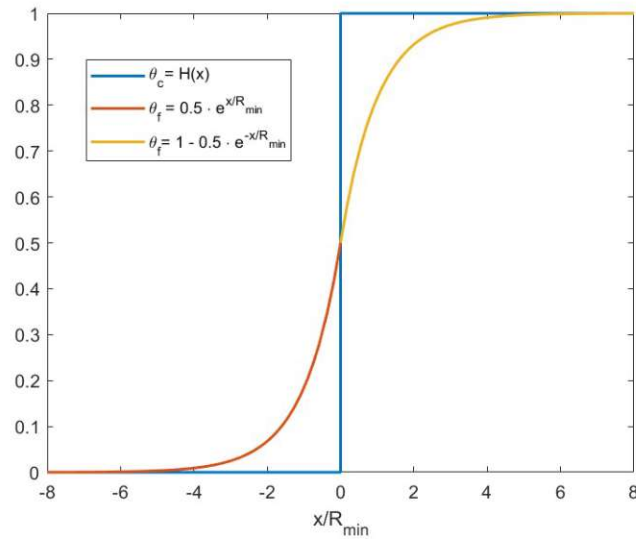


Figure 4.2: Illustration of the analytical solution of the Helmholtz filter equation by a one-dimensional Heaviside function [37]

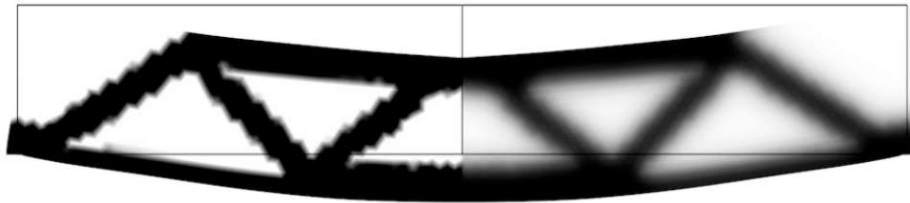


Figure 4.3: This figure represents an MBB (Messerschmitt-Bolkow-Blohm) beam. The left side displays the not-filtered control variable θ_f , the right side shows the filtered θ_f [37], [39]

A third key component when using the density approach is the *interpolation type*. Two main types are used frequently, which are named *SIMP* (*solid isotropic material with penalization*) and *RAMP* (*rational approximation of material properties*). Apart from those two, the *Darcy interpolation* exists, but is used mainly for fluid mechanics [37].

The SIMP interpolation has the ambition to create an interpolation that is continuous and works between void and solid state by using intermediate density values as a penalization function. This is expressed in the following two equations:

$$\theta_p = \theta_{min} + (1 - \theta_{min})\theta^{p_{simp}} \quad (4.5a)$$

$$E_p = \theta_p \cdot E \quad (4.5b)$$

Equations 4.5 represents the relation between the material parameter, expressed as the Young's Modulus E and the density value θ_p that defines the design variable at the same time. p_{simp} as the exponent expresses the penalization parameter. An ideal value for p_{simp} was found out to be 3, as too low or too high values of it would cause either less gray-scaling effects or a too fast convergence towards a local minimum [32], [37]. Mentioned in [32], the value $p_{simp} = 3$ gives additionally the possibility to realize the optimized object

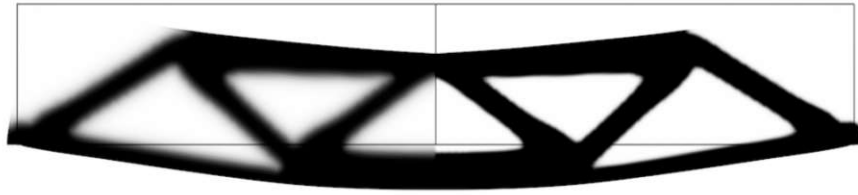


Figure 4.4: This figure represents an MBB (Messerschmitt-Bolkow-Blohm) beam. The left side displays the filtered control variable θ_f , the right side shows θ with reduced gray-scaling [37], [39].

with intermediate densities. Its big advantage is to generate a fast solution over material density, meaning where to have material (solid) or not (void).

In comparison to the SIMP interpolation that specifies on describing the material through its stiffness with an exponential relation 4.5a, the RAMP interpolation influences the material through its elasticity with a rational function. Contrary to the SIMP algorithm, it provides more smooth density distribution in its solution rather than fast definition of certain regions. A mathematical expression for this interpolation type can be given by [33]:

$$\theta_p = \theta_{min} + \frac{\theta \cdot (1 - \theta_{min})}{1 + q(1 - \theta)} \quad (4.6a)$$

$$E_p = \theta_p \cdot E \quad (4.6b)$$

In comparison to SIMP, the used parameter in equation 4.6a which controls if the material distribution will be more smooth or more binary, as figure (1.32) in [33] demonstrates for different values, is the parameter q . When $q = 1$, a interpolation is linear which includes a smooth material distribution. If q increases, the interpolation develops towards a more parabolic behaviour and leads to binary distribution [33].

Completely independent from the interpolation type is the chosen optimization solver, which is, specifically when using SIMP and RAMP algorithms, the *MMA (Method of Moving Asymptotes)*. It works incremental, as in each step the material distribution will be redefined to get an optimum out of it and simultaneously to guarantee structural integrity. MMA is used for optimization problems for large scale [33].

The main advantage of MMA lies in the split-up of the main problem into individual sub-problems that are convex. This includes that the optimization variables from the beginning do not influence the sub-problems that follows the original one. The fact of convex approximations changes the original convex problem into smaller linear problems with several coefficients by creating asymptotes in each iteration step that are adjusted to find the optimal material distribution while maintaining the structural integrity. Therefore, those advantages have a positive effect on the computational time, especially when problems have less constraints [33].

4.1.3 Evaluation and verification of results depending on examples

For all the results given from COMSOL for the following examples, the designed geometry in COMSOL will be always shown, a real life application for the given example to verify its purpose. The main objective is stated in the beginning, as a field plot and with a mathematical expression of the magnetic field. It will be demonstrated how exact this

objective is met by the two applied methods. For this reason, except for chapter 4.2.3, the other results in chapters 4.2.2 and 4.2.1 need to be validated by their components of a multi-pole expansion.

The background to the multipole expansion was given in chapter 2.1.3, where the ideal factors and their origin were demonstrated. As they provide a mathematical explanation for ideal models of multipoles without any disturbance factors, it needs to be included in the following declaration, as trade-offs occur when modelling real life applications, even with simplifications. Therefore, a partition between the desired value of the expansion and a term which includes the residuals was made [6].

As mentioned in [8], the graph in 4.5 should illustrate the analogy between the definitions in Hilbert space and linear algebra, in order to state the facts in a simpler way. The order of magnitude should be disregarded, as it only serves for better illustration.

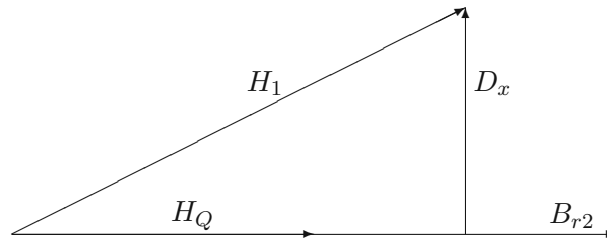


Figure 4.5: Illustration of the analogy to the Hilbert space expressions

H_1 demonstrates the magnetic field strength which represents the distribution of the field in the specific air gap, depending on the observed system later. H_Q is part of the desired vector, Δx , marked as D_x , defines the difference between H_1 and H_Q . B_{r2} , defines the remanence flux density, which is known for the upcoming examples, but not the exact magnitude. To be able to define the relation between H_Q and B_{r2} , it can be said that

$$H_Q \cdot c = \hat{B}r_2 \quad (4.7)$$

$$c = H_Q \cdot \hat{B}r_2. \quad (4.8)$$

Transferring the relation in equation (4.8) into the Hilbert space, as the physical environment here is expressed through vector fields, some expressions used in linear algebra will be transferred into the Hilbert space, were the following elements

$$A \cdot B = \int_{\Lambda} dV A(x) \cdot B(x) \quad (4.9)$$

$$\|B\| = \int_{\Lambda} dV \|B\|^2. \quad (4.10)$$

serve as a basis [8]. Both in equation 4.9, 4.10 and 4.12a - 4.12c, the symbol Λ serves as the air gap area, where the desired field configuration is observed.

As explained in [6] for the example of the analysis of a quadrupole magnet, to consider a suitable figure of merit, the field distribution in the air gap can be considered. Based on the correlation in equation 2.28 in chapter 2.2, the magnetic field strength in the air gap, here defined with the indexed 1, can be expressed as follows

$$\mathbf{H}_1(\mathbf{x}) = \mathbf{H}_Q(\mathbf{x}) + \mathbf{\Delta}(\mathbf{x}) \quad (4.11a)$$

$$\mathbf{H}_1(\mathbf{x}) = \mathbf{u}(\mathbf{x})\alpha[\mathbf{H}_1(\mathbf{x})] + \mathbf{\Delta}(\mathbf{x}) \quad (4.11b)$$

$$\mathbf{H}_1(\mathbf{x}) = \mathbf{u}(\mathbf{x}) \frac{\mathbf{H}_1(\mathbf{x}) \cdot \mathbf{u}(\mathbf{x})}{\|\mathbf{u}(\mathbf{x})\|^2} + \mathbf{\Delta}(\mathbf{x}) \quad (4.11c)$$

Expression $\alpha[\mathbf{H}_1(\mathbf{x})]$ in equation 4.11b stands for a functional of the field $\mathbf{H}_1(\mathbf{x})$ (function of the vector field $\mathbf{H}_1(\mathbf{x})$, [14]), and behaves proportionally to the objective functional \mathcal{S} , which then causes linearity in $\mathbf{H}_1(\mathbf{x})$ [8].

The figure of merit can now be expressed by the two factors, further named with a c , and depending on which part of the multipole expansion is expressed, the subscript symbol will define it. The subscript Q stands for the quality of an ideal field (either quadrupolar or sextupolar, depending on the example later), therefore the second-order or third-order term of the expansion. The subscript Δ summarizes the other residual terms [6],[8].

$$c_Q = \left(\frac{\int_{\Lambda} dS \|\mathbf{H}_Q(\mathbf{x})\|^2}{\int_{\Lambda} dS \|\mathbf{H}_1(\mathbf{x})\|^2} \right)^{1/2} \quad (4.12a)$$

$$\mathbf{H}_Q(\mathbf{x}) = \int_{\Lambda} dS \mathbf{H}_1(\mathbf{x}) \cdot \left(\frac{\mathbf{u}(\mathbf{x})}{\left(\int_{\Lambda} dS \|\mathbf{u}(\mathbf{x})\|^2 \right)^{1/2}} \right) \quad (4.12b)$$

$$c_{\Delta} = \left(\frac{\int_{\Lambda} dS \|\mathbf{\Delta}(\mathbf{x})\|^2}{\int_{\Lambda} dS \|\mathbf{H}_1(\mathbf{x})\|^2} \right)^{1/2} = \left(\frac{\int_{\Lambda} dS \|\mathbf{H}_1(\mathbf{x}) - \mathbf{H}_Q(\mathbf{x})\|^2}{\int_{\Lambda} dS \|\mathbf{H}_1(\mathbf{x})\|^2} \right)^{1/2} \quad (4.12c)$$

For the case of chapter 4.2.4 the above mentioned way of calculating the factors in equation 4.12a - 4.12c can be applied similarly.

4.2 Models of simplified geometries

The following sub-chapters include a general description of the geometric object, then an analysis with the Virtual Magnet Method and the Topology Optimization Method. Eventually, the results will be compared. For the two examples, a combined approach of both methods will be shown.

4.2.1 Sextupole Magnet

The first model used to demonstrate both methods is a sextupole magnet. It is assumed to have similar field properties and an objective function which can be expressed and obtained in a way that the geometry shows directly the effect of the methods and at the same time knowing the desired field lines in advance helps to verify the output of both methods more facile.

The desired field is emerged from the application. When a beam experiences a spread of its momentum, it causes a certain dispersion when passing a dipole. The role of a sextupole magnet is to regulate the chromatic aberration [43].

As shown in figure 4.7, the desired field lines plotted with COMSOL can be seen and is expected as the main objective regardless of the applied optimization method. It clearly shows the dependence of the field lines are weakened quadratic, compared to the field of the quadrupole magnet of the chapter before.

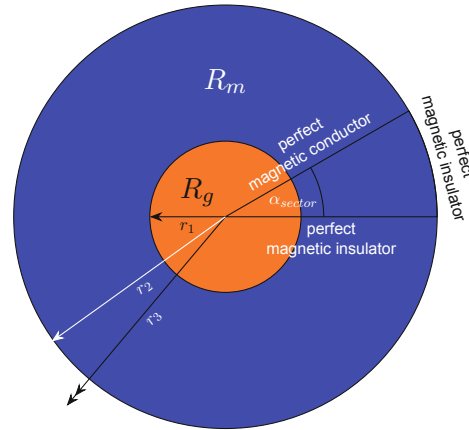


Figure 4.6: This schematic figure serves as a model for the sextupole magnet [6]. The orange area in the middle defines the virtual magnet, the blue circle around represents the design area, in this case the real permanent magnet. The circle segment should demonstrate the sector that is used for applying Topology Optimization Method for the two models, as a symmetric object is observed. The proper boundary conditions are mentioned for the sector sides.

Sextupole - Geometry Configuration	value	unit
r_1	0.175	m
r_2	0.5	m
r_3	2.5	m
α_{sector}	30	°

Table 4.1: Chosen measurements for geometry of sextupole magnet in COMSOL. The idea of taking one sector for Topology Optimization approach was given by [40], the sizes were inspired by [41], the general geometrical shape by [42].

A mathematical expression for the skewed (4.13a) and non-skewed (4.13b) magnetic field density inside the air gap can be given, as resulted from [44] and more detailed explained in chapter 2.1.3, by

$$\mathbf{B}_{g_s} = -0.5 \cdot (x^2 - y^2) \cdot \hat{e}_x + xy \cdot \hat{e}_y \quad (4.13a)$$

$$\mathbf{B}_g = xy \cdot \hat{e}_x + 0.5 \cdot (x^2 - y^2) \cdot \hat{e}_y \quad (4.13b)$$

To achieve this given magnetic field distribution, first the Virtual Magnet Method and then Topology Optimization Method will be applied on the geometry.

Sextupole Magnet analysed with Virtual Magnet Method

The results in 4.9 show clearly the desired field configuration plotted in 4.7 and verify, aside of the results calculated in table 4.2, that it can be used to identify regions to be filled with magnet material. Figure 4.11a then again emphasizes the exact calculation of the resulting field, which is demonstrated through the blue arrow plot, showing the magnetic field strength \mathbf{H} . Demonstrated with red arrows is the difference between the results and the green arrow plot, therefore the "error" that occurs. The green arrows show the best possible approximation of the desired field that can be obtained. It is to be mentioned here that for all three arrow plots a normalization of units was performed, hence they can

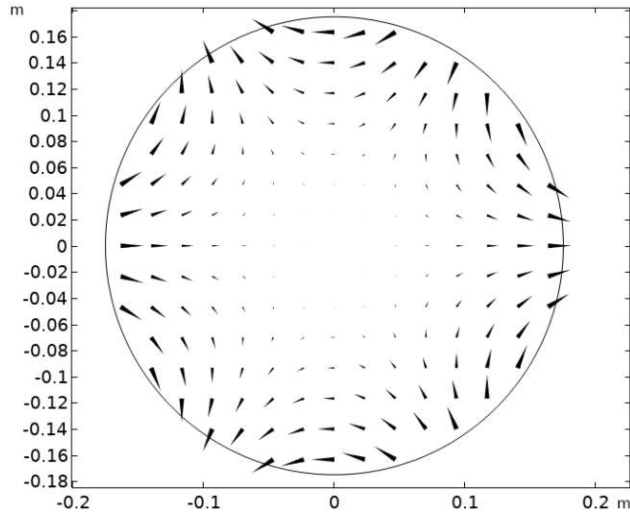


Figure 4.7: Ideal field distribution for the skewed field in the region R_g of a sextupole magnet with switched signs for x and y component to adjust the plots between topology optimization and virtual magnet method results.

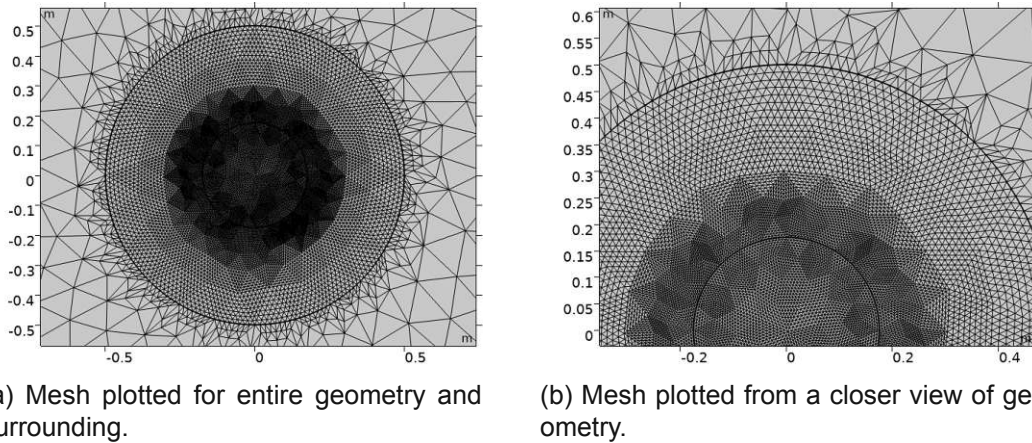


Figure 4.8: Mesh setup for applying Virtual Magnet Method. A refinement number of 3 was applied to the areas that are analysed.

be represented within the same plot and a comparison is valid. This procedure counts for all the following examples in this chapter.

As in figure 4.11a the geometrical shape of the virtual magnet part is ideally circular, it is obvious to obtain the desired field exactly as an output, according to [45]. Therefore, the error plot is not visible with the same factorisation of the other two plots. Comparing the results of the circular inner shape in 4.11a and the hexagonal shape in 4.11b, in the latter there is a slight difference in the edge of the inner field between the green and blue arrows.

Sextupole Magnet analysed with Topology Optimization Method

In this chapter the sextupole magnet is only analysed for the circle segment shown in figure 4.6 where the optimization was applied, taking advantage of symmetry. As for this method a description of the remanence flux density for the design area in order to define magnetic properties is needed, for a sextupole magnet it can be explained based on the general expression for Halbach cylinders as follows [35]

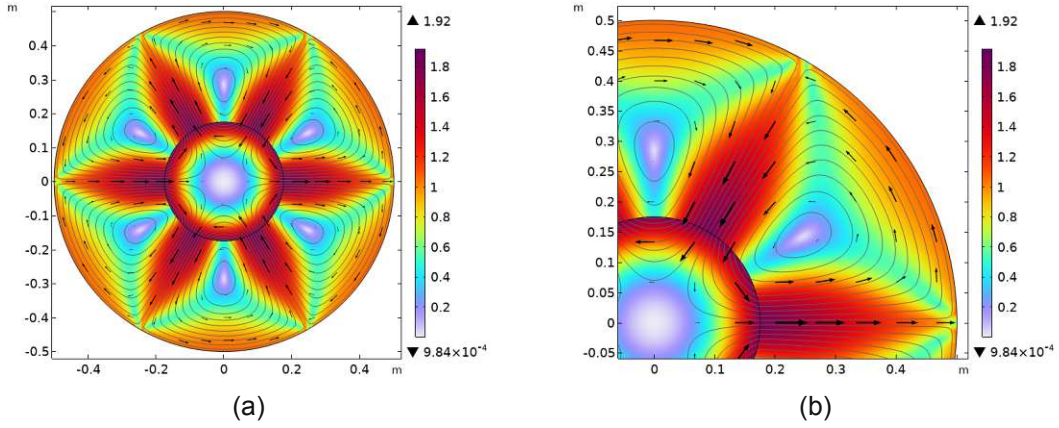


Figure 4.9: Sextupole Magnet optimized in permanent magnet material usage with the Virtual Magnet Method for a skewed field. The contour plot, here demonstrated with grey-colored lines, represent the z-component of the magnetic vector potential A_z . The black arrows demonstrate the magnetic flux density within the design area in its x and y direction. The colour bar serves as a demonstration of the norm of the magnetic flux density, given in Tesla.

$$\mathbf{B}_r = B_{rem} \cdot [\cos(p \cdot \varphi) \cdot \hat{\mathbf{e}}_r + \sin(p \cdot \varphi) \cdot \hat{\mathbf{e}}_\varphi] \quad (4.14)$$

Equation 4.14 states an expression for a homogeneous field with $p = 1$ using the cylindrical coordinate system. The factor p in the argument here serves only as a way to express different field configurations. B_{rem} refers to the maximum value of B_r . By setting $p = 2$ for Cartesian coordinates and using the density optimization variable θ_p to vary in material, it can be adapted to an expression specifically for sextupole magnets [35]:

$$\mathbf{B}_r = \theta_p \cdot B_{rem} \cdot [\cos(4 \cdot \varphi) \cdot \hat{\mathbf{e}}_x + \sin(4 \cdot \varphi) \cdot \hat{\mathbf{e}}_y] \quad (4.15)$$

Equation 4.15 includes the design variable θ_p which varies between zero and one (explained in chapter 4.1.2). B_{rem} is set to 1.4 T which corresponds to comparable values in [6]. φ defines the angle spanned between the x and y component within the air gap area, expressed through the function $\text{atan2}(y, x)$ as it depends on both components. Aside of equation 4.15, a definition for the recoil permeability μ_{rec} was set using θ_p to differentiate between the two desired materials. For $\theta_p = 0$, the permeability value equals the one from iron, if $\theta_p = 1$, then the value changes to the one from rare earth permanent magnets, which can be often approximated to 1. The value 4000 is needed to express the permeability of iron in that equation. As a reference for it it was taken from the COMSOL material library.

$$\mu_r = 4000 \cdot (1 - \theta_p) + \theta_p \quad (4.16)$$

Both equations 4.15 and 4.16 provide enough information about the desired field distribution and the materials that are used. For applying the density method an objective function Ξ needs to be set. For the observed cases here, Ξ will be maximized and is given by:

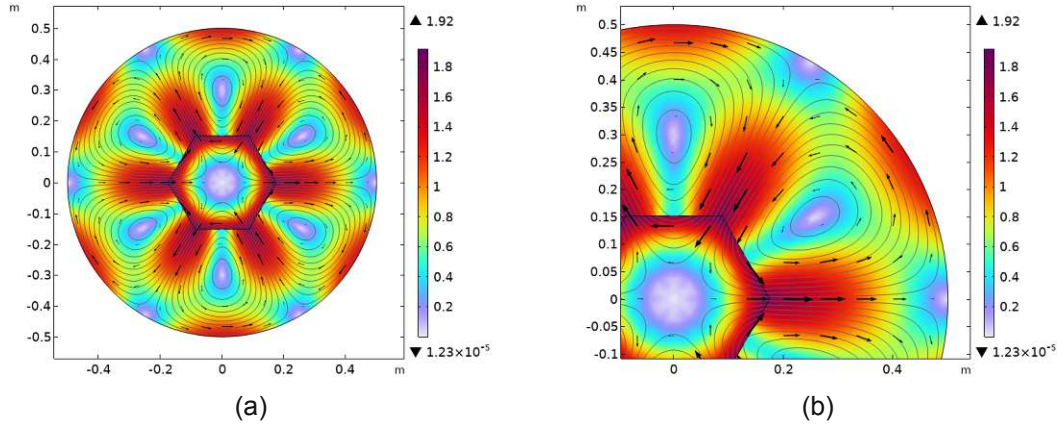


Figure 4.10: Sextupole Magnet optimized in permanent magnet material usage with the Virtual Magnet Method for a skewed field, however with a hexagonal shape inside for the virtual magnet area R_g . The contour plot, here demonstrated with grey-colored lines, represent the z-component of the magnetic vector potential A_z . The black arrows demonstrate the magnetic flux density within the design area in its x and y direction. The colour bar serves as a demonstration of the norm of the magnetic flux density, given in Tesla.

$$\Xi_{1,2,3,4} = \frac{\langle \mathbf{B}_{airgap} \rangle \cdot \mathbf{u}(x)}{d + A_{mag}}, \quad d = 0.2, 0.5, 1, 1.5 \quad (4.17)$$

Maximization of equation 4.17 is chosen as the numerator includes the average of the magnetic air gap field density, $\langle \mathbf{B}_{airgap} \rangle$, which is expressed as an inner product with the ideal definition of a skewed sextupole field in equation 4.13a, $\mathbf{u}(x) = \mathbf{B}_{g_s}$. The denominator A_{mag} includes the expression of the permanent magnet area. In order to vary the emphasis of the magnet amount, a factor d is changed in order to compare four different objective functions and their output.

It is desired to be as small as possible as of cost factors, but still large enough to guarantee a strong field in the air gap, given by the numerator. The 1 added to the area is given only for reasons of more smooth approach of the objective itself [35].

Sextupole Magnet	c_Q	c_Δ	$c_Q^2 + c_\Delta^2$	\mathcal{M}
VMM (circular R_g)	1.0000	0.0015854	1.0000	0.077856
VMM (hexagonal R_g)	0.99867	0.051559	1.0000	0.063621
TOM (Ξ_1 , $\beta = 8$, $p_{SIMP} = \text{set}$)	0.99997	0.0075503	1.0000	$8.2222 \cdot 10^{-8}$
TOM (Ξ_2 , $\beta = 8$, $p_{SIMP} = \text{set}$)	0.99999	0.0043405	1.00000	$5.0264 \cdot 10^{-8}$
TOM (Ξ_3 , $\beta = 8$, $p_{SIMP} = \text{set}$)	1.0000	0.0026474	1.0000	$3.8342 \cdot 10^{-8}$
TOM (Ξ_4 , $\beta = 8$, $p_{SIMP} = \text{set}$)	1.00000	0.0019929	1.00000	$3.4346 \cdot 10^{-8}$
TOM (Ξ_2 , $\beta = 13$, $p_{SIMP} = \text{set}$)	0.99997	0.0075503	1.00000	$8.2222 \cdot 10^{-8}$
TOM (Ξ_2 , $\beta = 20$, $p_{SIMP} = \text{set}$)	0.99972	0.023459	1.00000	$5.9323 \cdot 10^{-7}$

Table 4.2: Representation of the calculated values of the multipole expansion 4.12a, 4.12c and the magnetic efficiency factor 3.6. For the analysis of TOM, the SIMP algorithm was used and changes of β and p_{SIMP} were made, the initial value $\theta_0 = 0.5$ and the projection point $\theta_\beta = 0.5$ was set by default and not changed in this case. The used optimality tolerance for TOM was 0.1, and a maximum of 100 iterations was set as a restriction.

As argued in [6], the factors in table 4.2 are normalized, therefore the expression in

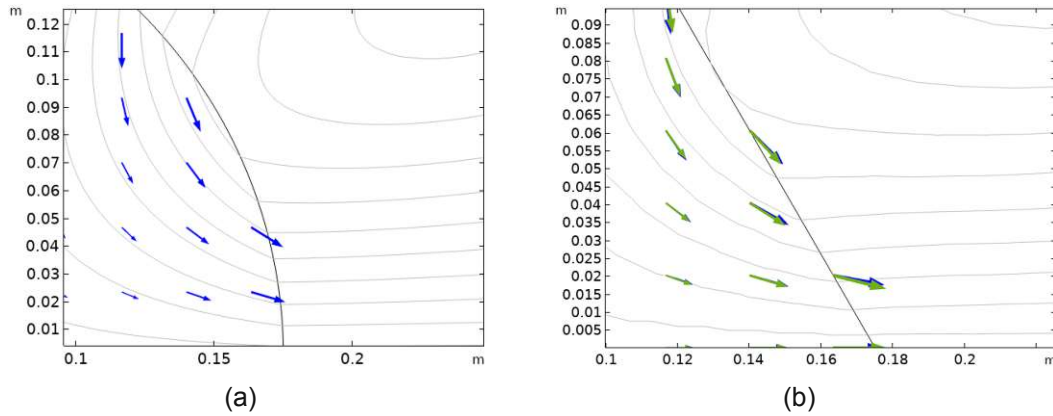


Figure 4.11: A cutout of the skewed field is shown here. The contour plot, here demonstrated with grey-colored lines, represent the z-component of the magnetic vector potential A_z . The green arrows are covered by the blue arrows, the red arrows are too small to be shown within the same scaling.

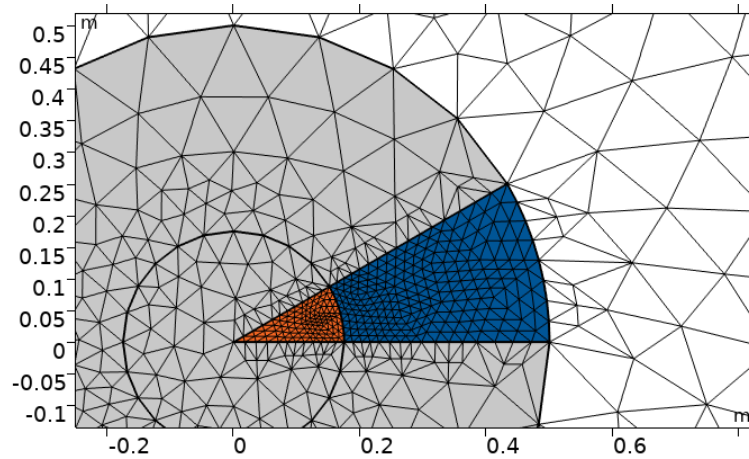


Figure 4.12: Mesh setup for applying Topology Optimization Method for the 30° sector for Sextupole design. A refinement number of 2 was applied to the areas that are analysed, the iron core around the design area was not taken into account.

the third column can be done. When comparing the results from Topology Optimization Method with different values of β , it can be seen that a more significant impact on the results is created by the change of p_{SIMP} , which is automatically set by COMSOL to 3 if not manually changed. By adapting it to higher values above 5, as mentioned in chapter 3, the solution converges very fast and stops after one iteration with no reasonable output. On the other hand, setting the value p_{SIMP} towards lower values than 3, the dependency on the slope factor β gets higher, as can be seen for c_Δ . This value increases by an increasing value of β , which means that the residual terms that should be minimal increase. At the same time, \mathcal{M} increases as well. The magnetic efficiency factor \mathcal{M} in the fourth column, explained in chapter 3.2, gives a significant higher value for objects where the field strength is more important than in these examples. However, for reasons of comparison it is included in every example in this chapter.

Another aspect to consider is shown in figure 4.14a - 4.14d, that specifically for case 4.14c the least amount of magnet material would be used and the objective plot in blue in 4.15 also clearly achieves the highest value among the investigated cases. Although, as men-

tioned through other aspects before, the main focus to achieve beam focusing with the geometry of the field within the bore, needs to be the main objective which is less accurate in this case. In this specific case, a possible approach would be to consider both results from the Virtual Magnet Method and those from Topology Optimization where results of the cases showed in figure 4.13a - 4.13d correspond the most with results given through figure 4.9 and those from table 4.2.

Overall comparing the results of the density method in table 4.2 to the results of the Virtual Magnet Method, it is apparent that this method here achieved better results with a lower value of c_{Δ} .

4.2.2 Quadrupole Magnet

Quadrupole Magnets are used to focus beams of particles which are charged, which mainly appears in the field of particle acceleration [6]. The desired field configuration is to have magnetic field of zero in the center of the air gap, therefore achieving a focusing effect. A slightly different figure is used for the quadrupole compared to the sextupole magnet, as shown in figure 4.16 and table 4.3. The iron yoke was used here only as a schematic representation for a stabilizer that is sometimes used in real life applications, so the idea was inspired by [41]. Although it needs to be mentioned that because of the iron yoke the field lines from the region R_m are forced to be perpendicular to it, so it will affect the output, as results will show. Therefore, this experiment of including the iron yoke was only made for this example and left out for the sextupole magnet, as the results were too strongly influenced by it.

For this example a sector with 45° was chosen which can represent the field properly.

Quadrupole - Geometry Configuration	value	unit
r_1	0.175	m
r_2	0.5	m
r_{sector}	0.75	m
b	1.25	m
chamfer(distance from vertex)	0.3	m
α_{sector}	45	°

Table 4.3: Chosen measurements for geometry of quadrupole magnet in COMSOL. The idea of taking one sector for Topology Optimization approach was given by [40], the sizes were inspired by [41].

Demonstrated in figure 4.17, the skewed version of the quadrupole field was chosen to analyse and taken as an objective. The skewed (4.18a) and non-skewed (4.18b) version can be mathematically expressed by

$$B_{g_s} = y \cdot \hat{e}_x + x \cdot \hat{e}_y \quad (4.18a)$$

$$B_g = x \cdot \hat{e}_x + y \cdot \hat{e}_y \quad (4.18b)$$

Quadrupole Magnet analysed with Virtual Magnet Method

After generating the mesh for the Virtual Magnet Method for the whole geometry, results in figure 4.19 indicate the achieved ideal not-skewed field from figure 4.17. Demonstrated with the magnetic vector potential A_z , the desired field with red arrows is plotted in a cutout of the geometry to show the strong correlation to the resulted arrow plot of c_Q . Especially the plot 4.19a let assume to fill certain areas with permanent magnet material.

Quadrupole Magnet analysed with Topology Optimization Method

Starting from equation 4.14, this one can be adapted in this case to an expression for a quadrupole magnet:

$$\mathbf{B}_r = \theta_p \cdot B_{rem} \cdot [\cos(3 \cdot \varphi) \cdot \hat{e}_x + \sin(3 \cdot \varphi) \cdot \hat{e}_y] \quad (4.19)$$

$$\Xi = \frac{\langle \mathbf{B}_{airgap} \rangle \cdot \mathbf{u}(\mathbf{x})}{1 + \langle \theta_p \rangle} \quad (4.20)$$

Maximization of equation 4.20 is chosen in the same way as for the Sextupole geometry with a similar approach, although the expression of the ideal definition of the non-skewed quadrupole field in equation 4.18b, $\mathbf{u}(\mathbf{x}) = \mathbf{B}_g$, is different. The same equation was taken for defining the two different materials, defined in 4.16.

Figure 4.24 gives a good overview over the different cases applied on the geometry with the SIMP algorithm. Attention needs to be paid for a larger scale for figure 4.24b and 4.24e as for those cases only small regions showed values around 2.5 – 3.5 T. At the same time, the results for defining the magnet-iron border show for those two cases a slightly different result, 4.25b and 4.25e. Although as mentioned in the previous example, the results in table 4.4 needs to be taken into account as well. Therefore, results have shown again for cases with rising value for β had an increasing value of c_Δ and simultaneously for \mathcal{M} . Values for c_Q stayed stable for all cases.

Comparing the objective plots for each case demonstrated in figure 4.26 that with higher values for β the convergence went faster within the first 10 iterations to its optimized end value at the last iteration. Two of the cases with lower β values and especially with the lower value for p_{SIMP} , drawn with the red line, and the predefined case with the automatically set value leads to a lower end objective after 100 iterations than other observed cases.

Quadrupole Magnet	c_Q	c_Δ	$c_Q^2 + c_\Delta^2$	\mathcal{M}
VMM (circular R_g)	0.99992	0.012458	1.0000	0.11672
VMM (pentagonal R_g)	0.99825	0.059071	1.0000	0.094805
TOM ($\beta = 8$, p_{SIMP} set)	0.99974	0.022795	1.0000	0.12983
TOM ($\beta = 14$, $p_{SIMP} = 2$)	0.99997	0.0078568	1.0000	0.16735
TOM ($\beta = 14$, $p_{SIMP} = 2.5$)	0.99997	0.0075649	1.0000	0.16725
TOM ($\beta = 20$, $p_{SIMP} = 2$)	0.99997	0.0075293	1.0000	0.17311
TOM ($\beta = 25$, $p_{SIMP} = 2$)	0.99997	0.0075740	1.0000	0.17316
TOM ($\beta = 9$, $p_{SIMP} = 1.5$)	0.99993	0.0011921	1.0000	0.15003

Table 4.4: Representation of the calculated values of the multipole expansion 4.12a ,4.12c and the magnetic efficiency factor 3.6. For the analysis of TOM, the SIMP algorithm was used and changes of β and p_{SIMP} were made, the initial value $\theta_0 = 0.5$ and the projection point $\theta_\beta = 0.5$ was set by default and not changed in this case. The used optimality tolerance for TOM was 0.001, and a maximum of 100 iterations was set as a restriction.

4.2.3 Magnetic Refrigeration

Another interesting object to investigate, inspired from examples of [6], is a magnetic refrigeration.

As explained in [40], magnetic refrigeration uses the produced magnetic field through permanent magnets to generate a temperature change, whereby a system can be cooled.

Magnetic Refrigeration - Geometry Configuration	value	unit
r_1	0.4	m
r_2	0.45	m
r_3	1	m
r_4	5	m
α_{sector}	90	°

Table 4.5: Chosen measurements for geometry of magnetic refrigeration in COMSOL. The measurements were chosen according to [40]. The idea of taking one sector for Topology Optimization approach was given by [46].

The square in figure 4.27 should demonstrate the sector that is used for applying Topology Optimization Method. As it is a symmetric object, for reasons of simplicity only one quarter is analysed, as the output field distribution can easily be mirrored to the other sectors. As for boundary conditions, the inner two sides of the square are used, for the outside, the sector of the blue circle is used.

The radius r_4 in table 4.5 and outlined in figure 4.27 serves as a wide region where the main geometrical object can be investigated and proper boundary conditions are guaranteed. Therefore it was chosen to be five times the outer radius of the observed geometry.

Magnetic Refrigeration analysed with Virtual Magnet Method

The desired B_g field within the area R_g has the following shape:

$$B_g = \text{sign}(x) \cdot \frac{x}{\sqrt{x^2 + y^2}} \hat{e}_x + \text{sign}(y) \cdot \frac{y}{\sqrt{x^2 + y^2}} \cdot \hat{e}_y \quad (4.21)$$

The denominators represent the normalization of each component, $\text{sign}(x)$ stands for the signum function and serves to express the field direction properly.

For reasons of simplicity, similar in [40], the inner part of the geometry will be already determined to soft iron with a relative permeability of $\mu_r = 1000$ and other parameters set by the material library of COMSOL Multiphysics. Hence only the ring outside, named as R_g in figure 4.27, serves as design area. Additionally, it should be noted that the extra circle in the air gap ring between the inner iron circle and the outer design area in figure 4.28c or e.g. in figure 4.29b only serves for calculating the magnetic flux density along this curve.

The results produced in figure 4.29 are similar to the results presented for magnetic refrigeration in [6]. The regions that are aimed to be strong field regions appear as "kidney-shaped" in figure 4.29a, held in red on the left and right side of the inner circle, which resembles the results in figure 4 in [6].

Magnetic Refrigeration analysed with Topology Optimization Method and combined approach

Additionally mentioned, the investigation for all of topology optimization variations for this example have been made by using one quarter of the geometry and setting the proper boundary conditions on the borders, based on the approach of [40]. This is shown for the mesh in figure 4.30.

As already mentioned in the previous examples, an expression needs to be found for the remanence flux density within the design region. It can be explained based on the

general expression for Halbach cylinders, inspired from [35], and adapting it with $p = 1$ for the Cartesian Coordinate system to

$$\mathbf{B}_r = \theta_p \cdot B_{rem} \cdot [\cos(2 \cdot \varphi) \cdot \hat{\mathbf{e}}_x + \sin(2 \cdot \varphi) \cdot \hat{\mathbf{e}}_y] \quad (4.22)$$

$$\mu_{rec} = (1000 - \theta_p \cdot 2000) \cdot (\theta_p < 0.5) + 1 \quad (4.23)$$

This time, a different formulation is given for the recoil permeability, which includes an expression that works as a differentiation between the case of having $\theta_p < 0$ and $\theta_p \geq 0$. The former result in an expression for μ_{rec} as only including the first part of the equation which ends up as $\mu_{rec} = 1000 - \theta_p \cdot 2000$, which stands for an iron-based material. Latter includes the opposite, so only the second term of the equation counts and results in $\mu_{rec} = 1$, which represents permanent magnet.

$$\Xi_1 = \frac{\langle \mathbf{B}_{slot} \rangle}{1 + \langle \theta_p \rangle} \quad (4.24a)$$

$$\Xi_2 = \frac{\langle \mathbf{B}_{slot} \rangle}{0.5 + \langle \theta_p \rangle} \quad (4.24b)$$

For this example, two objective functions were investigated. The difference between them lays in the modeling of the denominator to create a more smooth transition. The main objective although remains as the difference between the high field regions R_g (held in orange in figure 4.27) and low field regions (the rest of the white ring in figure 4.27) needs to be maximized by simultaneously using least amount of magnet material, defined in the denominator. This idea was inspired by [35] and [40].

In both definitions of the objective functions 4.24a and 4.24b, $\langle \mathbf{B}_{slot} \rangle$ stands specifically for the norm of the magnetic flux density in that part of the air gap where the field needs to be strong.

To have a larger variety of results, a comparison between the virtual magnet method was made with two separate approaches of algorithms for Topology Optimization: SIMP and RAMP. For each, the combined approach with the Virtual Magnet Method was made. The focus on investigated parameters laid on the magnetic efficiency \mathcal{M} like in the previous examples and the maximum value of the norm of the magnetic flux density in the area air gap area R_g , summarized in the following tables 4.6 and 4.7.

The combined approach was made by using the topology optimized outputs and adapting it to the virtual magnet method, so that in the end both methods are applied. More precisely, instead of having the physical laws for the regions within the geometry only defined by the material design variable θ_p , the design area is additionally defined through the virtual magnet method, but using the expression of equation 4.23 for the material definition. Aside of the magnitude of the remanent flux density within the design area, defined with θ_p as usual for the density method, now for the direction of it the reference to the virtual magnet area R_g is used instead, which includes the definition of \mathbf{B}_g in 4.21. Separately it needs to be mentioned that the expression of μ_{rec} needs to be mentioned within the definition of the virtual system this time.

Figure 4.31 reproduces the kidney-shaped result of VMM in all cases, except in the combined approaches in 4.31e and 4.31f. The latter shows more influence from the virtual

Magnetic refrigeration	\mathcal{M}	$\langle B_{airgap_{max}} \rangle [T]$
VMM	0.059253	2.2528
TOM ($\beta = 8, p_{SIMP}$ set, Ξ_1)	0.13094	2.0020
TOM ($\beta = 8, p_{SIMP}$ set, Ξ_2)	0.17202	1.7193
TOM ($\beta = 14, p_{SIMP}$ set, Ξ_1)	0.12736	1.9209
TOM ($\beta = 14, p_{SIMP}$ set, Ξ_2)	0.17159	1.7330
TOM ($\beta = 8, p_{SIMP}$ set, Ξ_1) & VMM	0.15828	2.1853
TOM ($\beta = 8, p_{SIMP}$ set, Ξ_2) & VMM	0.16358	1.9493

Table 4.6: Results of VMM and TOM with SIMP algorithm and combined approach. The best result regarding the tradeoff between both calculations was highlighted in yellow.

magnet method. The partly occurring white areas in the field plot signifies that those regions are out of the common set range, which was chosen for better comparability.

The table in 4.6 provides information about the calculated figure of merit \mathcal{M} and the maximum value of the magnetic flux density in the air gap at the angle 0. Highest values could be achieved through Ξ_2 despite the changing β values. Similar values were achieved through the combined approaches. Comparing these results with the second column in table 4.6, a slight correspondence can be seen between raising values of the maximum air gap flux density and falling values of \mathcal{M} .

The maximum value of the air gap flux density in table 4.6 was taken from the plot in figure 4.32 at 0° . Especially in this plot compared to the result for *VMM* solution in [6], only a sector of $0^\circ - 90^\circ$ was plotted as of symmetry reasons and better visibility. The combined approaches occur with similar results. They clearly show the influence of the local maximum at 75° of the *VMM* result, however shifted to the angle close to 60° . The red line of Ξ_1 with $\beta = 8$ has a longer lasting plateau compared to the rest, starting already from 55° . The course of the non-combined approach lines do not have any effect on the combined approaches, only for the dark blue line with Ξ_2 and *VMM*, a short plateau is recognizable.

Regarding the objective plots in figure 4.33, Ξ_2 achieves one of the highest objectives, which corresponds with the results of \mathcal{M} . This perhaps influenced as well the result of the combination with Ξ_2 , even though the plot stopped before iteration 20. The combined approach with Ξ_1 had the most iterations and a continuous raise in the plateau.

Comparing the results of the combined approaches in figure 4.34 with the rest (4.34a-4.34d), there is no significant kidney-shaped magnet result. Even the topology optimized versions have, additional to the kidney shaped part an extra magnet area, except for 4.34d. The kidney areas close to the 0° area explains the high magnitude of the radial component of the magnetic flux density and the high achievements of the objective. Surprisingly the result in 4.34d has no second magnet part and the kidney magnet area is smaller than the rest of the results in 4.34a-4.34c.

For the RAMP investigation, the same set-up in terms of objective functions Ξ and changed values for β were used, to make it better comparable.

The magnetic field norm plot in figure 4.35 is, regarding the resulted shapes of the arrow plot and the field lines of the z-component of the magnetic vector potential, comparable in strength and size to the results achieved by using SIMP algorithm in 4.31.

For this particular case when using RAMP algorithm, in table 4.7, the dependency on the

Magnetic refrigeration	\mathcal{M}	$\langle B_{airgap_{max}} \rangle [T]$
VMM	0.059253	2.2528
TOM ($\beta = 8, q_{RAMP} = 3, \Xi_1$)	0.12998	1.9860
TOM ($\beta = 8, q_{RAMP} = 3, \Xi_2$)	0.15642	1.7118
TOM ($\beta = 14, q_{RAMP} = 1.5, \Xi_1$)	0.13237	1.9421
TOM ($\beta = 14, q_{RAMP} = 1.5, \Xi_2$)	0.16715	1.7970
TOM ($\beta = 14, q_{RAMP} = 3, \Xi_1$) & VMM	0.15655	2.0915
TOM ($\beta = 14, q_{RAMP} = 1.5, \Xi_1$) & VMM	0.13184	2.2308

Table 4.7: Results of VMM and TOM with RAMP algorithm and combined approach. The best result regarding the trade-off between both calculations was highlighted in yellow.

variable q_{RAMP} was tried to investigate, aside of changing Ξ and β .

This table gives partly the explanation of why for the combined approach only Ξ_1 and $\beta = 14$ were chosen, as with them higher results in \mathcal{M} and especially $\langle B_{airgap_{max}} \rangle$ were reached. The general correspondence of higher values in \mathcal{M} resulting in lower values in $\langle B_{airgap_{max}} \rangle$ suit for the RAMP investigation here as well.

Overall shows the table 4.7 a similar result range than 4.6, however the values for the figure of merit \mathcal{M} are a little lower. With the combined approaches higher values for $\langle B_{airgap_{max}} \rangle$ could be obtained.

Including the plots of the radial component of the flux density here as well, compared to the results with SIMP algorithm, the curves are more spread between the same objectives. The combined approaches were influenced by the local maximum of Ξ_1 at 70° , although theirs occurred at 60° . The course of the combined approach plots were congruent. They also show a different behaviour with $q_{RAMP} = 1.5$, as they reach a global maximum at 30° , compared to the version with $q_{RAMP} = 3$, where the plateau correlates to the solution of the one where SIMP was used.

The local maximum at 30° might be explained by the small extra magnet area as a result in 4.36f, compared to 4.36e. Generally, the magnet areas are similar to the results of SIMP, although the areas of the solution in 4.36b and 4.36c are smaller than in the SIMP result.

The objective of Ξ_2 appears again in figure 4.38 as the highest, compared to the rest. The combined approaches could reduce their plateaus, whereas for the TOM approaches only the plateaus started at iteration 20 with almost no change afterwards.

Differences in some results compared to e.g. [35] can be attributed to different size of the simulated geometry, as for smaller size the differences in the magnetic flux density between different optimization results may vary less, according to [35].

As well it changes the output when the "optimality tolerance" in COMSOL is changed, which results in less executed iterations and therefore less iterations that might lead to another, more optimized result. For all the given examples here an optimality tolerance, as already stated before, of 0.001 was used in the simulation environment.

4.2.4 Simplified Model for electric motor

This model was as well inspired by the investigation of the simplified electric motor model of [6], however adapted to a switch between rotor and stator, so that in this model, the stator is the outside ring, whereas the inside area, the design area, represents the rotor that is optimized.

Simplified Motor model - Geometry Configuration	value	unit
r_1	0.007	m
r_2	0.03	m
r_3	0.031	m
r_4	0.038	m
r_5	0.05	m
r_6	0.25	m
α_{sector}	90	°

Table 4.8: Chosen measurements for geometry of the simplified motor model in COMSOL. The measurements were chosen according to . The idea of taking one sector for Topology Optimization approach was given by [46], as it can be applied as well on a symmetric composition as it is given here.

Electric motor analysed with Virtual Magnet Method

For the Virtual Magnet Method, the air gap flux density in equation 4.25 was applied to create minimal harmonic effects [6]. The mesh was set to be refined in the areas R_g and R_m where the optimization was applied, whereas in the stator area the mesh was held less fine.

The result of the simulation can be seen in figure 4.42.

$$\mathbf{B}_g = \sin(2 \cdot \varphi) \cdot \frac{1}{\sqrt{x^2 + y^2}} (x \cdot \hat{\mathbf{e}}_x + y \cdot \hat{\mathbf{e}}_y) \quad (4.25)$$

The field demonstrated in figure 4.42 resembles strongly the solution of the segmented approach in [6] for a four-pole motor.

Electric motor analysed with Topology Optimization Method and combined approach

Four objective functions were tested as well as the combined approach with specifically chosen objective functions.

Based on the representation and use of the mesh in [47] and [48] an additional twofold refinement of the triangles of the mesh, shown in figure 4.51, was made to examine the impact on the accuracy of the results especially in the areas where the optimization is performed.

$$\mathbf{B}_r = \theta_p \cdot B_{rem} \cdot [y \cdot \hat{\mathbf{e}}_x + x \cdot \hat{\mathbf{e}}_y] \quad (4.26)$$

The expression for the remanence flux density in equation 4.26 was adapted to the quarter of the motor circle that was investigated. For the recoil permeability, the same expression as for the examples before in this chapter was taken.

$$\mu_{rec} = 4000 - \theta_p \cdot (4000 - 1) \quad (4.27)$$

To make the data from table 4.9 and charts 4.44 more understandable, the magnetic flux density along the air gap for the observed quarter was plotted by splitting it up into three components: the total radial component in figure 4.45, the first harmonics in 4.46 and the residual parts in 4.47. This approach was taken from [8] and is based on using the Fourier series to plot the first harmonic of the radial component of the air gap flux density and the total component, as well as the rest terms, summarized in the third plot. Therefore, the

Simple Motor - mesh refinement number 1	\mathcal{M}	THD (%)
VMM	0.15725	0.349
TOM (Ξ_1)	0.073438	19.366
TOM (Ξ_2)	0.14984	0.492
TOM (Ξ_3)	0.14806	5.567
TOM (Ξ_4)	0.071091	19.639
TOM, VMM (Ξ_2)	0.10682	22.029
TOM, VMM (Ξ_4)	0.10685	22.296

Table 4.9: Representation of the calculated figure of merit \mathcal{M} for the mesh refinement 1 in COMSOL. For the analysis of TOM, the SIMP algorithm was used and changes of β and p_{SIMP} were made, the initial value $\theta_0 = 0.5$ and the projection point $\theta_\beta = 0.5$ was set by default and not changed in this case. The used optimality tolerance for TOM was 0.001, and a maximum of 100 iterations was set as a restriction.

THD (total harmonic distortion) can be calculated accordingly to [8] to effectively see the ratio of the distortion, as they vary in their amplitude. The THD is added to table 4.9 and 4.10. For better comparability, the colours of the plots are adapted to the different cases. Only for the relative error plots (4.49,4.57), the colour of the combined case with Ξ_4 and VMM was changed from turquoise dotted line to dark red line for better visibility.

For the analysis of this simple motor model, the focus laid on different objectives and mesh refinements rather than changing the other parameters.

Regarding the magnetic field plots in figure 4.44, the strongest field results were achieved through $\Xi_{2,3}$ (in 4.44b,4.44c). The results in 4.44e and 4.44f were clearly influenced by the Virtual Magnet Method from the magnet shape.

The table in 4.9 show the calculated results for \mathcal{M} and the THD . The row in yellow serves to highlight a good trade-off between a low THD value and high value for \mathcal{M} , which explains why Ξ_2 was taken for the combined approach.

For the objectives $\Xi_{2,3}$ the results of the figure of merit are in a similar range than the one of the Virtual Magnet Method. The value of the latter for the total harmonic distortion is in the same range like the result mentioned in [6] with 0.02. This counts only for \mathcal{M} , but not for the THD . The two combined models are in a similar range for \mathcal{M} as well as for the THD .

Regarding the total magnetic flux density and the first harmonics plotted in 4.45,4.46, results show similar behaviour of VMM and of $\Xi_{2,3}$, as well as $\Xi_{1,4}$. For the combined versions, a shift is noticeable which might correspond to the shifted magnet area in 4.50e and 4.50f.

This shift is as well notable for the residual plots in 4.47. The results of $\Xi_{1,4}$ correspond again, only Ξ_3 shows a higher ratio.

Figure 4.48 represents the plot of the relative change of the objective which are very aligned to each other, especially between the first ten iterations.

After the 40th iteration, all objectives remain on a plateau, which signifies no further improvement, however $\Xi_{1,4}$ show the least plateau and the highest values of all. In general, Ξ_2 has a higher objective than Ξ_3 over the whole iteration number Corresponding to the reached plateaus, the error plots decrease, which prefigures a good convergence of the solutions.

Regarding figure 4.49, only four cases were chosen to demonstrate the difference in the

converging error. The plots in pink and turquoise come from the topology optimized approach with the objectives Ξ_2 and Ξ_4 . The plots held in dashed dark blue and red are the combined approaches with the virtual magnet method, both using the two mentioned objectives. While Ξ_2 and the combination of *VMM* and Ξ_4 decay between iteration 60 and 80, the combination of *VMM* and Ξ_2 goes down right before iteration 100, whereas the turquoise plot ends up with a higher error value after 100 iterations.

As a predefined upper boundary is set for the convergence error, its limit can be clearly seen as a plateau at 0.5.

The magnet areas in 4.50 highlight the prior explanations about the discussed results, as $\Xi_{1,3}$ are similar, as so are $\Xi_{2,3}$ and the combined results. The small areas of $\Xi_{1,4}$ also mirror the lower maximal radial component of the flux density, as well as the visible shift in amplitude for the combined versions can be explained by the resulted magnet area.

Simple Motor - mesh refinement number 2	\mathcal{M}	THD (%)
VMM	0.15725	0.349
TOM (Ξ_1)	0.11847	14.041
TOM (Ξ_2)	0.12190	2.0221
TOM (Ξ_3)	0.15096	13.101
TOM (Ξ_4)	0.11701	15.674
TOM, VMM (Ξ_2)	0.11275	15.5334
TOM, VMM (Ξ_4)	0.11963	19.889

Table 4.10: Representation of the calculated figure of merit \mathcal{M} for the number of mesh refinement 2 in COMSOL. The refinement process did not change any result from the virtual magnet method compared to the prior refinement number, so it only affected the results for Topology Optimization. For the latter, SIMP algorithm was used and changes of β and p_{SIMP} were made, the initial value $\theta_0 = 0.5$ and the projection point $\theta_\beta = 0.5$ was set by default and not changed in this case. The used optimality tolerance for TOM was 0.001, and a maximum of 100 iterations was set as a restriction.

For the second approach of refinement number 2, the results were the same for the Virtual Magnet Method both for the calculated values in the table as well as for the plots. As well as before, the colour of the combined version for Ξ_4 , *VMM* in the relative error plot 4.57 was changed from turquoise dotted line to dark red line as of visibility reason.

The magnetic field norm plots in figure 4.52 is general lower than in the former example with refinement number 1. The only remarkable difference is that $\Xi_{1,2,4}$ are similar here compared to the prior example.

Regarding the results for the *THD* in table 4.10, $\Xi_{1,4}$ improved, whereas $\Xi_{2,3}$ increased. Especially the combination Ξ_2 with *VMM* improved and a remarkable difference between Ξ_2 and Ξ_3 is noticeable. The values for \mathcal{M} improved for all values, except for the result of Ξ_2 which decreased and the Ξ_3 and *VMM* stayed the same.

The radial component of the flux density in figure 4.53 shows again an alignment of $\Xi_{1,4}$. For both combinations an alignment is only visible for the first harmonic plot in 4.54, for the total component the influence of the slight plateau of Ξ_2 has an impact on the combination with Ξ_2 and *VMM*.

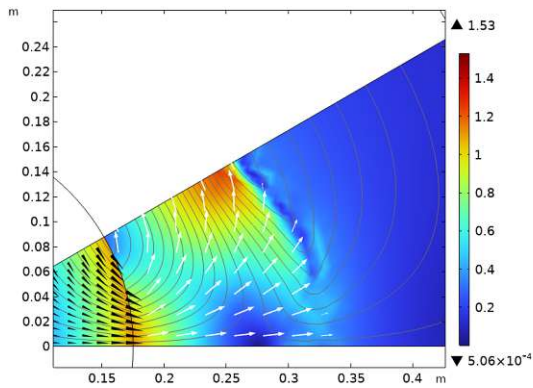
Very remarkable is the plateau of both results $\Xi_{2,3}$. Compared to the former results of refinement number 1, the plots are generally more spread and partly lower in their amplitude, as already the plotted flux density norm stated it.

For the residual plot in figure 4.55, a clear influence of Ξ_2 can be seen on the combination with Ξ_2 and *VMM*. The other plots here are as well more spread than the results of refinement number 1 in figure 4.47.

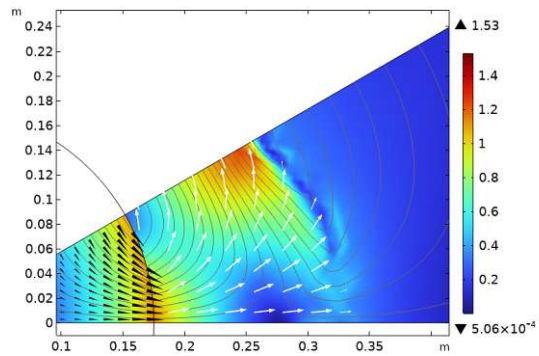
The objective plots in figure 4.56 possibly indicates that the change of the mesh influenced the progress of the objective in terms of less plateaus, except for Ξ_3 . In general, both combinations improved, as well the values increased in general. Specifically Ξ_2 aligns with the combination of Ξ_2 and *VMM*, the combination with Ξ_4 approaches the objective of Ξ_4 .

Comparing the convergence plot in figure 4.57 with figure 4.49, an increase of the overall relative error is visible, as well as the set boundary of 0.5. Compared to the plotted cases, Ξ_4 shows the lowest value.

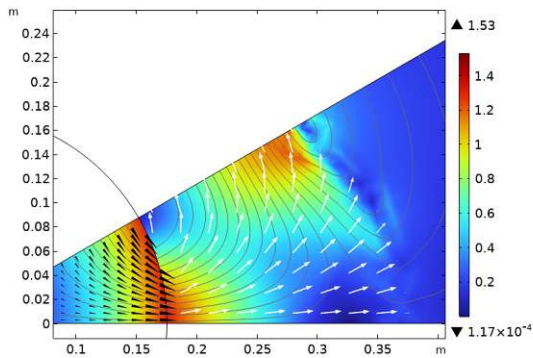
The magnet area in figure 4.58 demonstrates a bigger difference in shape between the two combinations, as well as the areas of $\Xi_{2,3}$ reduced in size and changed in shape.



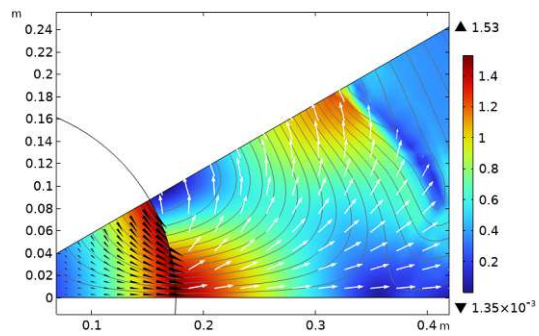
(a) Ξ_1 , projection slope $\beta = 8$, p_{SIMP} set by default.



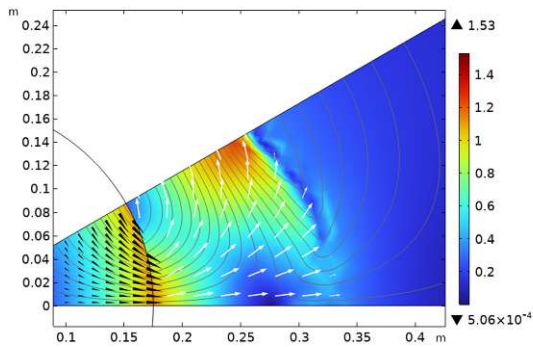
(b) Ξ_2 , projection slope $\beta = 8$, p_{SIMP} set by default.



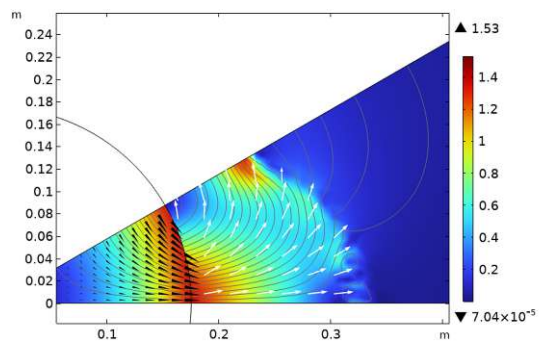
(c) Ξ_3 , projection slope $\beta = 14$, p_{SIMP} set by default.



(d) Ξ_4 , projection slope $\beta = 8$, p_{SIMP} set by default.

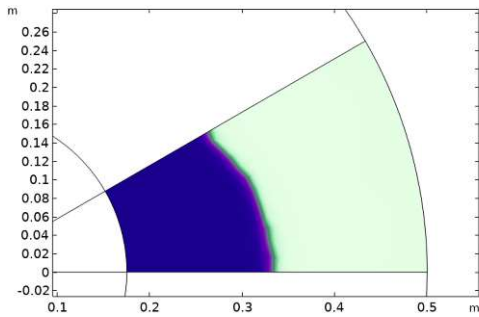


(e) Ξ_2 , projection slope $\beta = 13$, p_{SIMP} set by default.

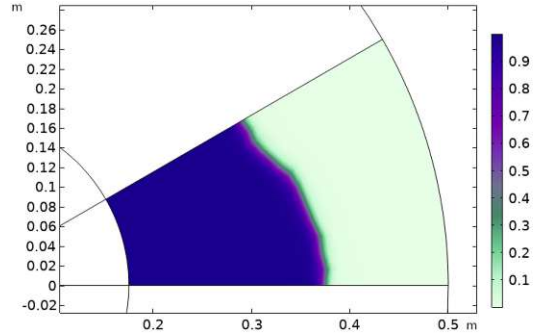


(f) Ξ_2 , projection slope $\beta = 20$, p_{SIMP} set by default.

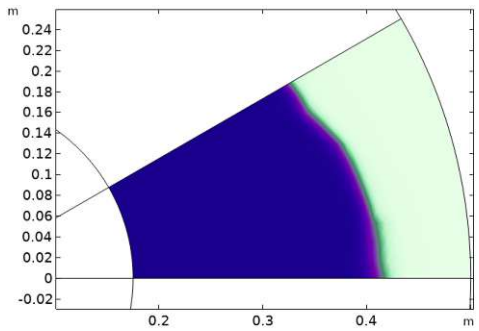
Figure 4.13: Sextupole Magnet analysed with the Topology Optimization Method with SIMP algorithm: The colour bar serves as a demonstration of the norm of the magnetic field, given in Tesla. The black arrows in cone-shape show the plotted objective function in the region R_g . The white arrows represent the remanence flux density of the magnetic field in the design area R_m . The projection point $\theta_\beta = 0.5$ and the initial value for the control variable was set to $\theta_0 = 0.5$ were used for all cases.



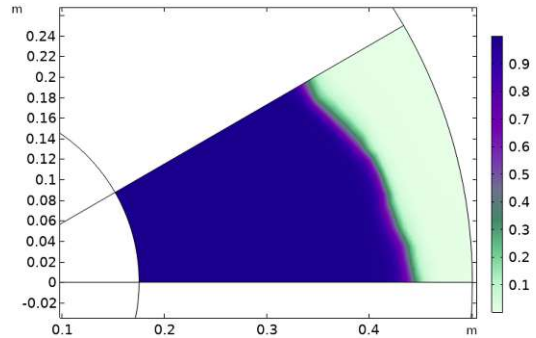
(a) Ξ_1 , projection slope $\beta = 8$, p_{SIMP} set by default.



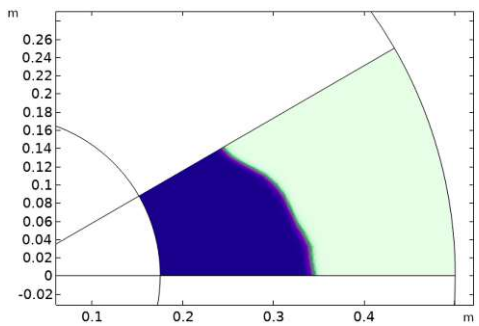
(b) Ξ_2 , projection slope $\beta = 8$, p_{SIMP} set by default.



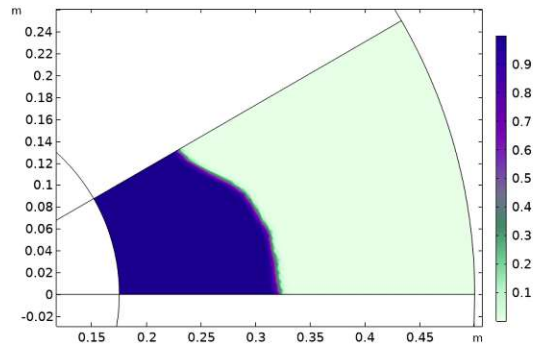
(c) Ξ_3 , projection slope $\beta = 8$, p_{SIMP} set by default.



(d) Ξ_4 , projection slope $\beta = 8$, p_{SIMP} set by default.



(e) Ξ_2 , projection slope $\beta = 13$, p_{SIMP} set by default.



(f) Ξ_2 , projection slope $\beta = 20$, p_{SIMP} set by default.

Figure 4.14: Sextupole Magnet analysed with the Topology Optimization Method with SIMP algorithm: The colour bar here serves as the indicator between magnet material above 0.5 and iron under this threshold level.

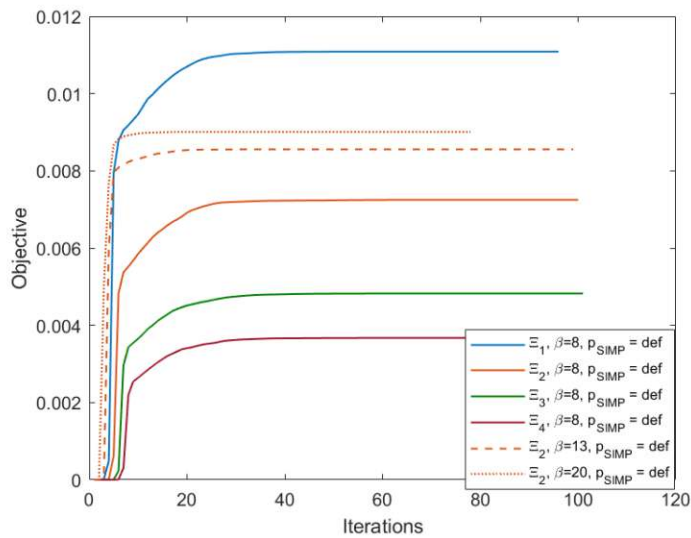


Figure 4.15: Objective function evaluations plotted over the total iterations made for the individual cases that were mentioned in table 4.2.

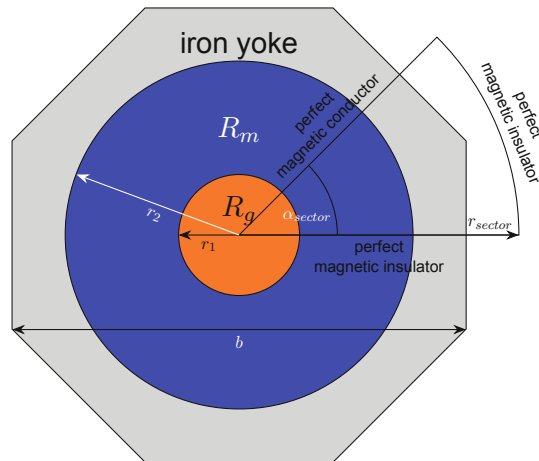


Figure 4.16: This schematic figure serves as a model for the quadrupole and sextupole magnet [6]. The orange area in the middle defines the virtual magnet, the blue circle around represents the design area, in this case the real permanent magnet, and the grey square around serves as an iron yoke. The circle segment should demonstrate the sector that is used for applying Topology Optimization Method for the two models, as a symmetric object is observed. The proper boundary conditions are mentioned for the sector sides.

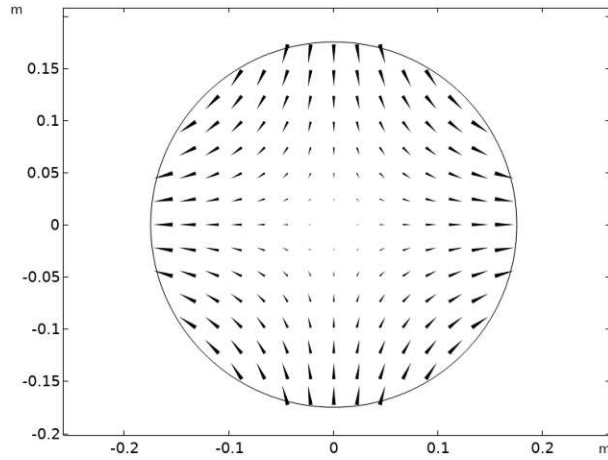


Figure 4.17: Ideal not-skewed field distribution in the center of the quadrupole magnet geometry. To have a comparison to the plots with TOM, for the y component a minus sign was added to let the field arrows point inwards the inner circle.

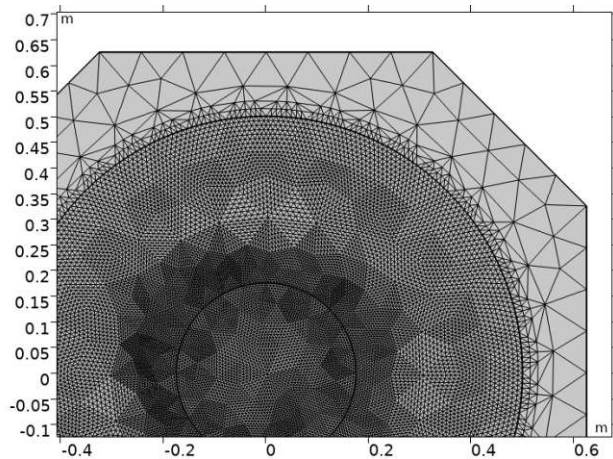


Figure 4.18: Mesh setup for Virtual Magnet Method for the quadrupole geometry. As of symmetry reasons, not the whole geometry is shown here. The refinement number of 3 was applied on the areas R_g and R_m .

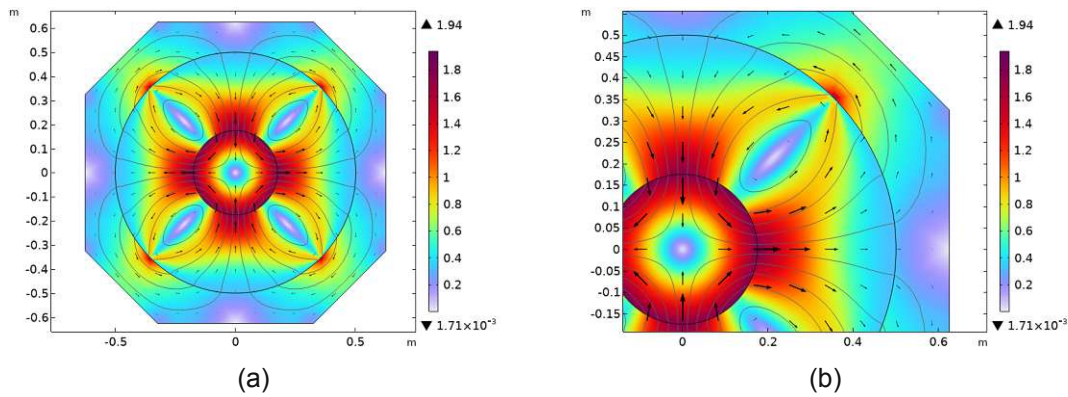


Figure 4.19: Quadrupole Magnet optimized in permanent magnet material usage with the Virtual Magnet Method for a not-skewed field. The contour plot, here demonstrated with grey-colored lines, represent the z -component of the magnetic vector potential A_z . The black arrows demonstrate the magnetic flux within the design area in its x and y direction. The colour bar serves as a demonstration of the norm of the magnetic flux density, given in Tesla.

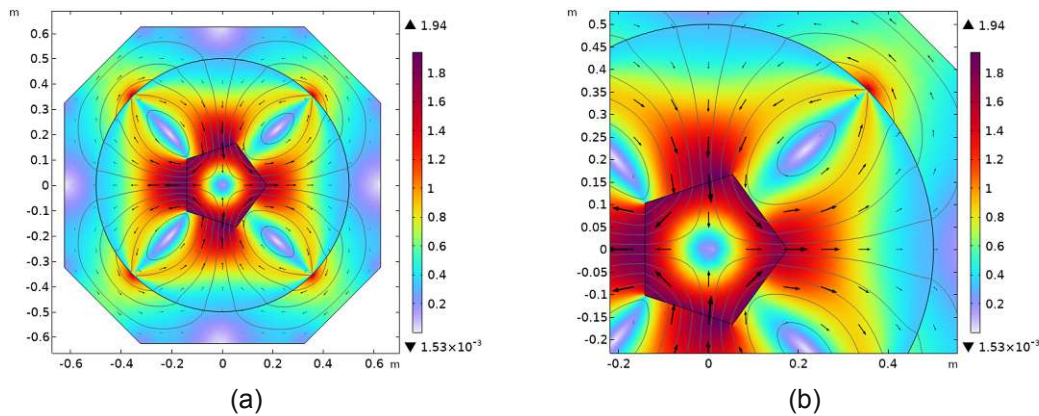


Figure 4.20: Quadrupole Magnet optimized in permanent magnet material usage with the Virtual Magnet Method for a not-skewed field for a pentagonal shaped R_g . The contour plot, here demonstrated with grey-colored lines, represent the z -component of the magnetic vector potential A_z . The black arrows demonstrate the magnetic flux within the design area in its x and y direction. The colour bar serves as a demonstration of the norm of the magnetic flux density, given in Tesla.

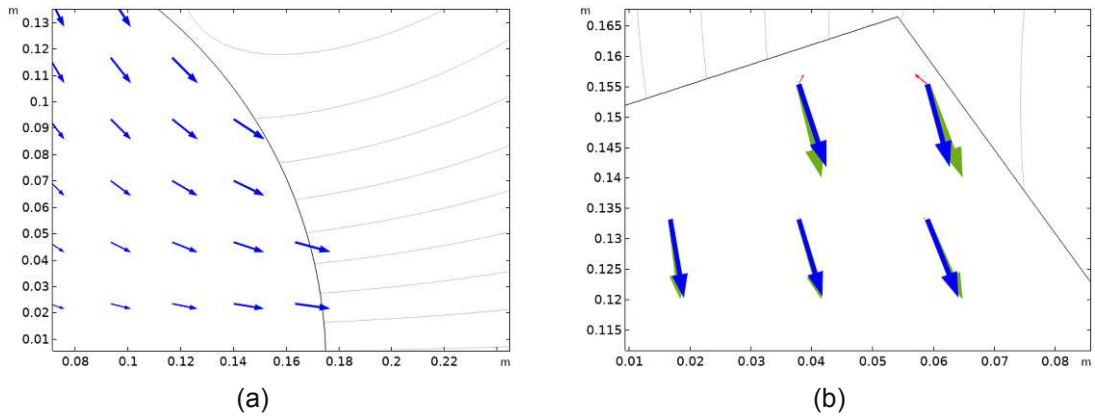


Figure 4.21: A cutout of the not-skewed field of the circular R_g in figure 4.21a and of the pentagonal shaped R_g in figure 4.21b. The contour plot, here demonstrated with grey-colored lines, represent the z-component of the magnetic vector potential A_z .

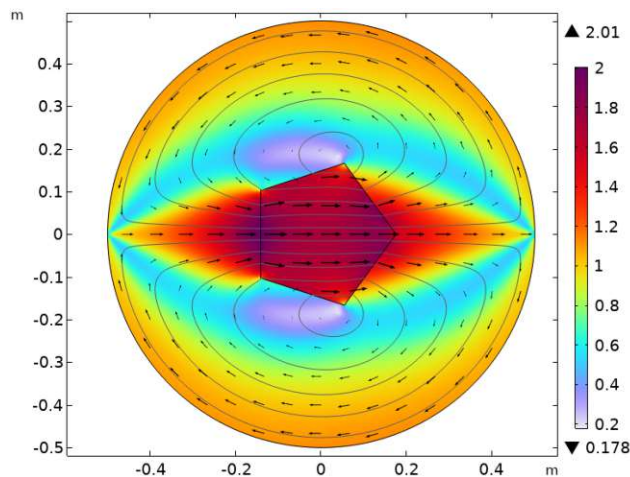
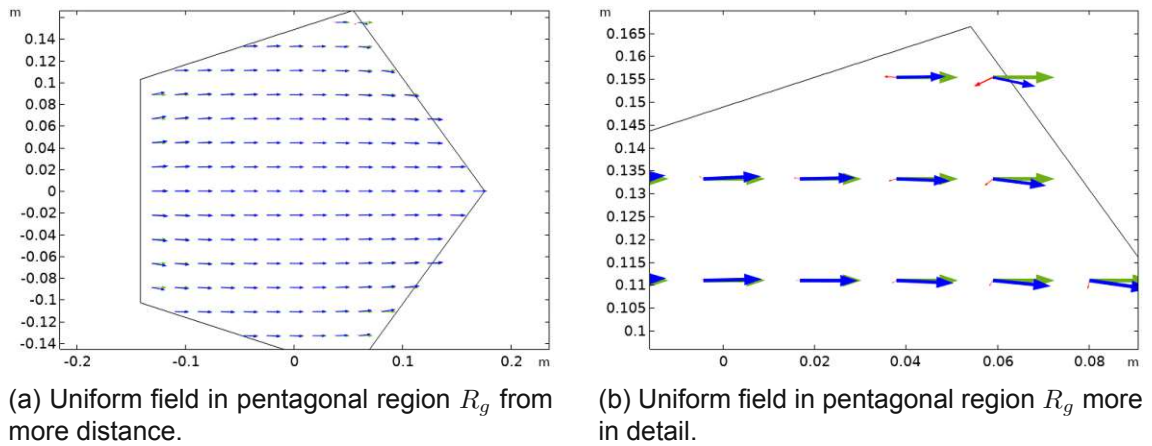


Figure 4.22: Comparison of virtual magnet method results with uniform field distribution. As the previous example, a pentagonal virtual magnet area was chosen to show the limits of the method.

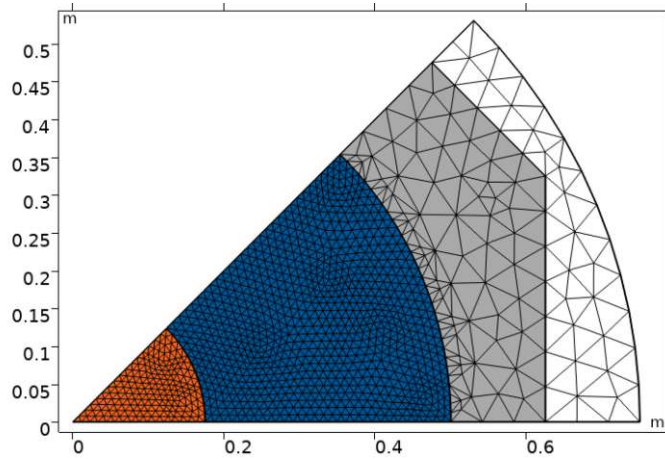
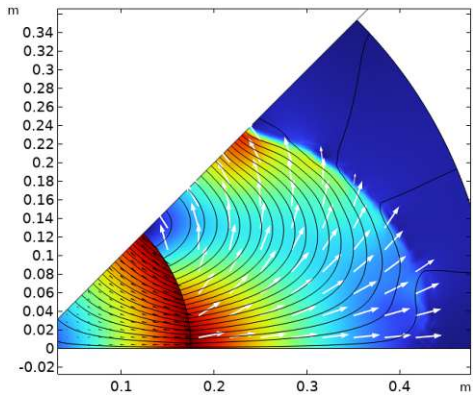
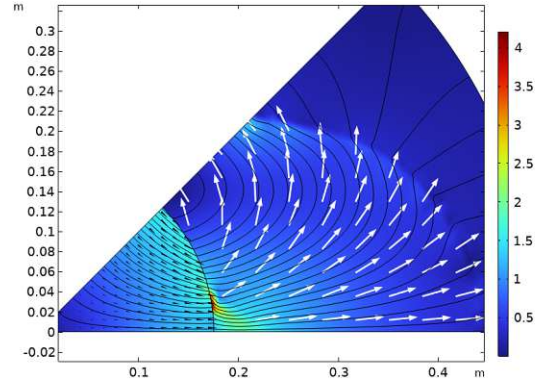


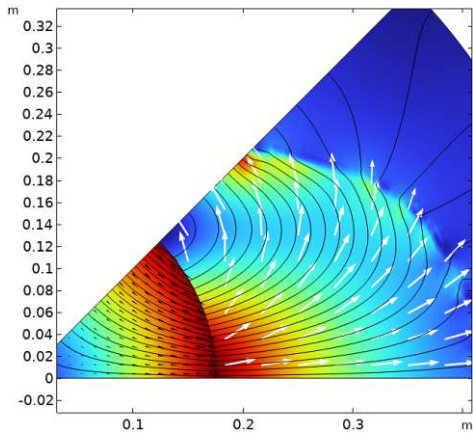
Figure 4.23: Mesh setup for applying Topology Optimization Method for the 45° sector for the quadrupole design. A refinement number of 2 was applied to the areas that are analysed, the iron core around the design area was not taken into account.



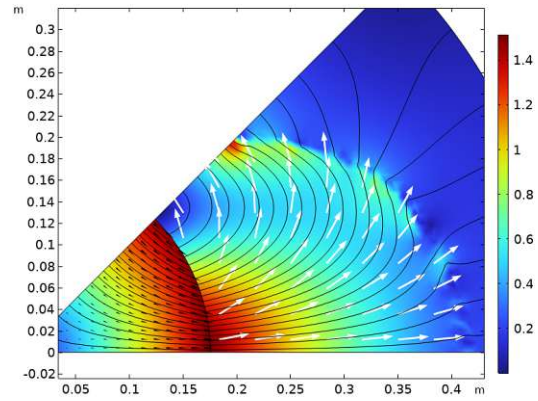
(a) Projection slope $\beta = 8$, p_{SIMP} set by default.



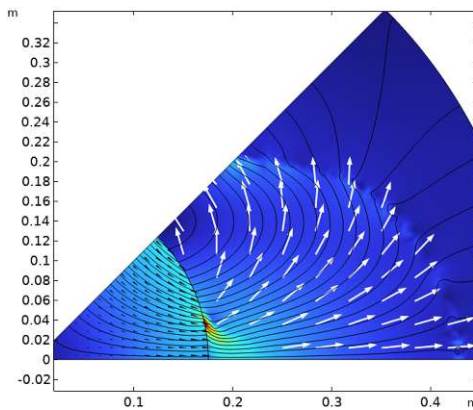
(b) Projection slope $\beta = 14$, $p_{SIMP} = 2$.



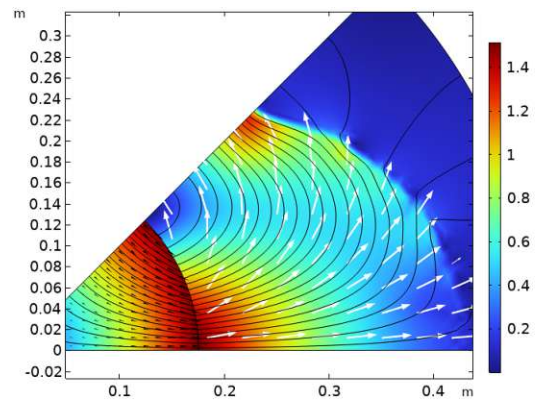
(c) Projection slope $\beta = 14$, $p_{SIMP} = 2.5$.



(d) Projection slope $\beta = 20$, $p_{SIMP} = 2$.

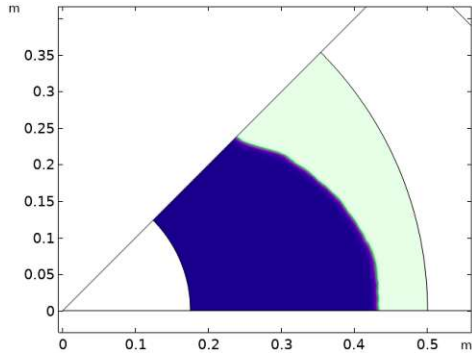


(e) Projection slope $\beta = 25$, $p_{SIMP} = 2$.

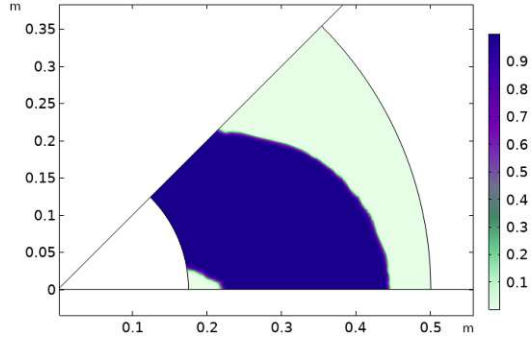


(f) Projection slope $\beta = 9$, $p_{SIMP} = 1.5$.

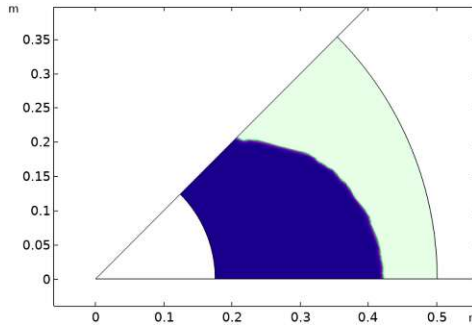
Figure 4.24: Quadrupole Magnet analysed with the Topology Optimization Method with SIMP algorithm: The colour bar serves as a demonstration of the norm of the magnetic field, given in Tesla. The red arrows show the plotted objective function in the region R_g . The white arrows represent the remanence flux density of the magnetic field in the design area R_m . The projection point $\theta_\beta = 0.5$ and the initial value for the control variable was set to $\theta_0 = 0.5$ were used for all cases.



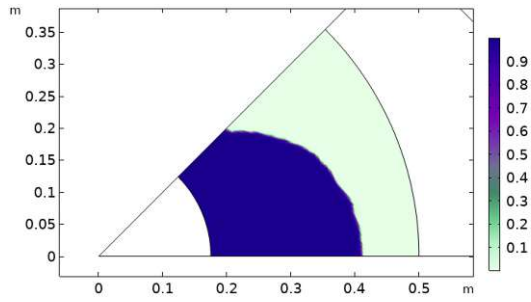
(a) Projection slope $\beta = 8$, p_{SIMP} set by default.



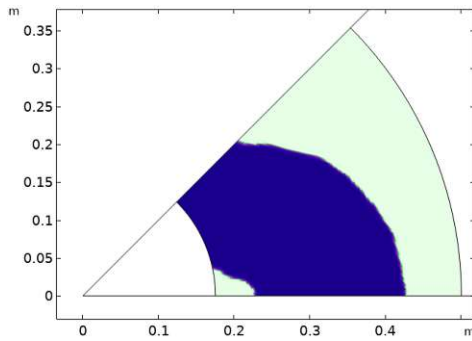
(b) Projection slope $\beta = 14$, $p_{SIMP} = 2$.



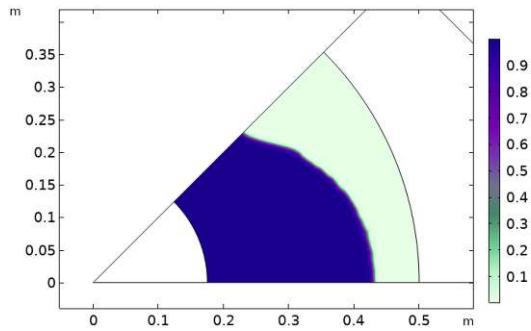
(c) Projection slope $\beta = 14$, $p_{SIMP} = 2.5$.



(d) Projection slope $\beta = 20$, $p_{SIMP} = 2$.



(e) Projection slope $\beta = 25$, $p_{SIMP} = 2$.



(f) Projection slope $\beta = 9$, $p_{SIMP} = 1.5$.

Figure 4.25: Quadrupole Magnet analysed with the Topology Optimization Method with SIMP algorithm: The colour bar here serves as the indicator between magnet material above 0.5 and iron under this threshold level.

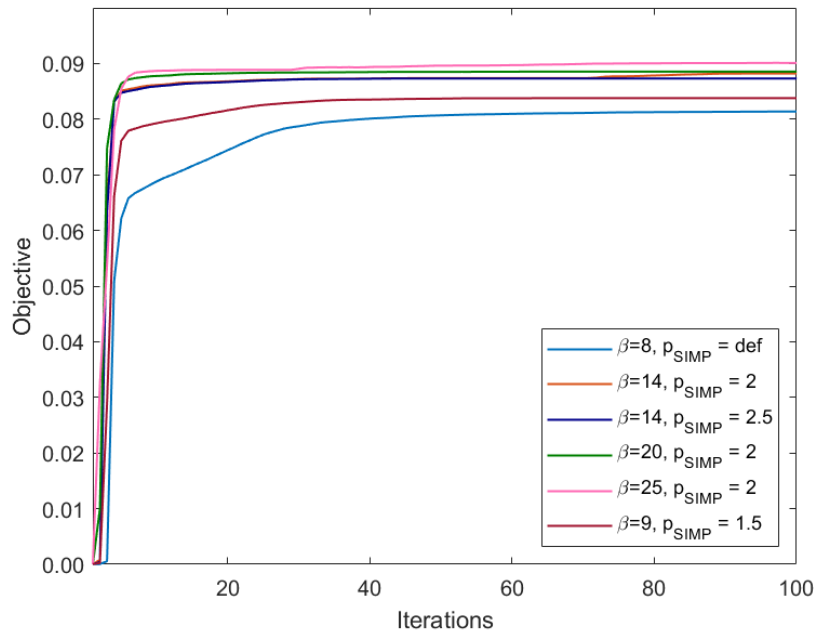


Figure 4.26: Objective function evaluations plotted over the total iterations made for the individual cases that were mentioned in table 4.4.

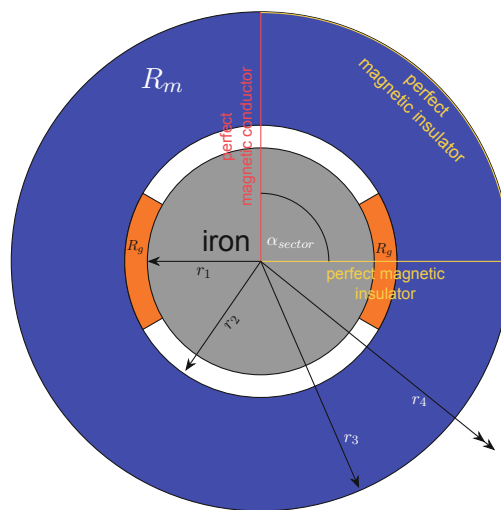
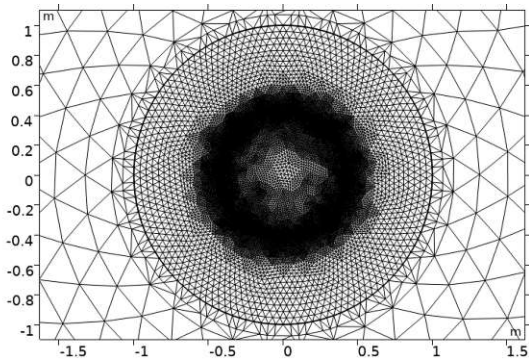
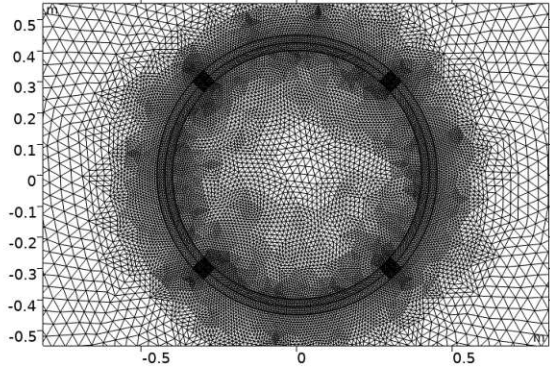


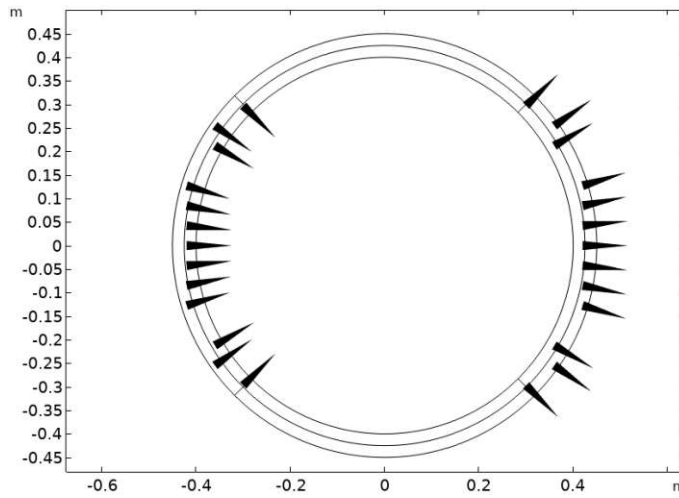
Figure 4.27: This schematic figure serves as a model for magnet refrigeration [6]. The orange areas on the sides define the virtual magnet, the blue circle around represents the design area, in this case the real permanent magnet, and the grey circle in the middle serves as the iron core.



(a) Mesh plotted for entire geometry with refinement number 2.



(b) Mesh plotted for inner circles including radius r_2 .



(c) Ideal field for magnetic refrigeration in two air gaps on each side, represented by red arrow plot. The figure only shows until the radius r_2 .

Figure 4.28: Mesh defined for analysis in 4.28a, 4.28b and ideal field plot.

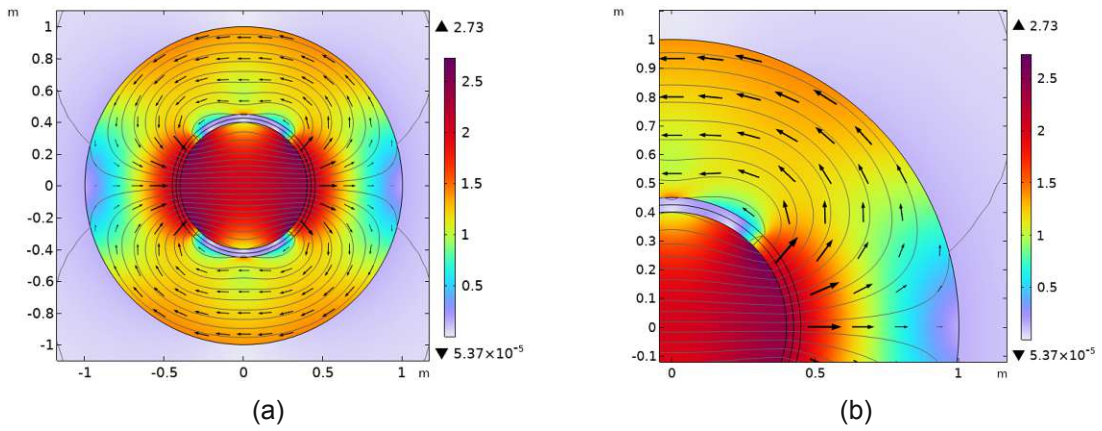


Figure 4.29: Magnetic refrigeration optimized in permanent magnet material usage with the Virtual Magnet Method. The contour plot, here demonstrated with grey-colored lines, represent the z -component of the magnetic vector potential A_z . The black arrows demonstrate the magnetic flux within the design area in its x and y direction. The colour bar serves as a demonstration of the norm of the magnetic flux density, given in Tesla.

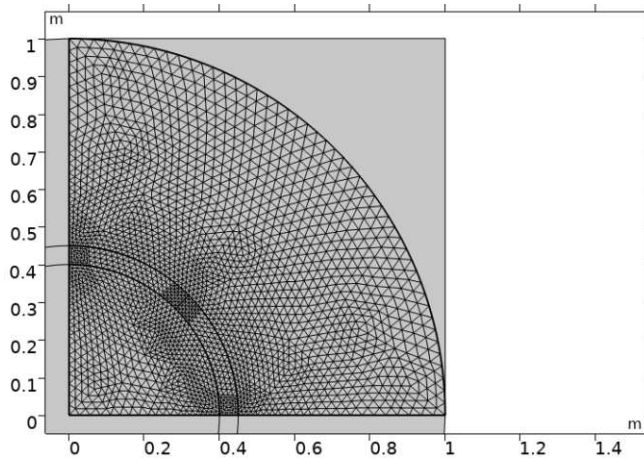
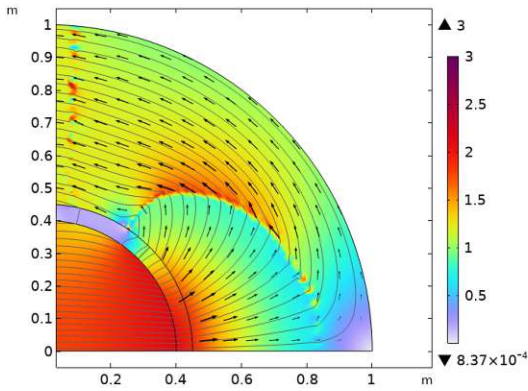
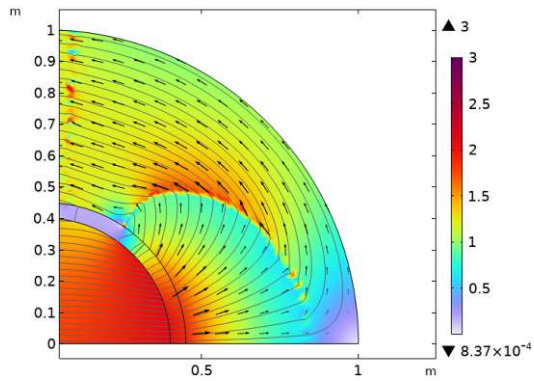


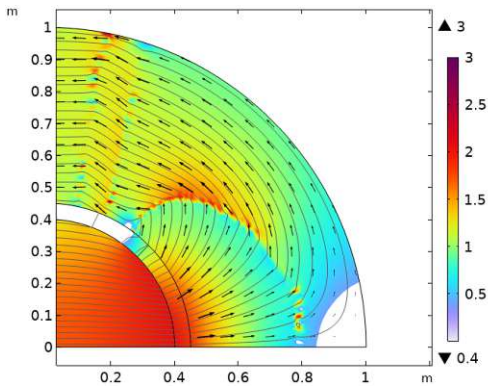
Figure 4.30: Mesh setup for applying Topology Optimization Method for the 90° sector for magnetic refrigeration design. A refinement number of 2 was used here as well.



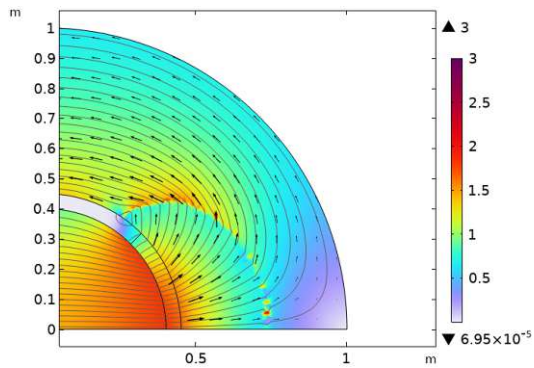
(a) Projection slope $\beta = 8$, p_{SIMP} set, Ξ_1 .



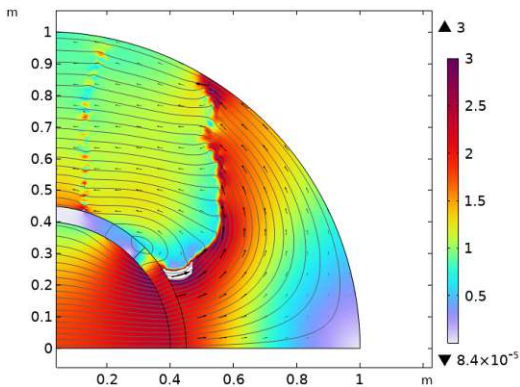
(b) Projection slope $\beta = 8$, p_{SIMP} set, Ξ_2 .



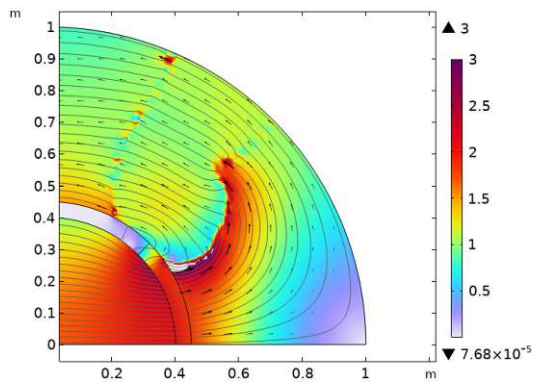
(c) Projection slope $\beta = 14$, p_{SIMP} set, Ξ_1 .



(d) Projection slope $\beta = 14$, p_{SIMP} set, Ξ_2 .



(e) Projection slope $\beta = 8$, p_{SIMP} set, Ξ_1 , VMM



(f) Projection slope $\beta = 8$, p_{SIMP} set, Ξ_2 , VMM

Figure 4.31: Magnetic refrigeration analysed with Topology Optimization Method with SIMP algorithm and the combination with VMM. The colour bar serves as a demonstration of the norm of the magnetic field, given in Tesla. The black arrows represent the flux density of the magnetic field in the design area R_m . The projection point θ_β and initial value for the control variable θ_0 were set to 0.5 and used for all cases.

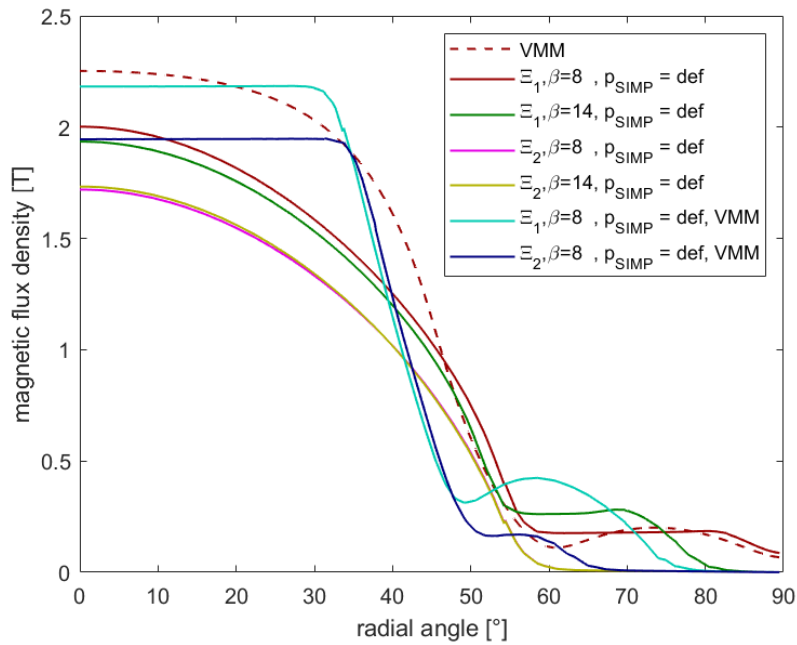


Figure 4.32: Magnetic flux density plots for the observed cases mentioned in table 4.6 for the VMM, the SIMP algorithm and the combined approaches. The plots were taken along the middle line displayed in figure 4.28c and 4.29b. $p_{SIMP} = def$ means the predefined value which is automatically set by COMSOL and the angle 0 is defined at the high field region direction and counting counterclockwise.

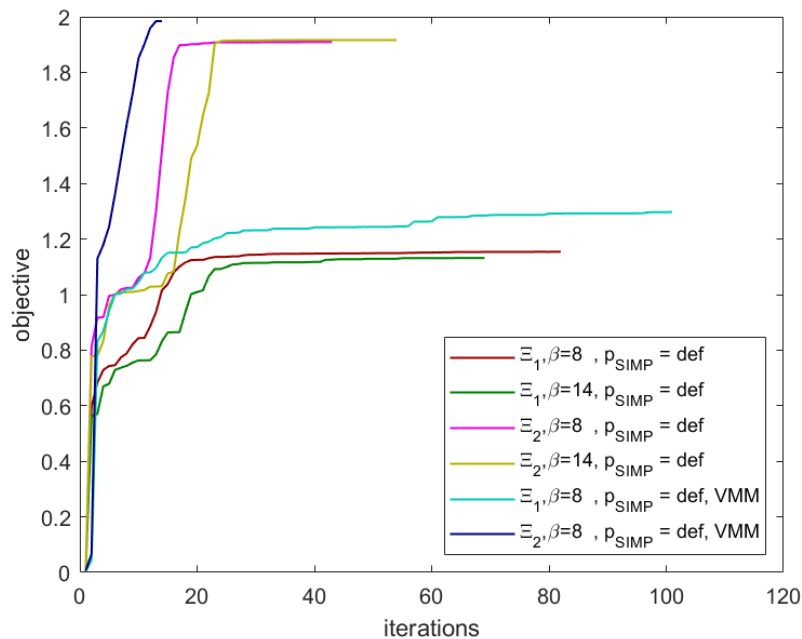


Figure 4.33: Objective plots for the observed cases mentioned in table 4.6 for the SIMP algorithm.

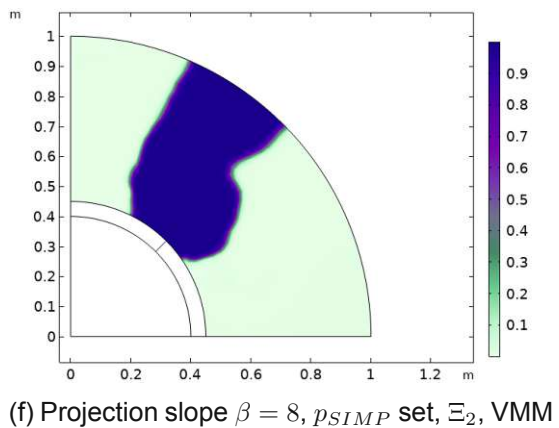
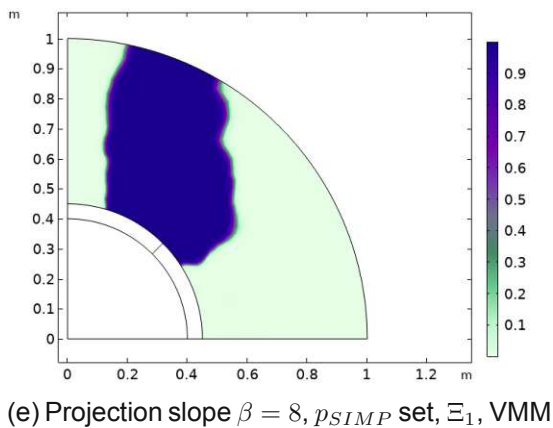
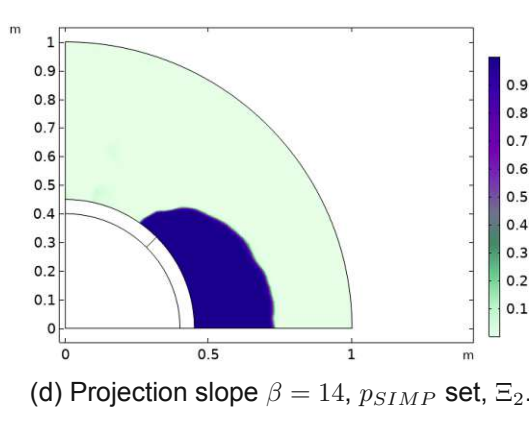
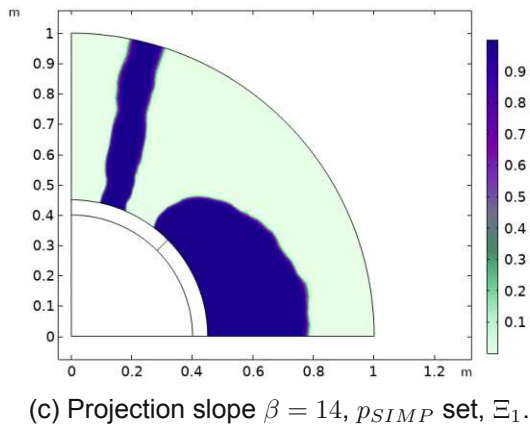
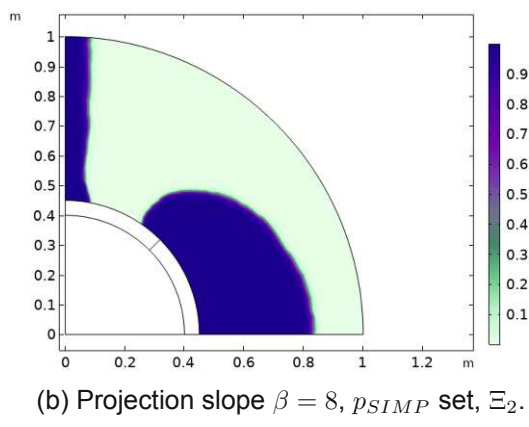
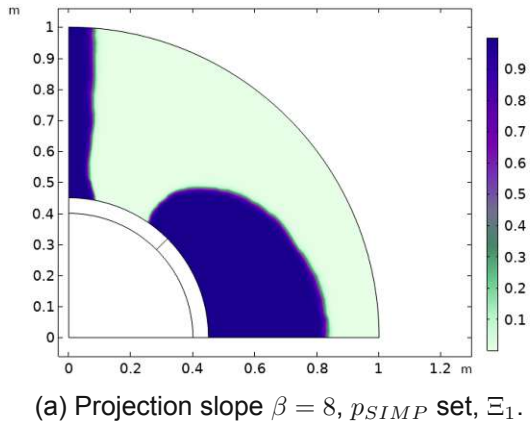


Figure 4.34: Magnet shape for magnetic refrigeration analysed with Topology Optimization Method with SIMP algorithm and the combination with VMM.

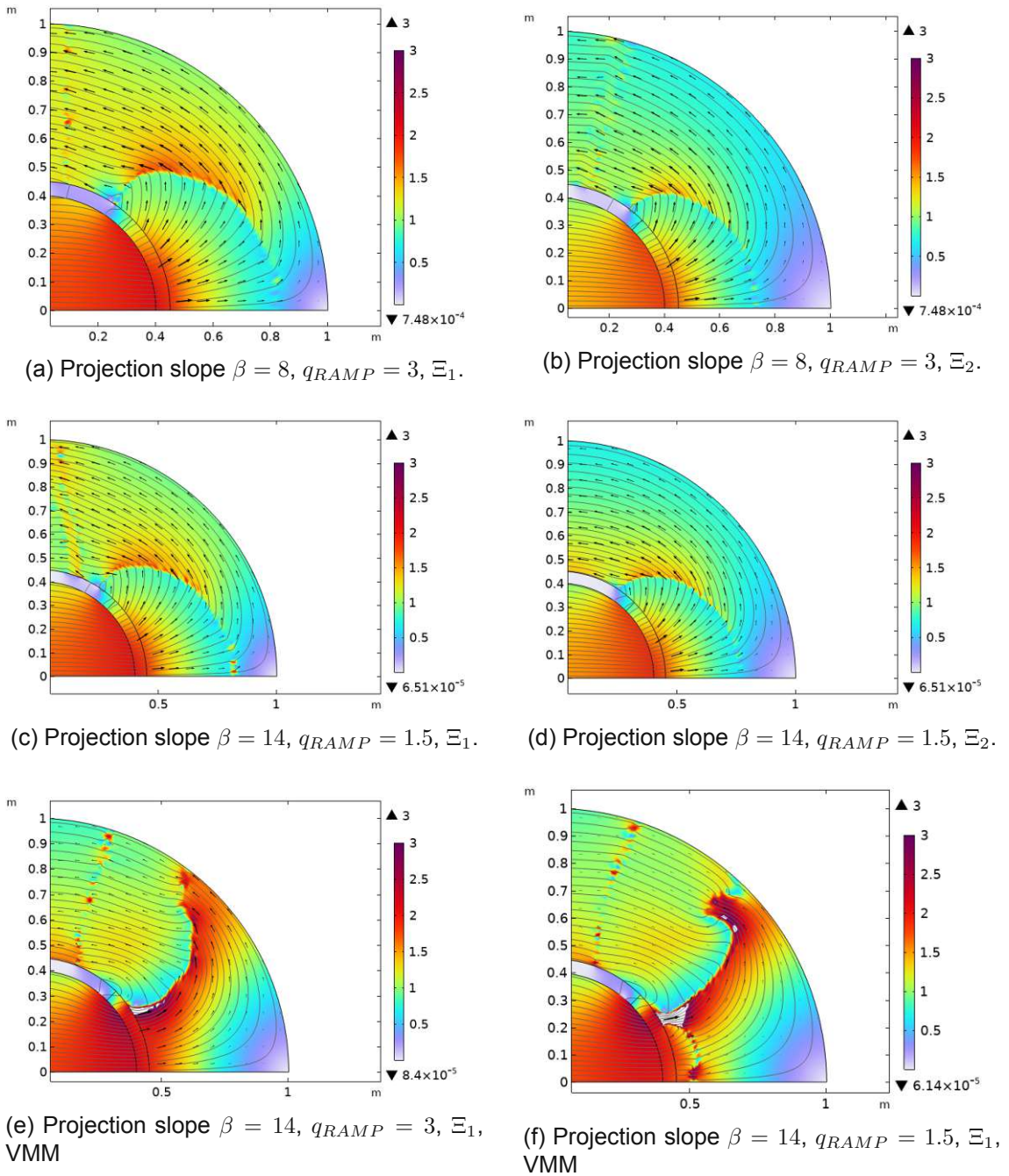
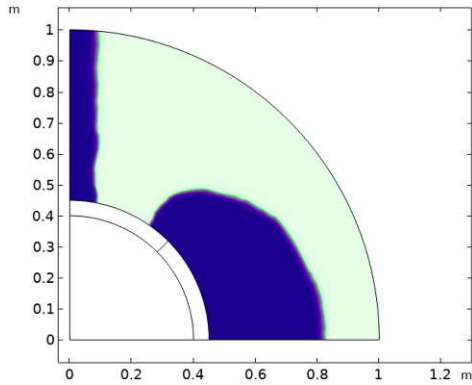
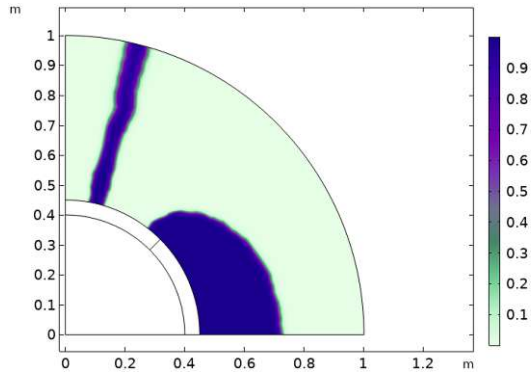


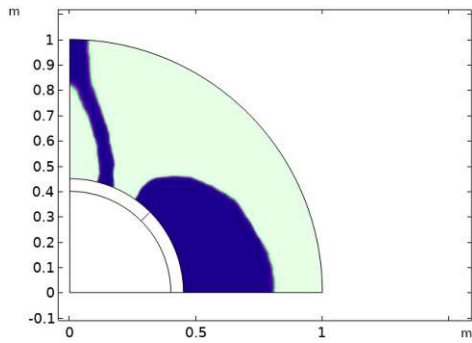
Figure 4.35: Magnetic refrigeration analysed with Topology Optimization Method with RAMP algorithm and the combination with VMM. The colour bar in 4.31 serves as a demonstration of the norm of the magnetic field, given in Tesla. The black arrows represent the flux density of the magnetic field in the design area R_m . The projection point θ_β and initial value for the control variable θ_0 were set to 0.5 and used for all cases.



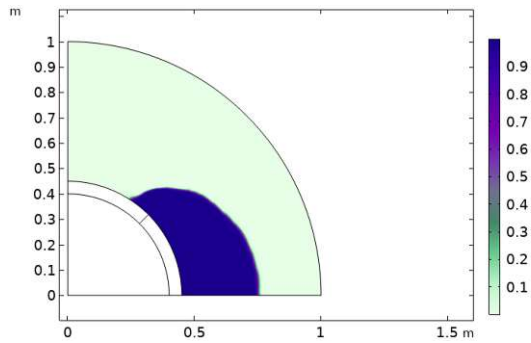
(a) Projection slope $\beta = 8$, $q_{RAMP} = 3$, Ξ_1 .



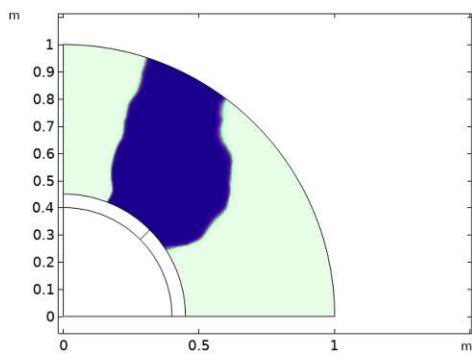
(b) Projection slope $\beta = 8$, $q_{RAMP} = 3$, Ξ_2 .



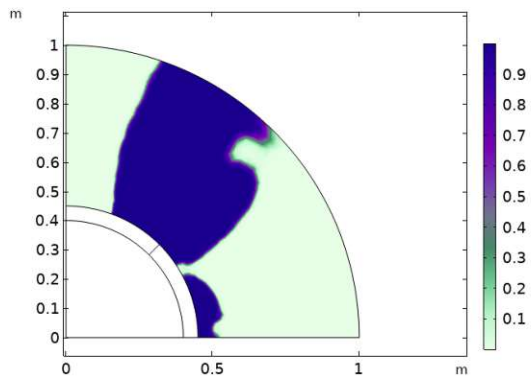
(c) Projection slope $\beta = 14$, $q_{RAMP} = 1.5$, Ξ_1 .



(d) Projection slope $\beta = 14$, $q_{RAMP} = 1.5$, Ξ_2 .



(e) Projection slope $\beta = 14$, $q_{RAMP} = 3$, Ξ_1 , VMM



(f) Projection slope $\beta = 14$, $q_{RAMP} = 1.5$, Ξ_1 , VMM

Figure 4.36: Magnet shape for magnetic refrigeration analysed with Topology Optimization Method with RAMP algorithm and the combination with VMM.

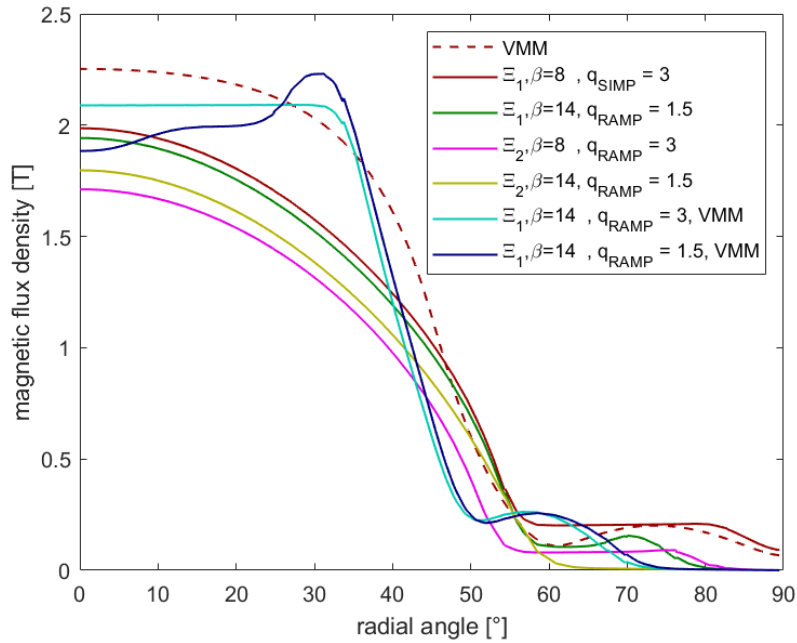


Figure 4.37: Magnetic flux density plots for the observed cases mentioned in table 4.7 for the VMM, the RAMP algorithm and the combined approaches. The plots were taken along the middle line displayed in figure 4.28c and 4.29b, defining the angle 0 at the high field region direction and counting counterclockwise.

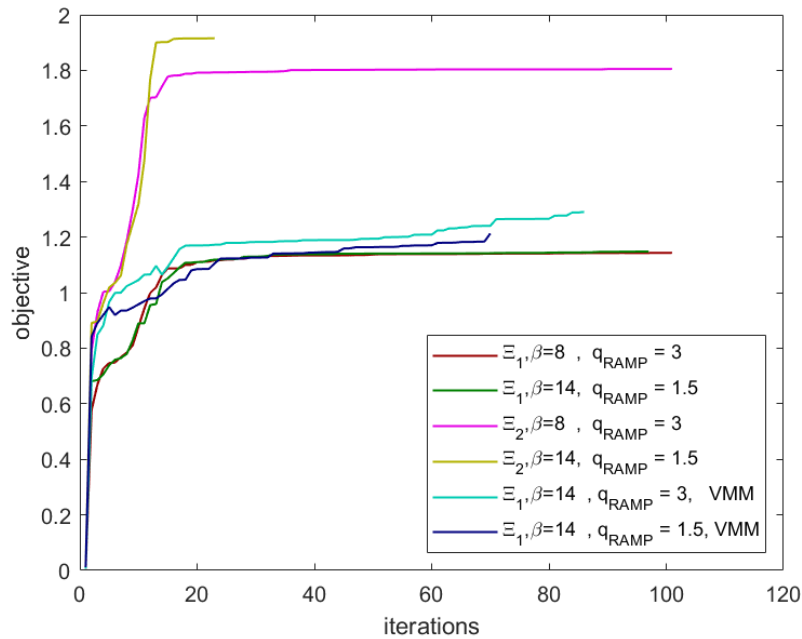


Figure 4.38: Objective plots for the observed cases mentioned in table 4.7 for the RAMP algorithm.

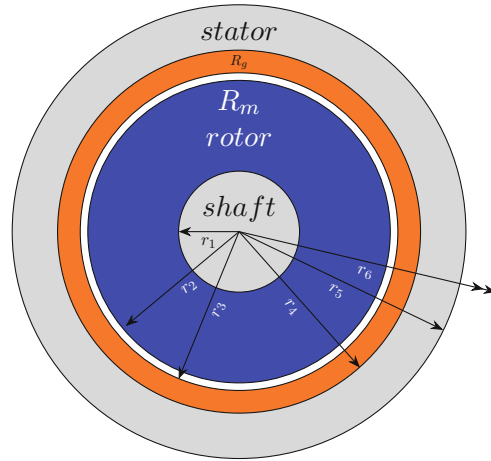


Figure 4.39: Schematic for simple electric motor model, inspired by the motor model of [5].

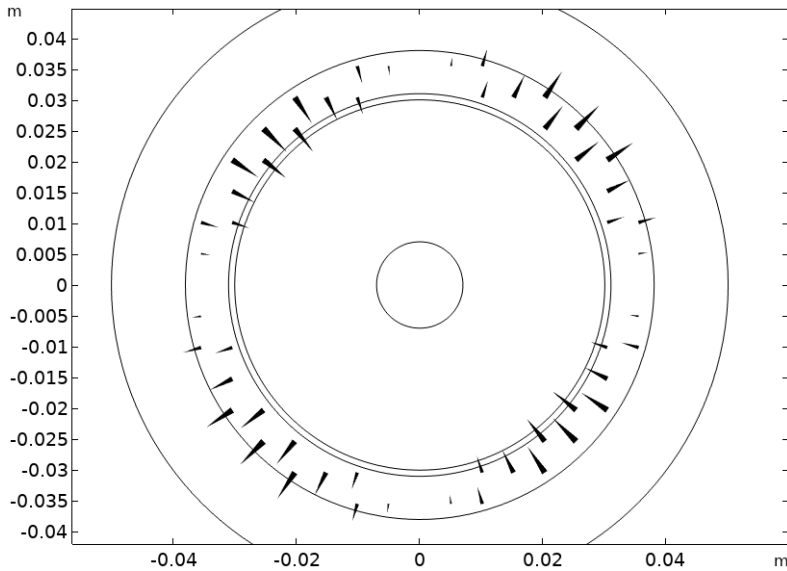


Figure 4.40: Ideal field distribution for simple motor model, plotted within the region of R_g .

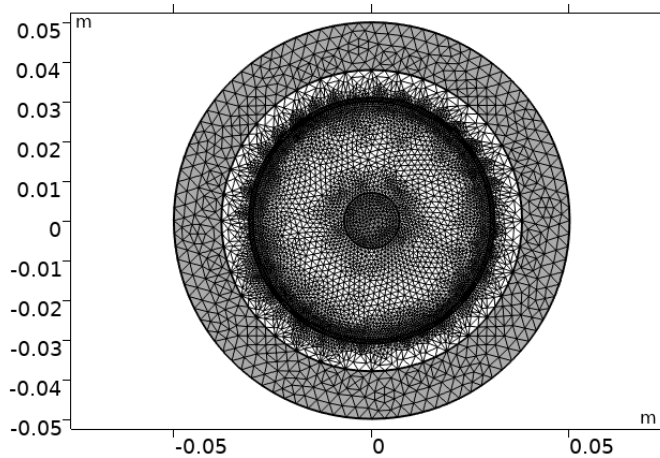


Figure 4.41: Mesh setup for Virtual Magnet Method for simple motor model. The refinement of the mesh was done within the areas R_g and R_m .

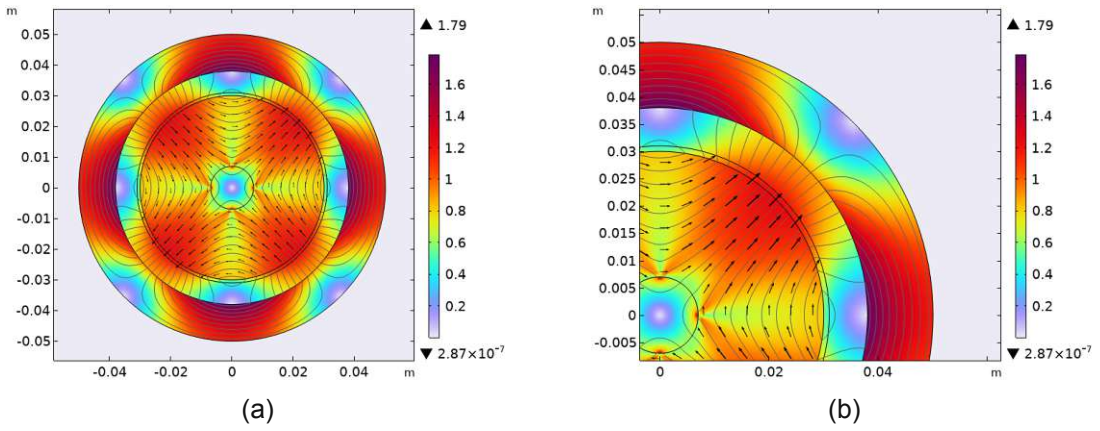


Figure 4.42: Simplified motor model optimized in permanent magnet material usage with the Virtual Magnet Method. The contour plot, here demonstrated with grey-colored lines, represent the z -component of the magnetic vector potential A_z . The black arrows demonstrate the magnetic flux within the design area in its x and y direction. The colour bar serves as a demonstration of the norm of the magnetic flux density, given in Tesla.

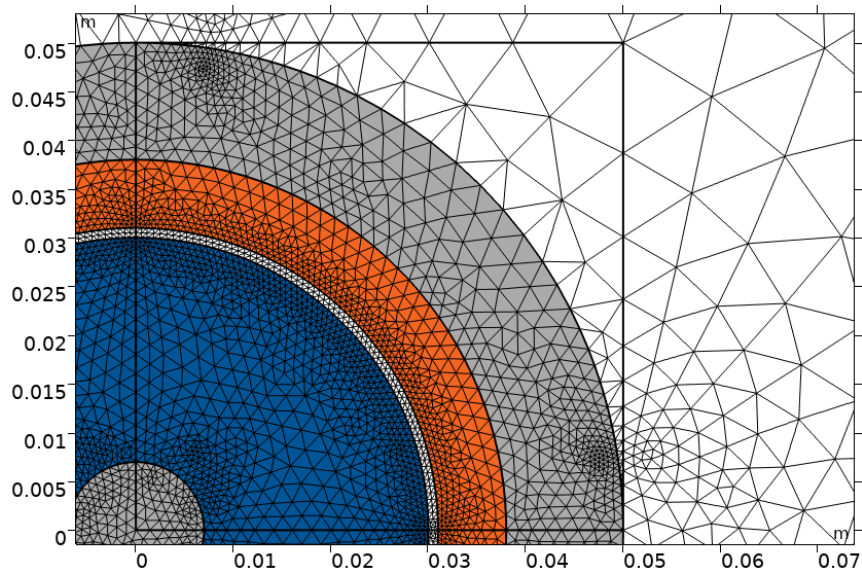


Figure 4.43: Mesh refinement number 1.

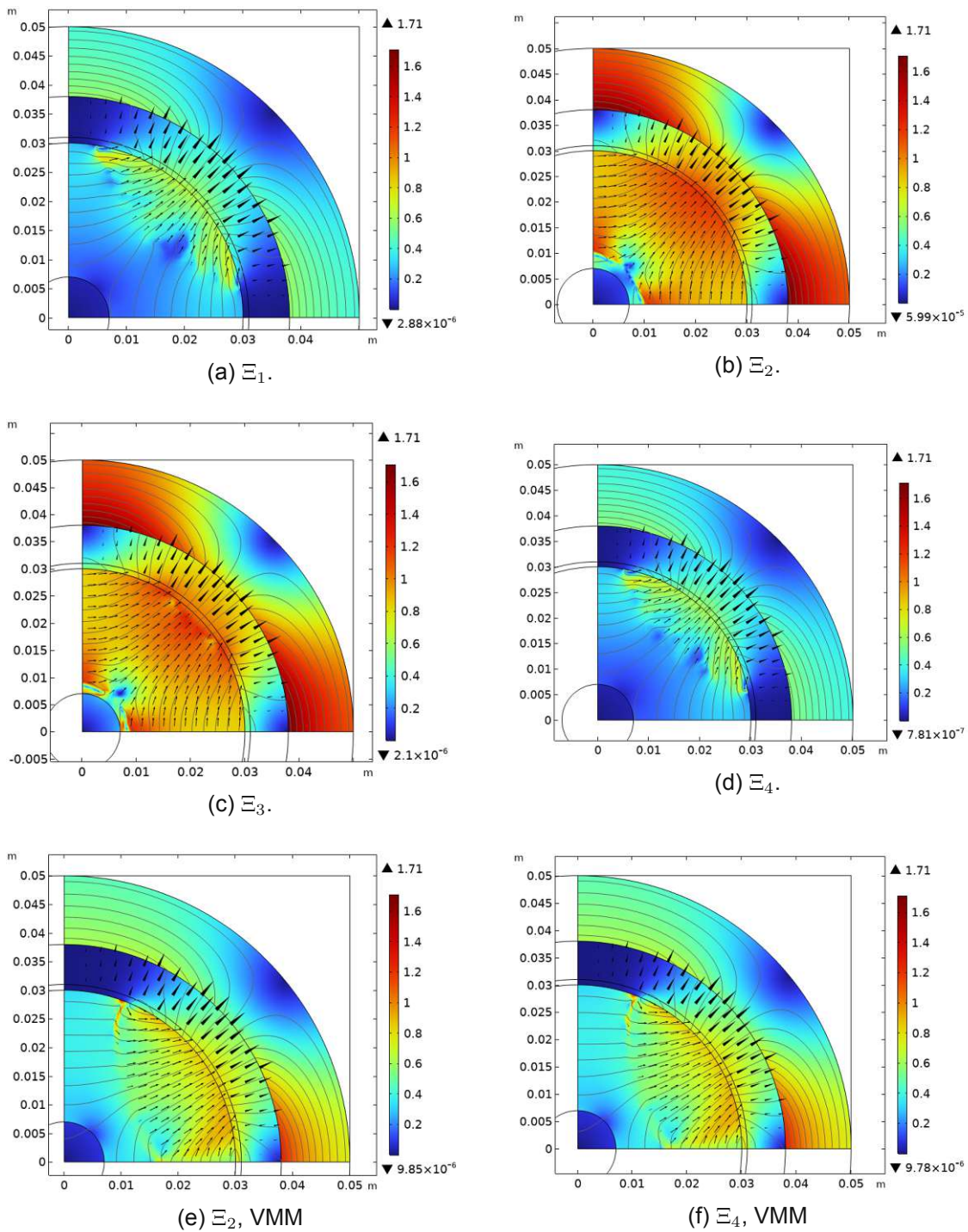


Figure 4.44: Simple Motor model analysed with Topology Optimization Method with a mesh refinement number of 1 and the combination with VMM. The colour bar serves as a demonstration of the norm of the magnetic field, given in Tesla. The black arrows represent the remanent flux density of the magnetic field in the design area R_m as they could not be illustrated in white because of visibility on the colour-bar. The cone-shaped arrows represent the desired field in region R_g . The projection point θ_β and initial value for the control variable θ_0 were set to 0.5 and used for all cases.

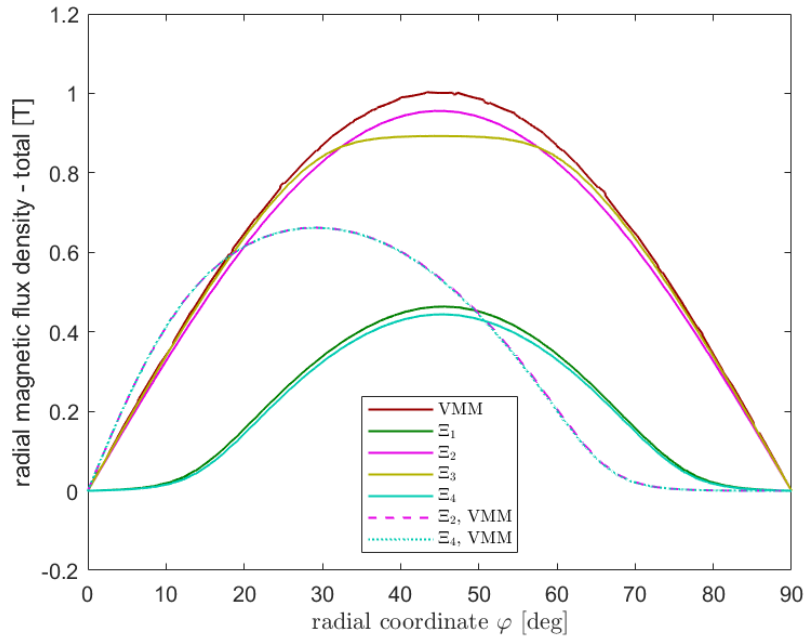


Figure 4.45: Total radial component of radial magnetic flux density - plots for the observed cases mentioned in table 4.9 for the mesh refinement number 1.

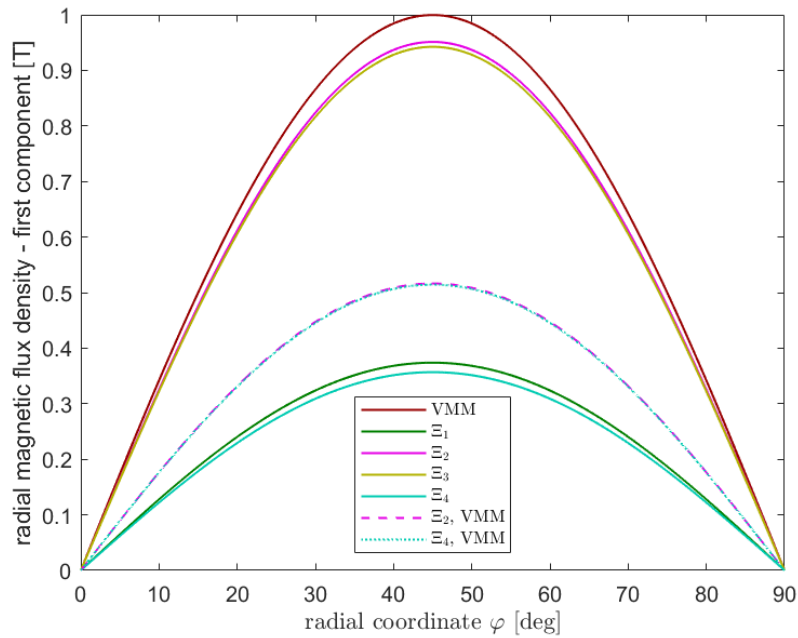


Figure 4.46: First harmonic of the radial component of radial magnetic flux density - plots for the observed cases mentioned in table 4.9 for the mesh refinement number 1.

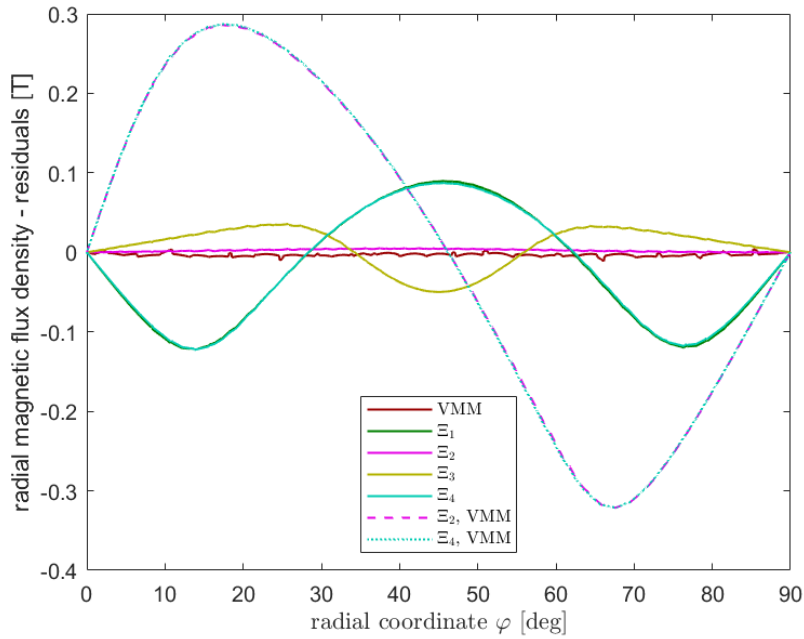


Figure 4.47: Residuals of the radial component of radial magnetic flux density - plots for the observed cases mentioned in table 4.9 for the mesh refinement number 1.

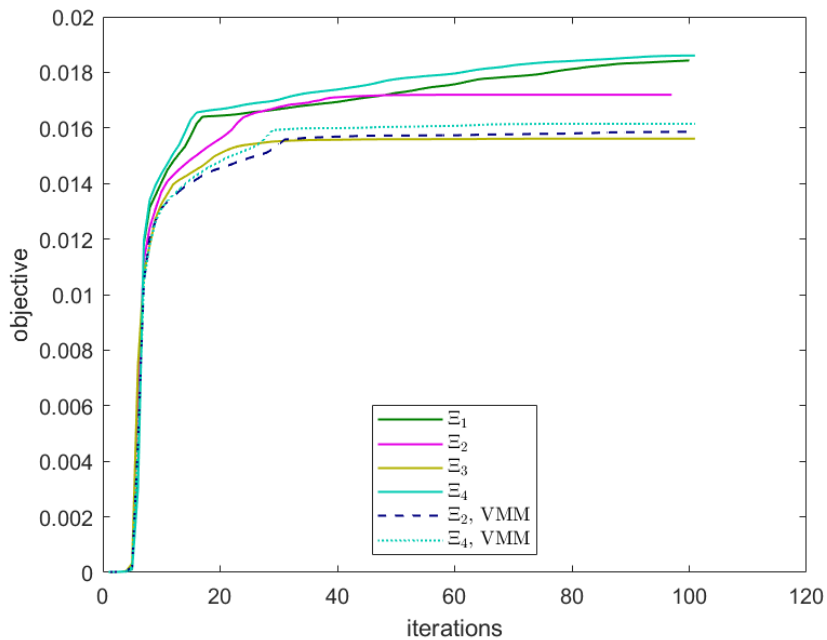


Figure 4.48: Objective plots for the observed cases mentioned in table 4.9 for the mesh refinement number 1.

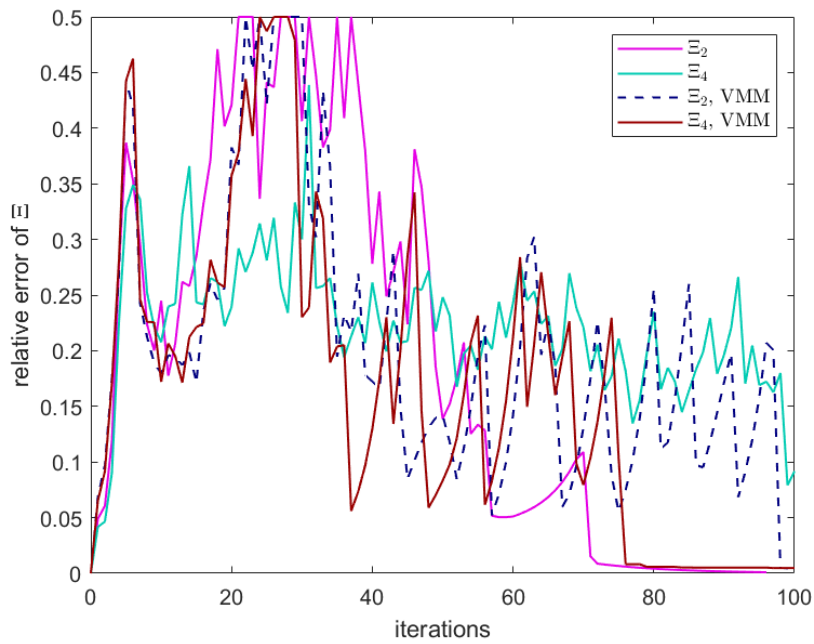


Figure 4.49: Relative error plots for the observed cases mentioned in table 4.9 for the mesh refinement number 1.

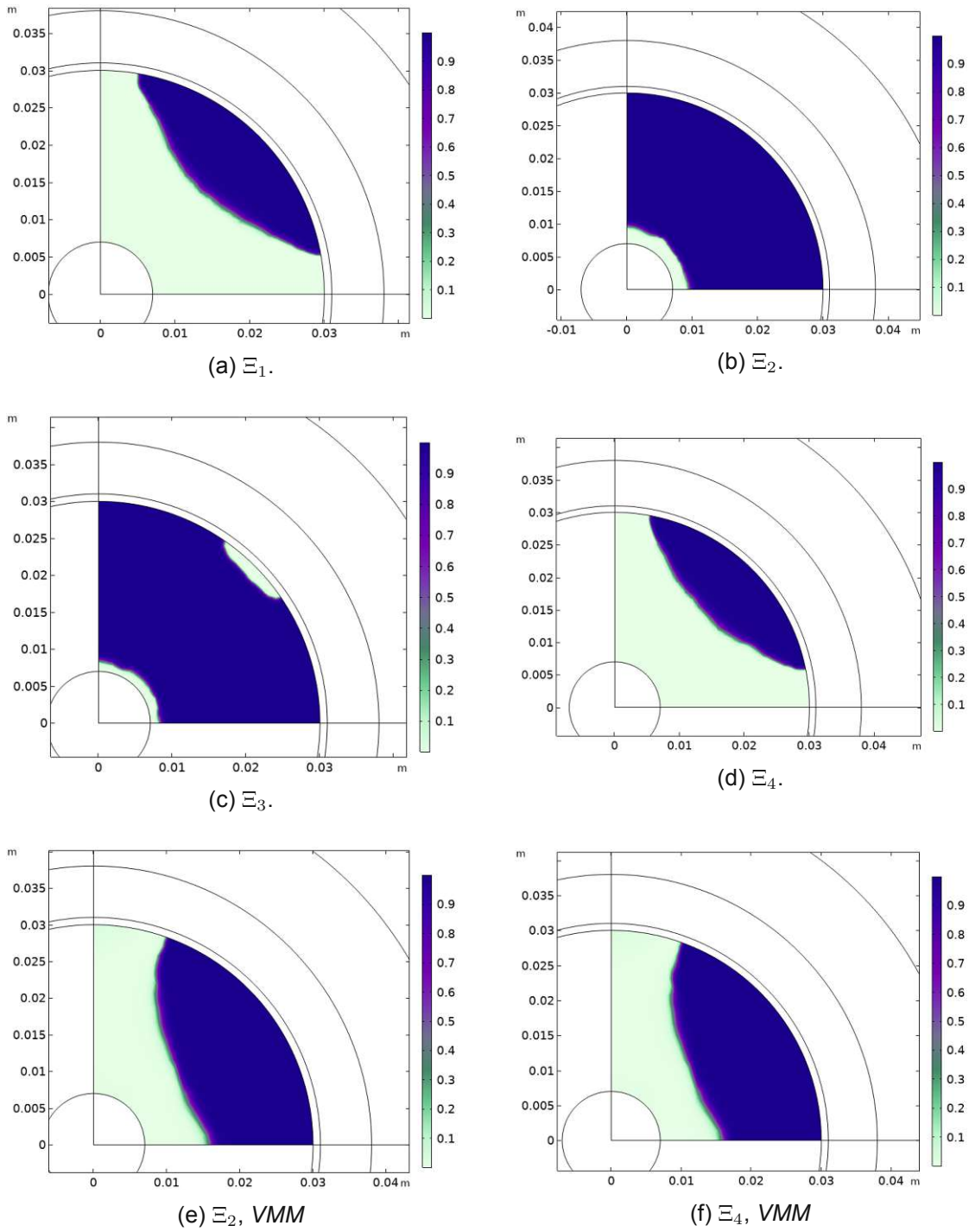


Figure 4.50: Simple Motor model analysed with Topology Optimization Method with a mesh refinement number of 1 and the combination with VMM. The colour bar serves as a demonstration of the magnet and iron area with the threshold of 0.5. The projection point θ_β and initial value for the control variable θ_0 were set to 0.5 and used for all cases.

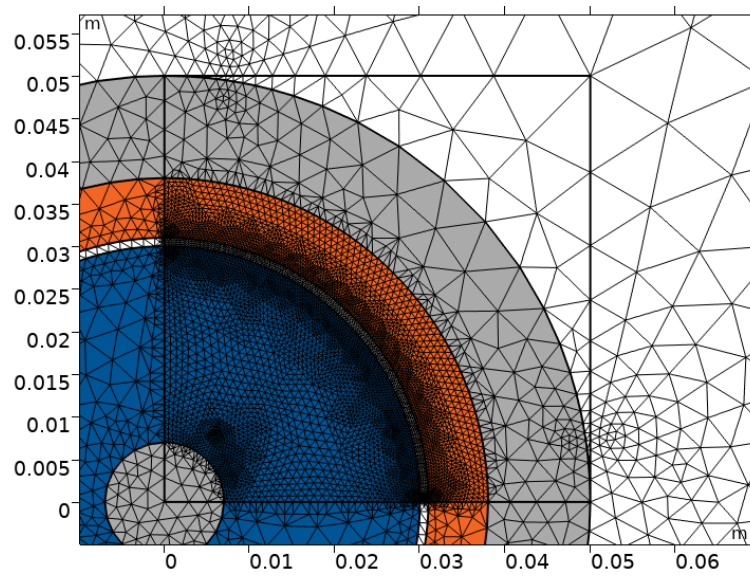


Figure 4.51: Mesh refinement number 2.

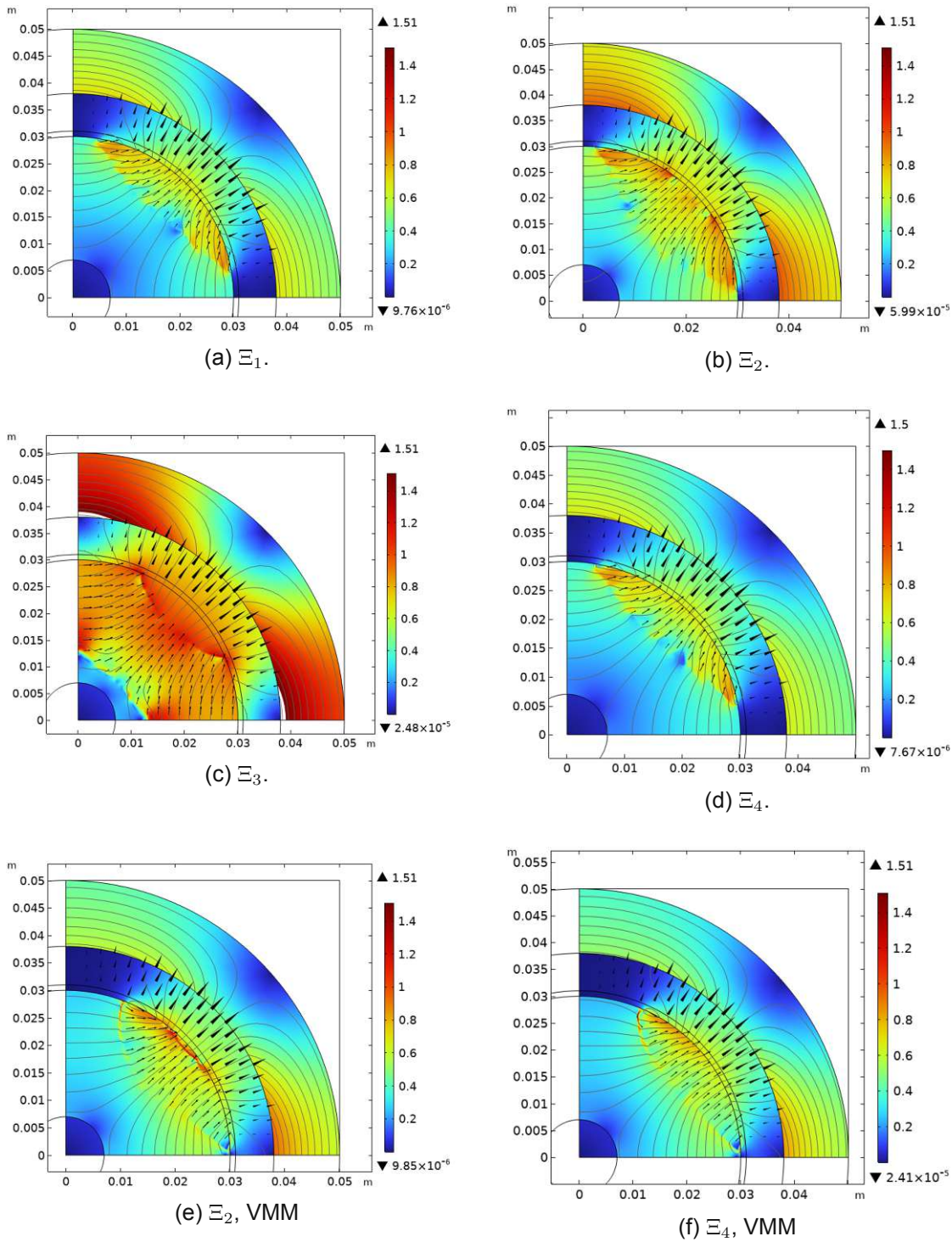


Figure 4.52: Simple Motor model analysed with Topology Optimization Method with a mesh refinement number of 2 and the combination with VMM. The colour bar serves as a demonstration of the norm of the magnetic field, given in Tesla. The black arrows represent the remanent flux density of the magnetic field in the design area R_m as they could not be illustrated in white because of visibility on the colour-bar. The cone-shaped arrows represent the desired field in region R_g . The projection point θ_β and initial value for the control variable θ_0 were set to 0.5 and used for all cases.

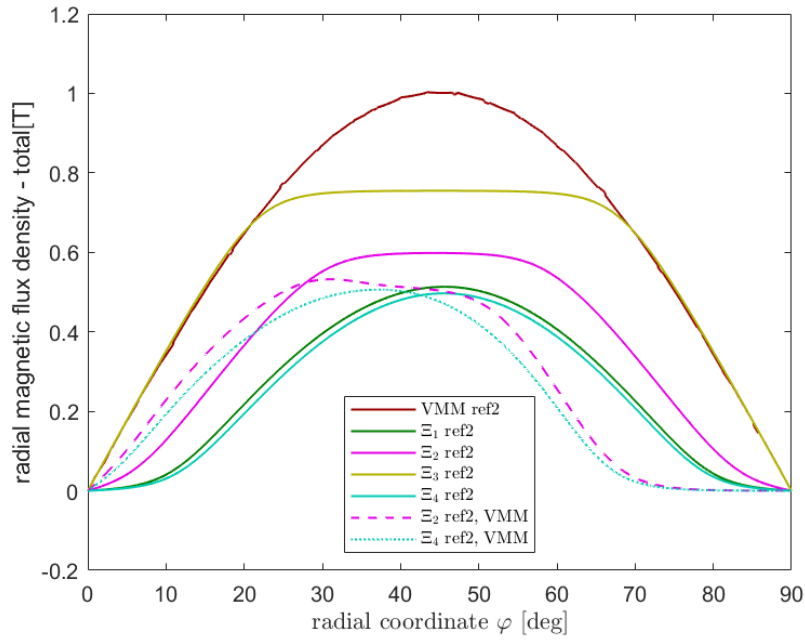


Figure 4.53: Total radial component of radial magnetic flux density - plots for the observed cases mentioned in table 4.10 for the mesh refinement number 2.

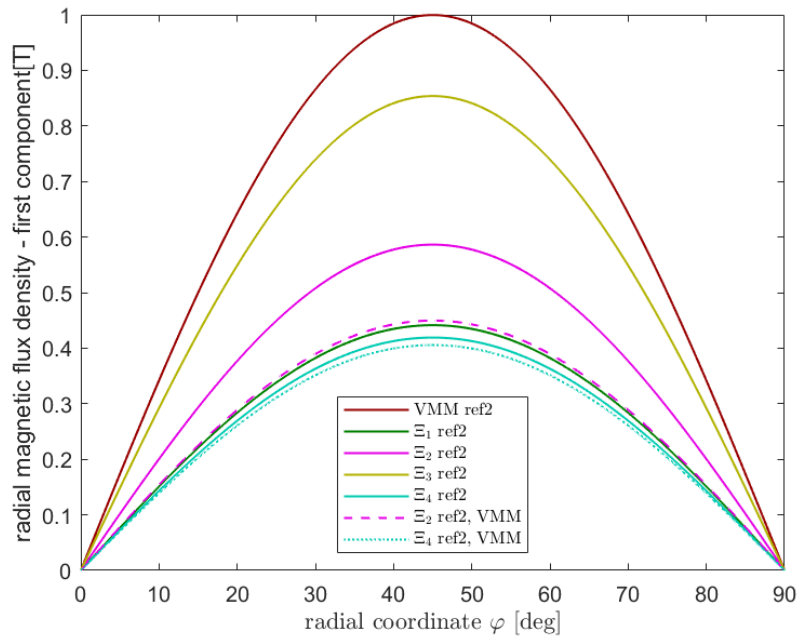


Figure 4.54: First harmonic of the radial component of radial magnetic flux density - plots for the observed cases mentioned in table 4.10 for the mesh refinement number 2.

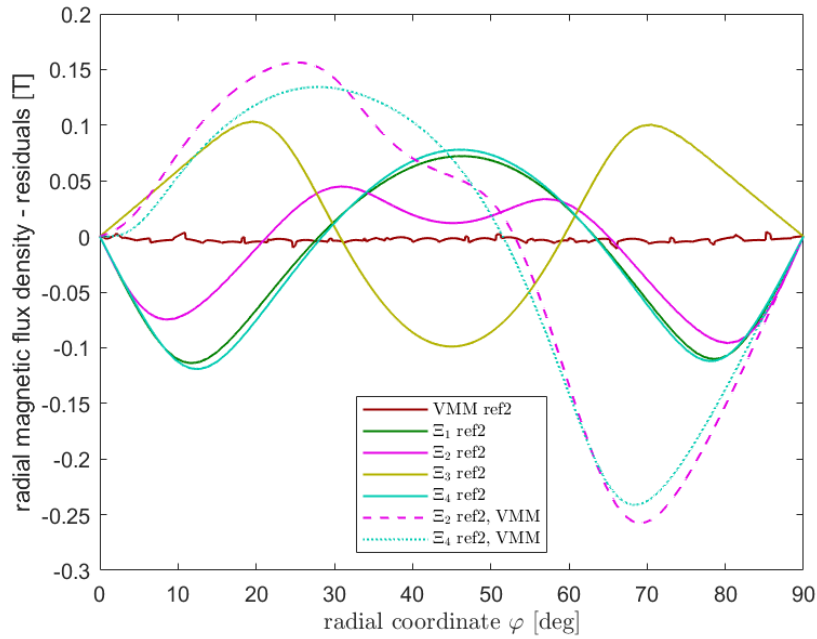


Figure 4.55: Residuals of the radial component of radial magnetic flux density - plots for the observed cases mentioned in table 4.10 for the mesh refinement number 2.

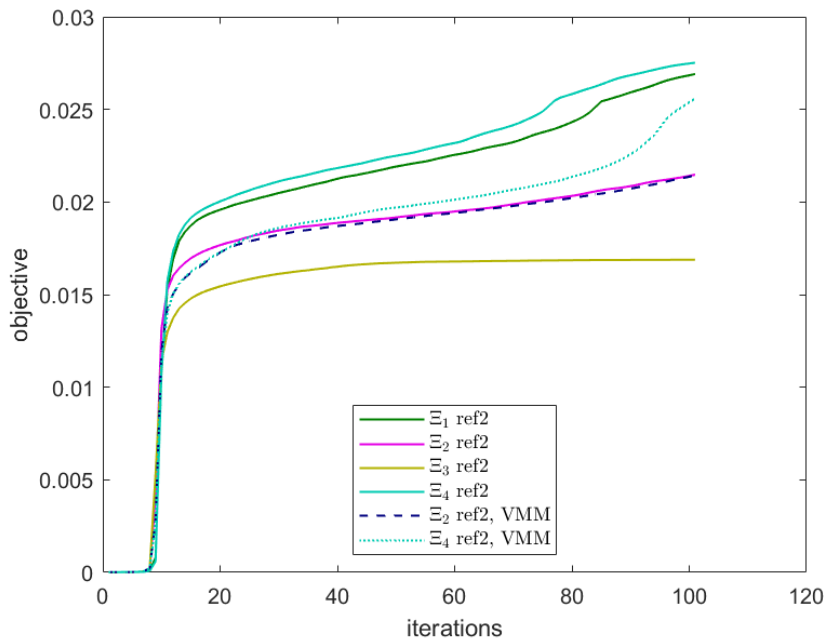


Figure 4.56: Objective plots for the observed cases mentioned in table 4.10 for the mesh refinement number 2.

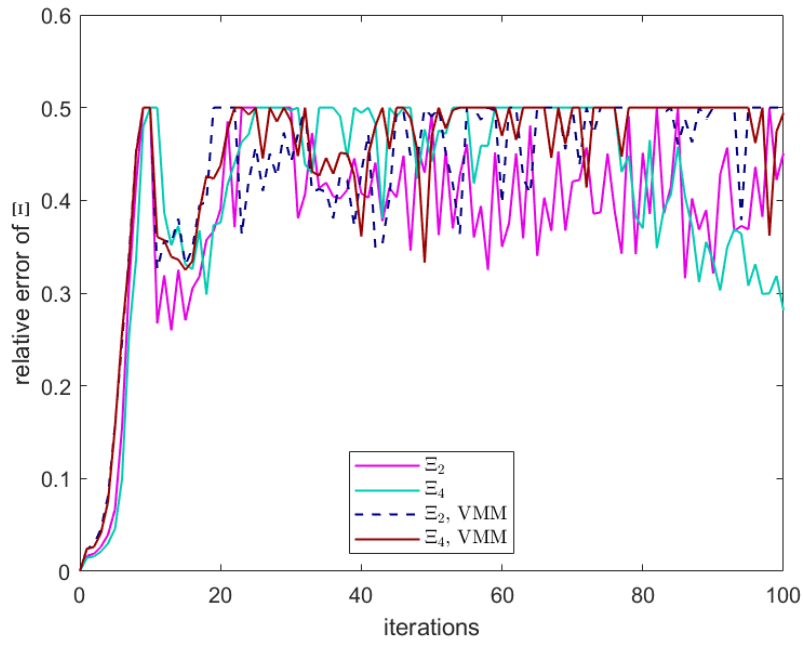


Figure 4.57: Relative error plots for the observed cases mentioned in table 4.10 for the mesh refinement number 2.

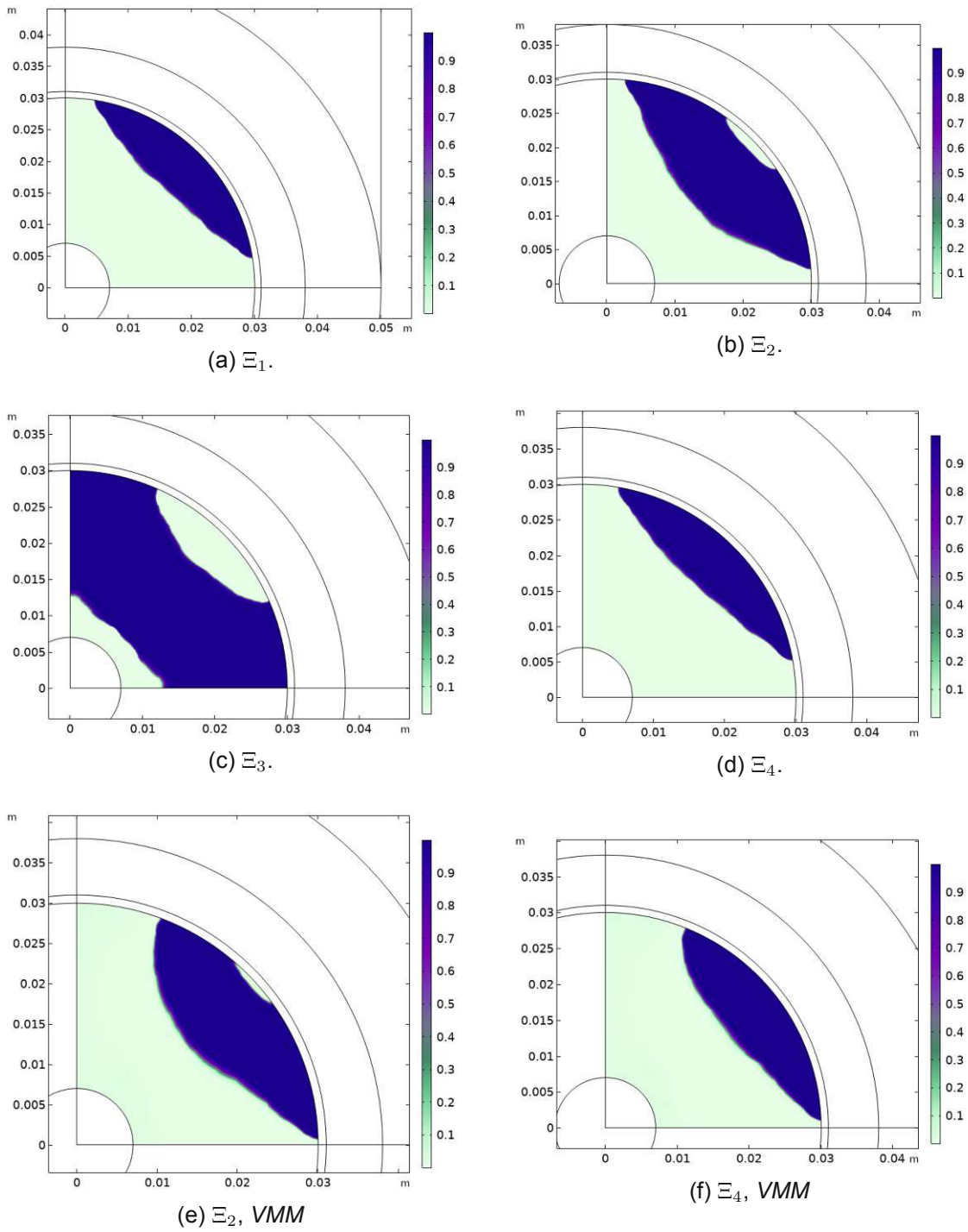


Figure 4.58: Simple Motor model analysed with Topology Optimization Method with a mesh refinement number of 1 and the combination with VMM. The colour bar serves as a demonstration of the magnet and iron area with the threshold of 0.5. The projection point θ_β and initial value for the control variable θ_0 were set to 0.5 and used for all cases.

5 Synchronous Machines

Synchronous machines are one part of AC machines, which are on the other hand part of electrical machines. Their range of application starts from small power motors, working in a range of Watt up to a few 100 Watt, working with a converter and permanent magnets, and used for ventilation of computers or within medical technology for example. Compared to DC motors they don't use brushes, which is of advantage [27].

As generators they can work in a range of some kW up to 2 GW for hydro power plants, wind power plants, as well as vehicle power supply of ships and airplanes [27].

Within the stationary state of energy conversion of an electrical machine, the electromagnetic torque that causes the rotation is mainly caused by the current within the armature winding which correlates with the electromagnetic field within the air gap. It is assumed that the spatial periodicity for circumference, given by the number of pairs of poles p , is the same for the wire configurations and the caused rotating fields. Therefore, it can be supposed to have the same behaviour of the machine in each pair of poles, why in this thesis at some points this symmetry will be used and only one pair of poles will be investigated [20].

A general equation with the angular speeds can be expressed in equation 5.4 and 5.5. Ω_{Sta} is referred to the angular speed of the electromagnetic field with respect to the stator inside the air gap, Ω_{Rot} defines the same, although with respect to the rotor. Equation 5.5 specifically defines the correlation for electrical angular frequencies, and p defines the number of pairs of poles. The general connection between the electric frequency f and the mechanical rotational speed n within electrical machines is given by equation 5.3 [20].

$$\Omega_e = p \cdot \Omega_{mech} = 2 \cdot \pi \cdot f \quad (5.1)$$

$$\Omega_{mech} = 2 \cdot \pi \cdot n \quad (5.2)$$

$$f = p \cdot n \quad (5.3)$$

$$\Omega_{Sta} = \Omega_{Rot} + \Omega_{mech} \quad (5.4)$$

$$\Omega_{e,Sta} = \Omega_{e,Rot} + p \cdot \Omega_{mech} \quad (5.5)$$

For synchronous machines, equation 5.6 and 5.8 are used. Former implies that the excitation of this machine type happens with time-independent parameters, e.g. permanent magnets in the rotor. Latter defines the relation between the frequency of the stator, for the first harmonic, and the rotational speed, therefore n_{Syn} is also called *synchronous rotational speed*, which explains the name for this type of electrical machines [20].

$$\Omega_{Sta} = \Omega_{mech} \quad (5.6)$$

$$\Omega_{Rot} = 0 \quad (5.7)$$

$$f_{Sta} = p \cdot n_{Syn} \quad (5.8)$$

Figure 5.1 provides a more specified overview of the various kinds of synchronous machines. They are subdivided by their excitation and if their axes need to be considered magnetically. The parameters l_d and l_q stand for specific inductance in direction d and q , which will be explained and shown in the following sub-chapters in more detail. For those types of machines, the dq coordinate system is common to use, with respect to a fixed rotor [20].

For the machine types which use excitation, such as the electrically excited and permanent magnet machines, as shown in figure 5.1 in light blue and lime, their longitudinal axes lies in the direction of the excitation [20].

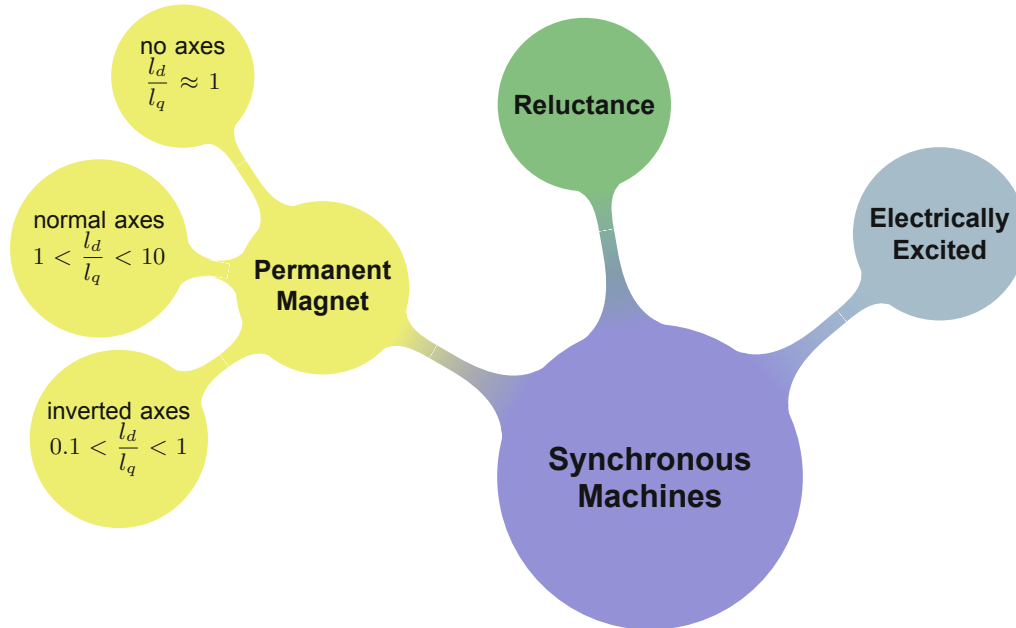


Figure 5.1: Overview over different types of synchronous machines and their relation between their inductance [20].

5.1 Permanent Magnet Synchronous Machines

5.1.1 Basic functionality of PMSMs (Permanent Magnet Synchronous Machines)

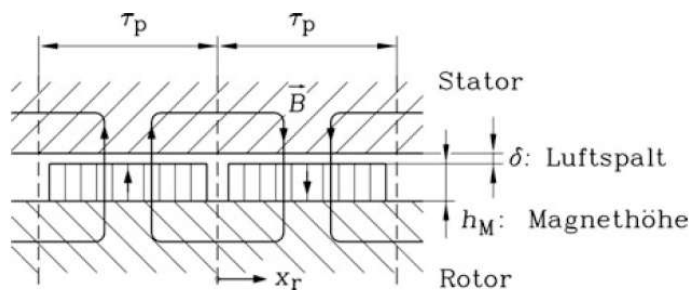


Figure 5.2: Magnetic circuit representing a simplified machine model [27].

This simplified explanation will be sufficient for this thesis as the machine will not be investigated by changing parameters like power rating, mechanical frequency. A more detailed description can be taken from e.g. [20].

Regarding an idle state of the machine, no current is flowing through the stator and only the influence of the rotor based permanent magnets (for this model here, surface-mounted magnets are used), is observed. Figure 5.2 shows the stator, rotor and in between the air gap δ (called "Luftspalt" in this figure), the height of the magnets h_M ("Magnethöhe"), the loops of the magnetic flux density B and the pole pitch τ_p . x_r stands for the coordinate x on the rotor side [27].

One of the loops of B closing over stator and rotor in figure 5.2 can be taken to define a curve integral, which results in a flux linkage of zero. Assuming infinitely permeable iron μ_r and neglecting leakage flux between the magnets of different polarity, then the integral can be written as, according to [27]:

$$\int_S \mathbf{H} ds = H_\delta \cdot \delta + H_M \cdot h_M = \theta = 0 \quad (5.9)$$

With assuming as well to have idealised continuity circumstances $B_M \cdot A_M = B_\delta \cdot A_\delta$ as neglecting leakage flux, the relation in equation 2.30 can be used to define a load line. With that, the dependency of the air gap height and magnets can be expressed.

Very typical for synchronous machines is to use the coordinate system dq , which is fixed regarding the rotor. It is used as the excitation, if not-existing it is the magnetically preferred axis, is laid in the real axes of the coordinate system. Therefore, it was used to define different rotor types for the PM synchronous machine in figure 5.1 and for describing one rotor type in figure 5.3 [20].

The direction d is important for the torque, as the dependency of the torque is mainly influenced for PMSMs through the flux linkage of the magnets in the d direction in the idle state [20].

5.1.2 Stator configurations

The focus for this thesis here lies on the type called FSCW (fractional-slot concentrated wound) double layer stator, as this one is used within COMSOL Multiphysics as a predefined example and serves here for more investigations. As mentioned in [49], the main machine parameters for the permanent magnet synchronous machines within the dq coordinate system can be defined by both flux linkages of the permanent magnets as well as the mutual and self inductances. Former represents the interaction between the magnetomotive force (MMF) from the stator as a result from the equivalent air gap function. Second refers to the interaction between the MMF of the stator resulting from the flux density caused by permanent magnets.

The FSCW types, as explained in [49], show no crossing of the windings, hence the copper use is less, which results in a lower copper loss factor as well and in total a more compact design is possible.

5.1.3 Rotor configurations

The main three types of rotors of synchronous machines can be defined as followed: the surface-mounted magnet rotors, the interior-mounted magnet rotors and interior-mounted magnet rotors using inverted axis. The first type has the advantage of an easy fixation of the magnets, although the air gap which counts magnetically is, compared to the other types, quite high, as the height of the magnets add up to the needed air gap between rotor and stator. This does not happen for the other two types, as the magnets are mounted inside the rotor. For the surface-mounted type then it needs to be mentioned that they are mostly not short-circuit-proof and are used for small rotational speed [20].

The second type includes rotors which have interior-mounted magnets, which often include small air areas inside for magnetic flux guidance reasons. As now the magnets are stored inside the rotor, the air gap is within the norm height, which means that short-circuit-strength is given as well as less eddy-current losses inside the magnets, compared to the first application with magnets placed on the surface of the rotor. The main difference between the last two types of permanent magnet rotors occurs in the magnetic axes, as the magnetic flux component in direction d needs to pass through the magnet for the inverted type, whereas for the normal axes type, the d flux can go through the iron core directly. The same inverse principle counts for the q axes [20].

Especially rotor types using permanent magnets for excitation not often use damping windings, as they often connected to converters and they can replace them by an extra control mechanism. Although, when they are connected directly to the grid, as for generators for wind mills, then this type of rotor only exists as interior-mounted magnets where the extra damping windings can be plugged in, as can be seen in [50]. For the surface-mounted type then the occurring eddy-currents behave similarly like damping windings [20].

Although the better mechanical stability and reliable performance of the interior-mounted type of rotor is more preferred for several applications, the focus will lay on the embedded surface mounted permanent magnet rotor type as of simplicity and time for realisation of this model, as pictured in figure 5.3. Further types of permanent magnet rotor configurations are explained in [49].

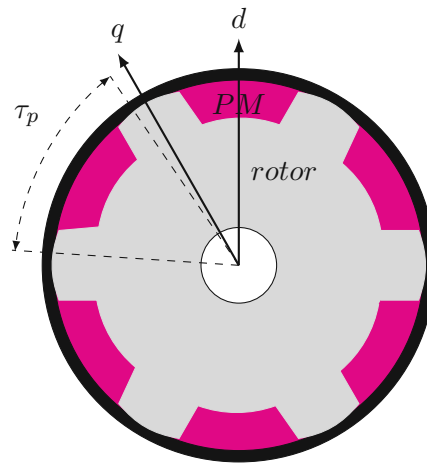


Figure 5.3: Model for 6 pole embedded permanent magnet rotor with axes d, q [49],[20].

5.2 Embedded Surface Mounted Permanent Magnet Synchronous Machines with COMSOL

5.2.1 Rotor optimization

First, a simplified model of the motor was generated in COMSOL to apply both methods in order to generate a functional rotor to implement in the predefined COMSOL motor model. Therefore, the geometry in figure 5.4 was designed for four different cases, but all with the same geometry of table 5.1.

The focus laid on generating an exportable curve to define the boundary between magnet and iron parts, as well as a magnetization, through applying both methods like in the previous chapter. With these two parameters, and making use of symmetrical installation, a rotor was constructed and compared with the results of the existing COMSOL example.

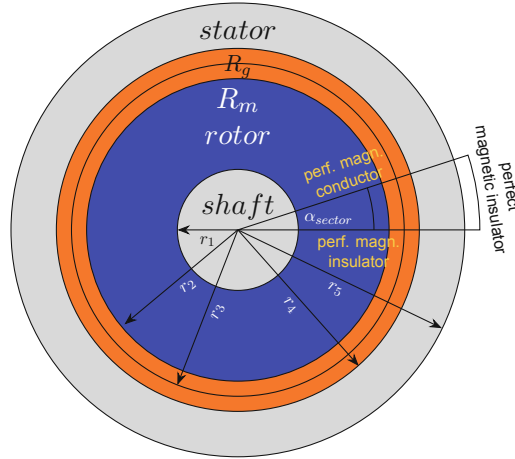


Figure 5.4: Schematic figure for PM rotor optimization.

PM rotor model - Geometry Configuration	value	unit
r_1	0.0005	m
r_2	0.015	m
r_3	0.01525	m
r_4	0.0155	m
r_5	0.0165	m
α_{sector}	18	°

Table 5.1: Chosen measurements for rotor design.

The measurements were chosen to be suitable to insert into the COMSOL 2D permanent magnet motor model. The idea of taking one sector for the combined approach was given by [46], as it can be applied as well on a symmetric composition as it is given here.

$$\Xi_1 = \frac{\langle \hat{B}_{slot} \rangle \cdot \sin(5 \cdot \text{atan2}(y, x))}{2 + A_{mag}} \quad (5.10a)$$

$$\Xi_2 = \frac{\langle \hat{B}_{slot} \rangle \cdot \sin(5 \cdot \text{atan2}(y, x))}{0.5 + A_{mag}} \quad (5.10b)$$

$$\Xi_3 = \frac{\langle \hat{B}_{slot} \rangle \cdot \sin(5 \cdot \text{atan2}(y, x))}{10^{-3} + A_{mag}} \quad (5.10c)$$

$$\Xi_4 = \frac{\langle \hat{B}_{slot} \rangle \cdot \sin(5 \cdot \text{atan2}(y, x))}{1 + A_{mag}} \quad (5.10d)$$

The idea of setting the objectives like shown in equation 5.10a-5.10d was to regulate the magnitude of the magnet area by changing the parameter added in the denominator, while maximizing a harmonic sinusoidal field in the air gap between rotor and stator. Equation 4.23 was used again to define the material.

For the expression of the remanence flux density, the norm includes, as previous examples had, θ_p and $B_{rem} = 1.4$ T, for the direction the corresponding expressions of equation 5.12 are used.

$$\mathbf{B}_r = \theta_p \cdot B_{rem} \cdot (\mathbf{e}_{B_{g,x}} + \mathbf{e}_{B_{g,y}}) \quad (5.11)$$

The desired B_g field within the area R_g is set to:

$$\mathbf{B}_g = \sin(5 \cdot \text{atan2}(y, x)) \cdot \frac{x}{\sqrt{x^2 + y^2}} \hat{e}_x + \sin(5 \cdot \text{atan2}(y, x)) \cdot \frac{y}{\sqrt{x^2 + y^2}} \cdot \hat{e}_y \quad (5.12)$$

For the plots shown in figures 5.5a-5.5d, a mesh refinement number of 2 was used except for the shaft inside. For all the plots, the optimality tolerance of 0.001 was used and the boundary conditions, shown in figure 5.4 were applied. For those cases, the objective plots were plotted, as well as the relative error plots, similar to the analysis of chapter 4. The relative error was split into two graphs for better visibility. Plot 5.7 shows clearly a minor relative error for objective 1 than for objective 2, although in the objective plot 5.6 objective 2 achieves a higher outcome. For the second relative error plot 5.8 objective 3 achieves a lower error and higher objective outcome than objective 4, even though the iteration for the pink objective stopped 50 iterations before the turquoise one.

However, it is important to see these results in relation to their field plot, and later included in the motor model to evaluate their performance better. Figure 5.5 shows the sector plot for all the observed cases, plotted with the same colour range for better comparison. Especially objective 3 shows, despite good results from the plots mentioned in the former paragraph, a weak field and very small contour line for the supposed magnet area. This affects clearly the functionality within the motor model, as shown in the following results.

5.2.2 Complete motor implementation and analysis

For this investigation, the permanent magnet motor model of COMSOL was taken, which should represent a 2D version of a real life motor with 35mm diameter and an axial length of 80mm [51],[52]. Detailed description of it can be seen in table 5.2 and figure 5.9.

PM 2D motor model - Geometry	definition	value	unit
α_0	initial mechanical angle	20	°
$2p$	number of poles	10	1
p	number of pole pairs	5	1
m	number of phases	3	1
ω_{rot}	rotational speed	600	rpm
f_{el}	electrical frequency	50	Hz
I_0	peak current	10	A
N_{turn}	number of wire turns in slot	20	1
f_{fslot}	slot filling factor	0.8	1
Q	number of stator slot	12	1
δ	air gap length	5	mm
$d_{cont} = 2 \cdot r_4$	diameter of rotor-stator continuity interface	30.5	mm
d_{stator}	stator diameter	50	mm
d_{geom}	motor diameter incl. air external to stator	53	mm
$tooth_h$	tooth height	8	mm
$tooth_w$	tooth width	4	mm
$shoe_h$	shoe height	1.5	mm
$shoe_w$	shoe width	6	mm
$shoe_f$	radius of shoe fillet	0.4	mm

Table 5.2: Measurements for COMSOL geometry of the motor model [52].

According to table 5.2, the number of stator slots per pole and phase is

$$q = \frac{Q}{2 \cdot p \cdot m} = \frac{2}{5} \quad (5.13)$$

Based on the structure of q , which indicates the fractional slot winding type of the stator, its denominator is used to identify the occurring harmonics ν_{PM} within this machine type. According to [20], it can be calculated, with respect to $g \in \mathbb{Z}$ as follows:

$$\nu_{PM} = \frac{1}{5} \cdot (1 + 2 \cdot m \cdot g) = \frac{1}{5}; -1; \frac{7}{5}; -\frac{11}{5}; \dots \quad (5.14)$$

It is important to mention as those harmonics, especially the first one with the norm smaller than one runs faster than the first harmonic, which can cause severe acoustic noise for this type of machine. The other harmonics are slower than the first harmonic, but can be remarkable as torque ripple [20]. Therefore, with the discrete fourier transformation (DFT), the harmonics of the investigated air gap flux density and the torque was analysed as well.

The model used from COMSOL can be seen in figure 5.9 with its partitions and materials. The three phases are highlighted with different colours, as well as soft iron and iron regions. In this image, the slot winding type, defined as "radial partition" in COMSOL, can be seen more clearly [51].

For a general demonstration, a surface-mounted permanent magnet rotor is pictured there, although for the investigations, an embedded model was used, to compare it with the designed rotor results.

The various material areas are highlighted in different colors in figure 5.11a to make them easier to spot and provide a better overview.

Copper for the windings is presented in dark orange in figure 5.11a, *N54 (sintered NdFeB)* for the magnets with a remanence flux density of 1.45T and a recoil permeability of 1.05 is highlighted in magenta. Soft iron was implemented for rotor and stator parts, held in dark gray, as plotted in the BH curve in 5.10. Iron, in light grey, was used for the shaft. The areas filled with air are painted in light blue.

As explained in chapter 2.2.2 with equation 2.30, with a larger air gap δ between rotor and stator, smaller air gap flux density would occur, as well as more likely that demagnetization effects occur. Therefore, the air gap was not changed and tried to be adapted to the original model. Therefore, a stronger dependency of the magnet height can be seen at the plots of the air gap flux density.

After implementing the contour plot and the magnetisation of each rotor solution, it was adapted to generate a new rotor to the existing stator configuration. Figure 5.11 gives an overview over the different magnet shapes, coloured in magenta to differentiate them easier.

Figure 5.11d includes small rectangular shaped cavities in between the magnet shapes. These were added after analyzing the magnet shapes, as the field lines partly closed through soft iron and did not fulfill their purpose for the machine. The idea, especially of rounding the cavity edges, was partly inspired by [53], the measurements for the small rectangles are 2.8mm for the height and 3.7mm for the width.

As mentioned before, in figure 5.12 and 5.13, a clear difference in the magnetic field density norm (colour bar) is remarkable for objective 3, whereas objective 1 and 4 seem

to have similar outputs.

The torque calculation for this example is based on *Arkkio's method*, which is referred to the Maxwell's stress tensor for the general torque calculation, mentioned in chapter 2.1.2. It is specifically used when two parts are split through an air gap with one rotating part, demonstrated in figure 5.14. The main difference between this method and the calculation with Maxwell's stress tensor lies in the integral, as latter in equation 2.20b uses a surface integral, whereas Arkkio's method uses a volume integral as shown in equation 5.15a, which leads to less mesh dependency [54]. For the volume integral over the area Λ (eq. 5.15c) utilizes the azimuthal force density, which is calculated through the radial and azimuthal component of the flux density, as shown in 5.15b [54].

$$T = n_{sec} \int_{\Lambda} \frac{F_{\varphi} \cdot r_A}{r_{out} - r_{in}} dV \quad (5.15a)$$

$$F_{\varphi} = \frac{B_r \cdot B_{\varphi}}{\mu_0} \quad (5.15b)$$

$$\Lambda : (r_{in} < r_A < r_{out}) \quad (5.15c)$$

The radius r_A lies between two radii which are entirely in air and n_{sec} is the number of sectors, set automatically by COMSOL. The area used for Arkkio's method is highlighted in blue in figure 5.14a and more detailed in figure 5.14b, adjacent to the continuity boundary.

The continuity boundary is the boundary that is defined as the rotors mesh is rotating, so it needs to be adapted during rotation to the mesh of the stator to have a continuity between the two parts. Therefore, variables can be properly interpolated if the meshes are not continuous to guarantee that the magnetic vector potential A is continuous [52].

The plotted torque in figure 5.15 serves as an easier comparison of the resulting torque between the different rotor solutions. It is plotted over exactly 72° , which refers to exactly the length of one pole pair for this machine type.

This measurement was taken over 360° to calculate a better approximation of the RMS (root mean square) of the torque, that is plotted over the magnet area of the rotor magnets, shown through figure 5.18.

It is important to have in mind that aside of the clear improvement of the torque in its magnitude with objective 1 and 4, and magnet material could be reduced with objective 2, a ripple in the torque occurs, as the plot over one electrical period in figure 5.17 shows, but more clearly demonstrated through the calculated DFT (discrete fourier transformation) of the torque ripple in figure 5.19. The latter shows for each plot the original model with blue diamond-shaped symbols in comparison with one of the rotor models and their objectives what they are based on.

Clearly for the motors designed with objective 1,2 and 4 harmonics in the torque can be seen, compared to the dark blue plot.

In a similar way like the torque investigation, a closer look can be done towards the magnetic flux density within the air gap, illustrated over one half of the arc length, plotted over the angle in $^\circ$, in figure 5.16. A similar shape can be registered, as well as the exceeding amplitude of all rotors except the one designed with objective 3, which is obvious when taking into account the minimized magnet size. To interpret this result from another perspective, again the DFT was used to calculate the occurring harmonics in the flux density,

shown in figure 5.20. As already seen in figure 5.16, the similar curve of rotor with objective 2 mirrors in the green harmonic plot compared to the original model, as the first component is the strongest for green as well.

On the other hand, the rotor with the objective 1 shows a stronger component than the first one, which might come through in more sharp peaks in 5.16.

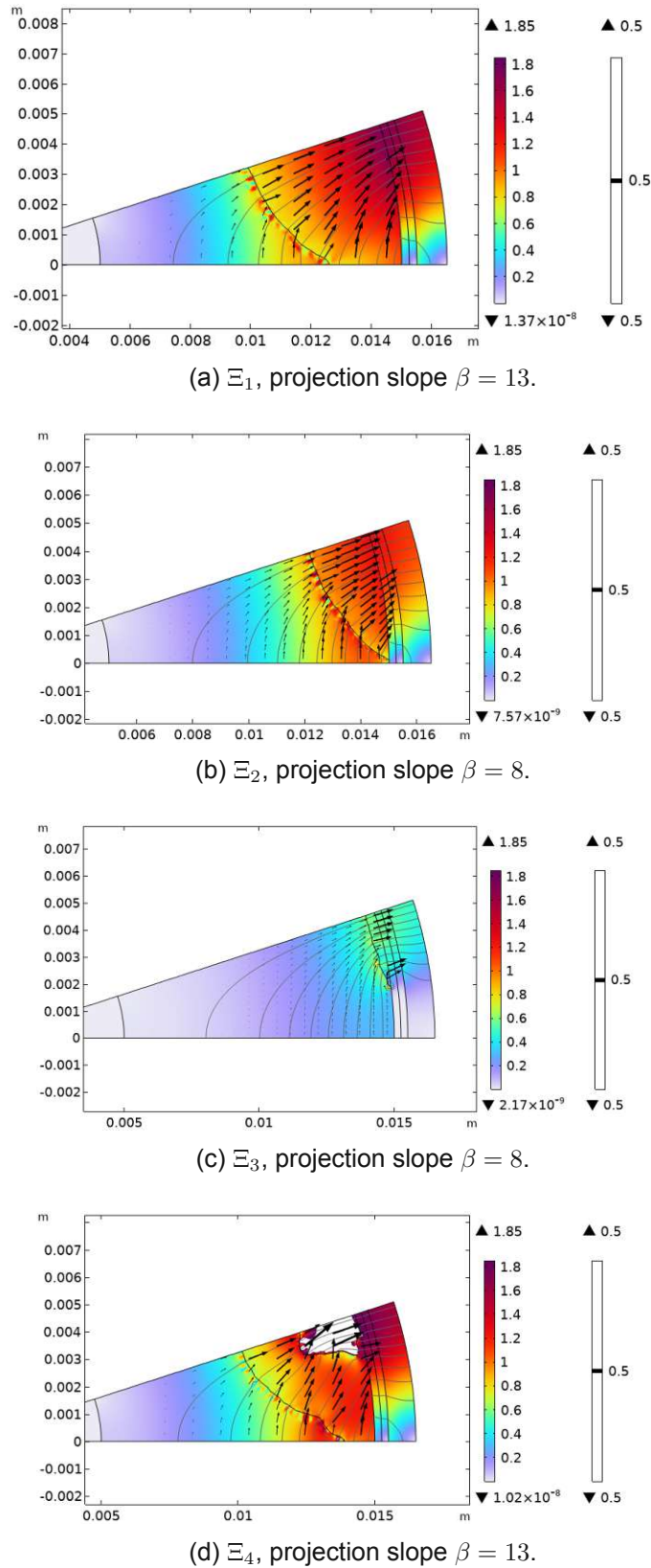


Figure 5.5: Sector plots of all observed cases for the rotor model. The black arrows this time show the magnetization that resulted from the Virtual Magnet Method. The contour line signifies the boundary between iron and magnet area.

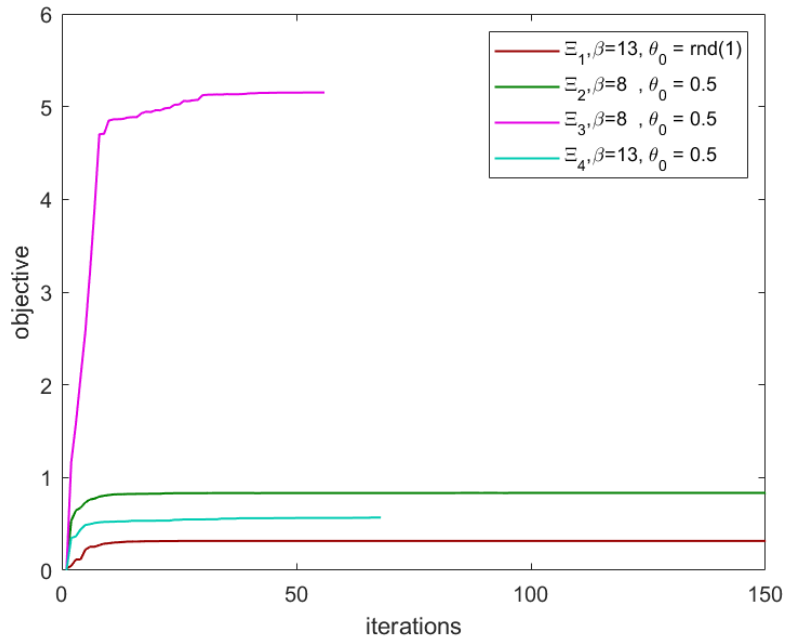


Figure 5.6: Objectives of designed rotor models, plotted over iterations.

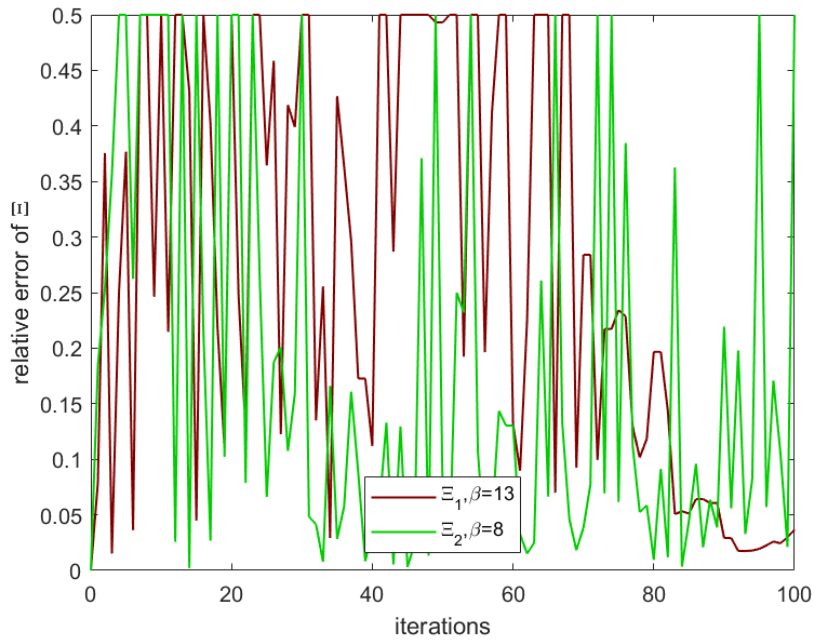


Figure 5.7: Relative error plots of objective 1 and 2, for better visibility it was plotted separately from the other two error plots.

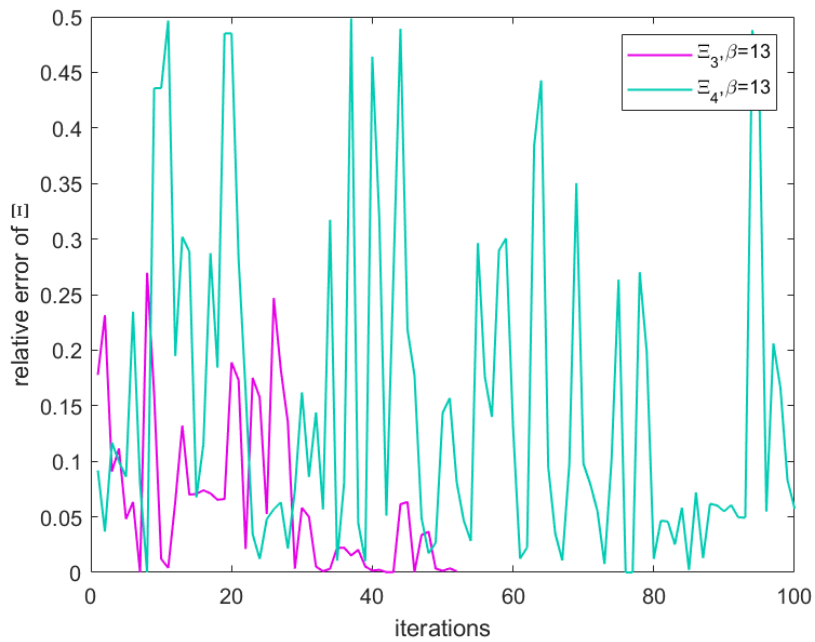


Figure 5.8: Relative error plots of objective 3 and 4, for better visibility it was plotted separately from the other two error plots.

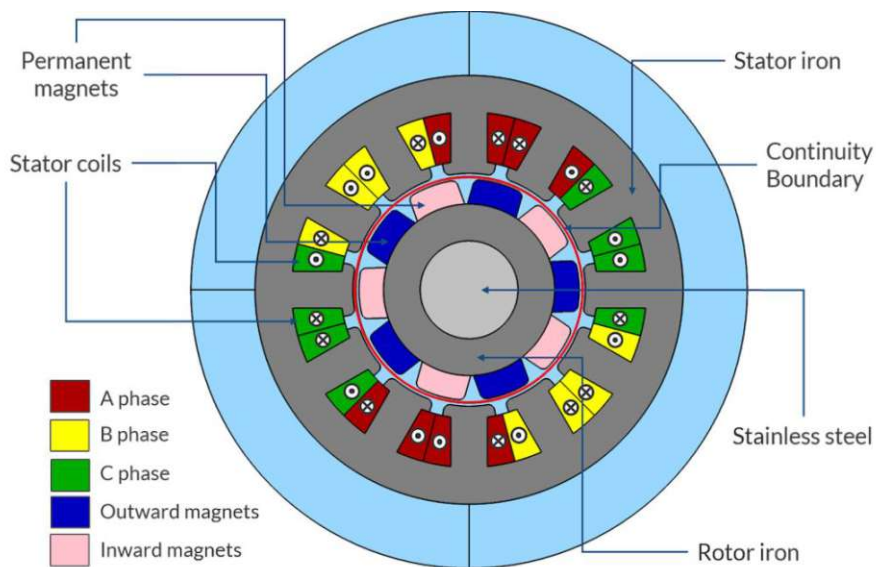


Figure 5.9: 2D - permanent magnet motor model in COMSOL, taken from [51].

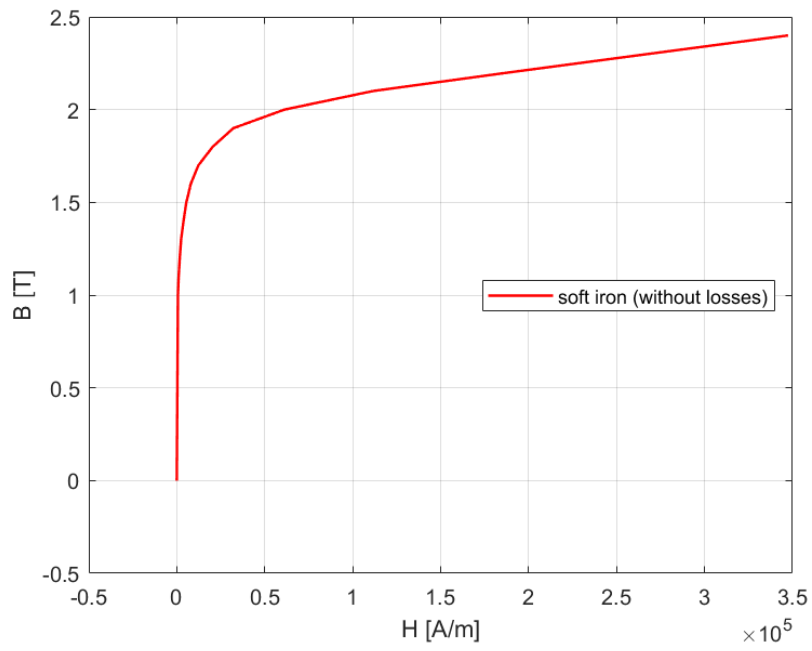
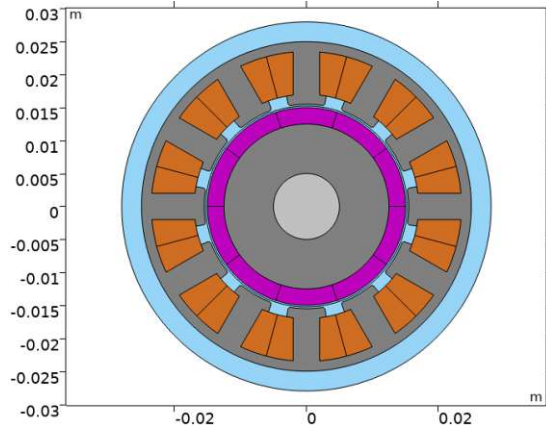
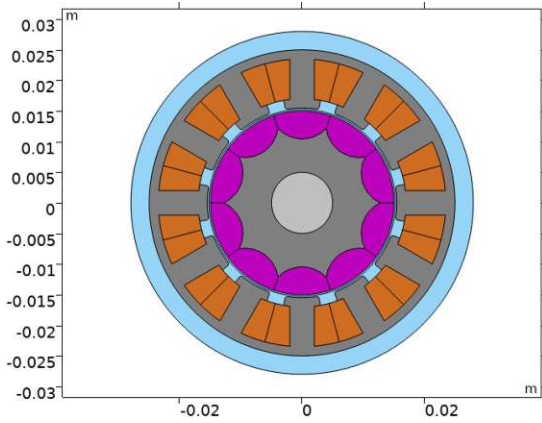


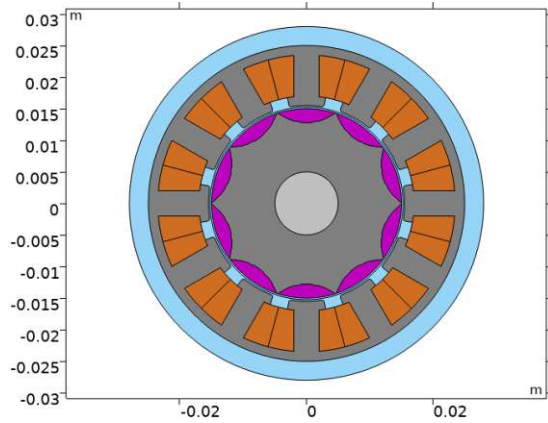
Figure 5.10: BH curve for the soft iron used in the COMSOL model.



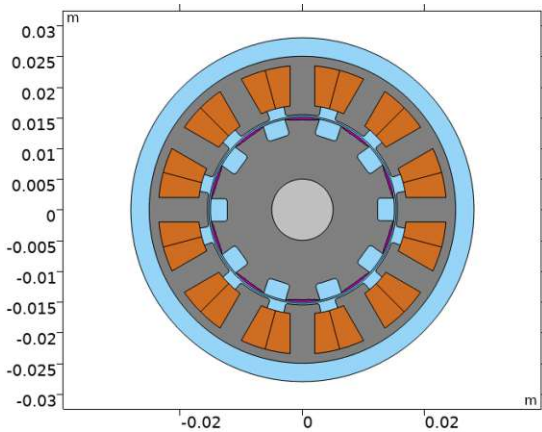
(a) Original model of COMSOL



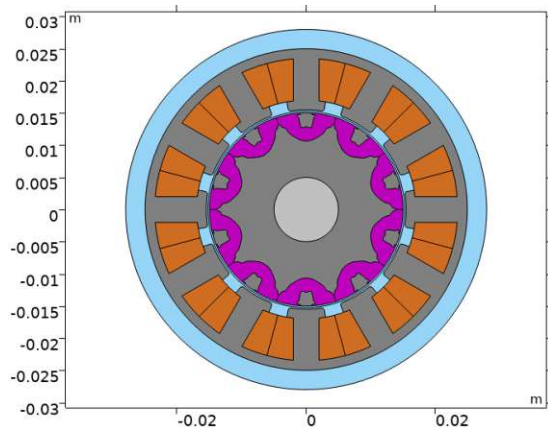
(b) Motor with included solution of $\beta = 13, \Xi_1$.



(c) Motor with included solution of $\beta = 8, \Xi_2$.

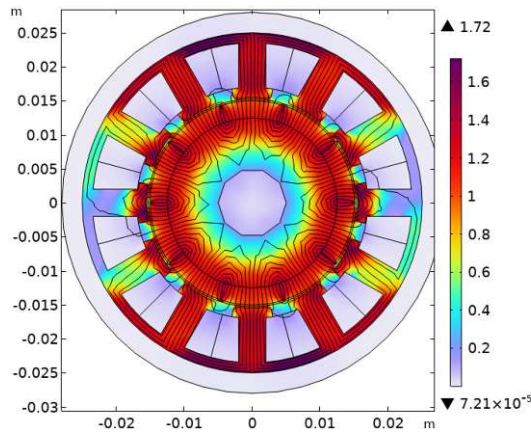


(d) Motor with included solution of $\beta = 8, \Xi_3$.

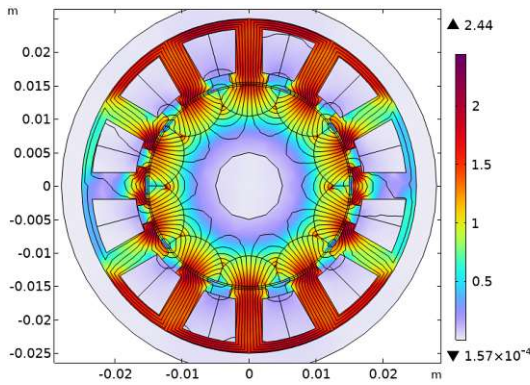


(e) Motor with included solution of $\beta = 13, \Xi_4$.

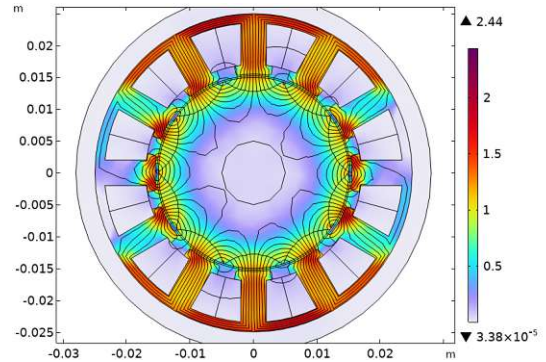
Figure 5.11: Comparing magnet shape (in magenta) within designed rotor , implemented in the motor model, with original model.



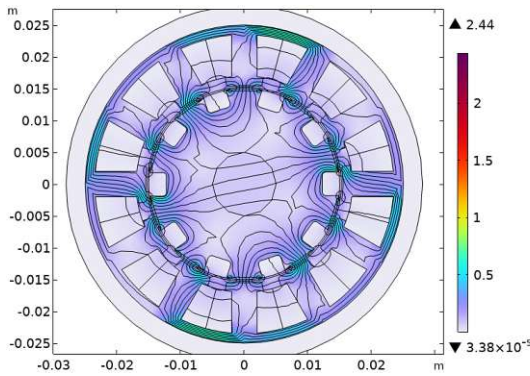
(a) Original model of COMSOL



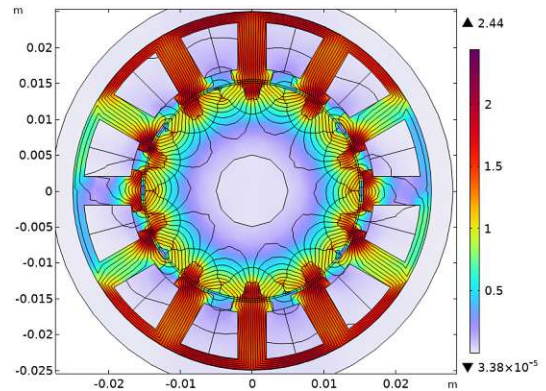
(b) Motor with included solution of $\beta = 13, \Xi_1$.



(c) Motor with included solution of $\beta = 8, \Xi_2$.

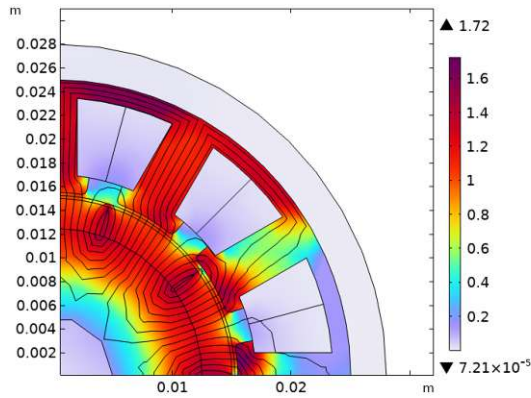


(d) Motor with included solution of $\beta = 8, \Xi_3$.

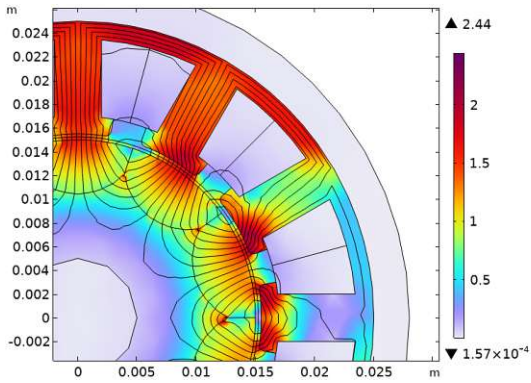


(e) Motor with included solution of $\beta = 13, \Xi_4$.

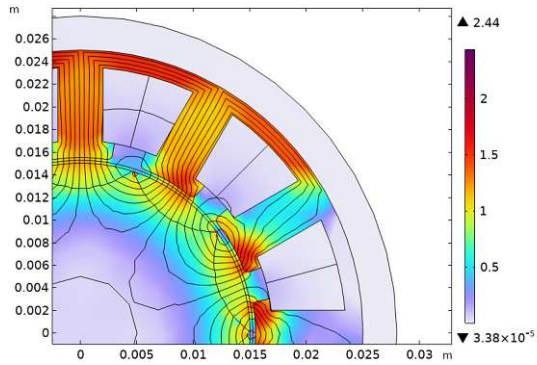
Figure 5.12: Comparing field plots of stationary analysis of original model with imported rotor models, at $t = 0$.



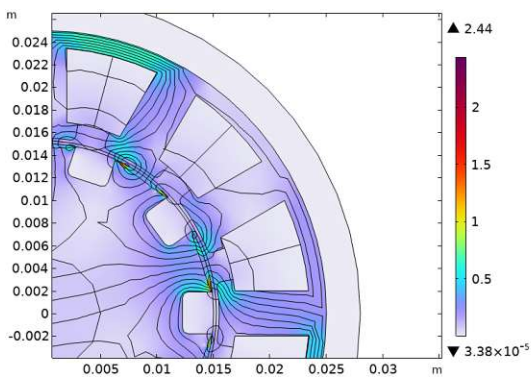
(a) Original model of COMSOL



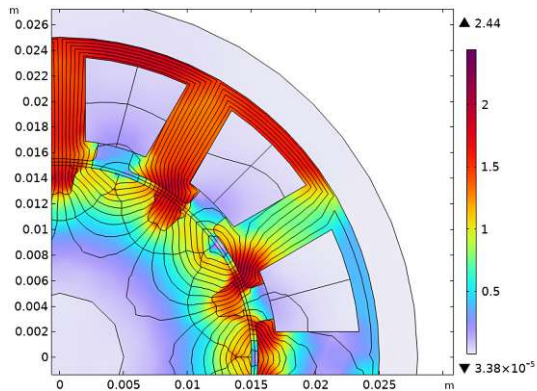
(b) Motor with included solution of $\beta = 13, \Xi_1$.



(c) Motor with included solution of $\beta = 8, \Xi_2$.



(d) Motor with included solution of $\beta = 8, \Xi_3$.



(e) Motor with included solution of $\beta = 13, \Xi_4$.

Figure 5.13: Comparing field plots of stationary analysis of original model with imported rotor models by more detailed plot, at $t = 0$.

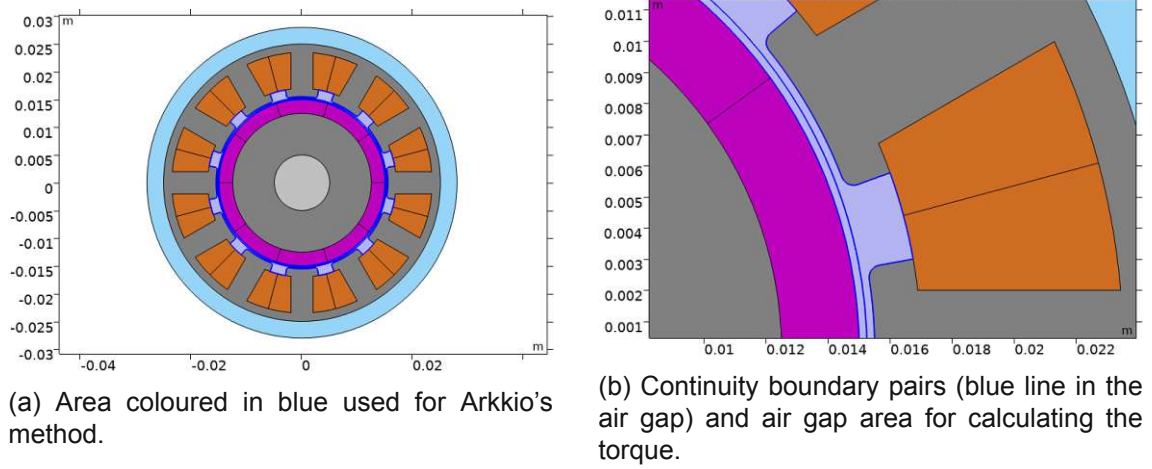


Figure 5.14: Radii shown that are used for Arkkio's method.

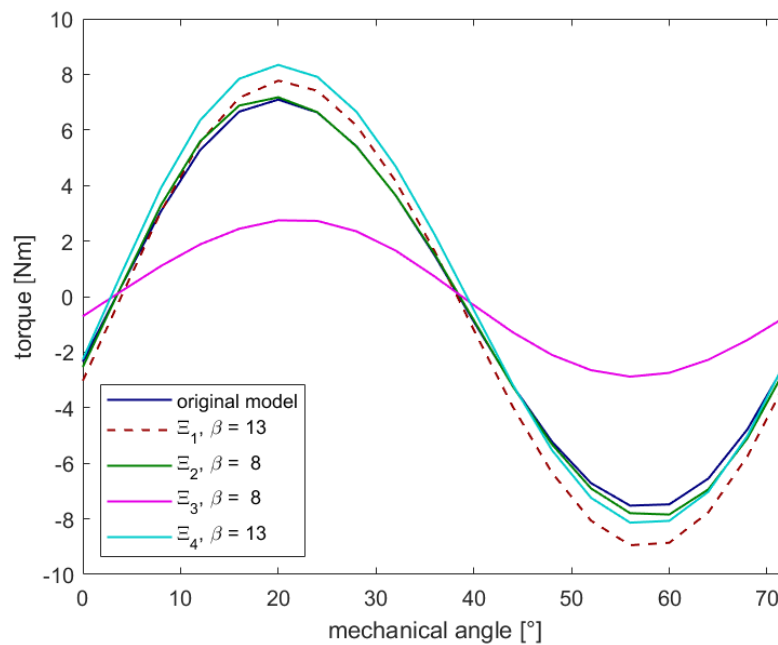


Figure 5.15: Torque plotted for the initial mechanical angle with 20° , for an angle of 72° , which refers to exactly a period of one pole pair.

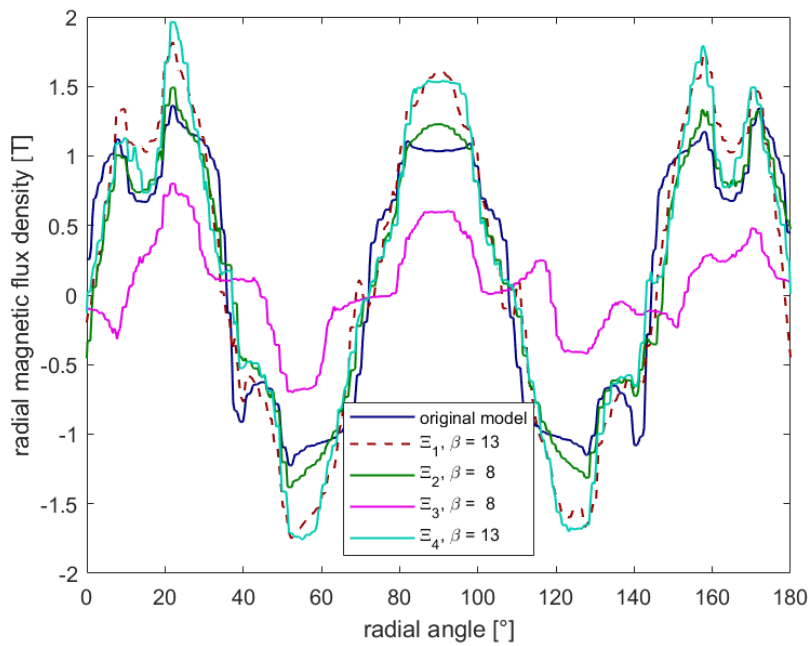


Figure 5.16: Radial component of the magnetic flux density, plotted over the arc length along the continuity line between rotor and stator, demonstrated as radial angle on the x-axis, for time $t = 0$ [52].

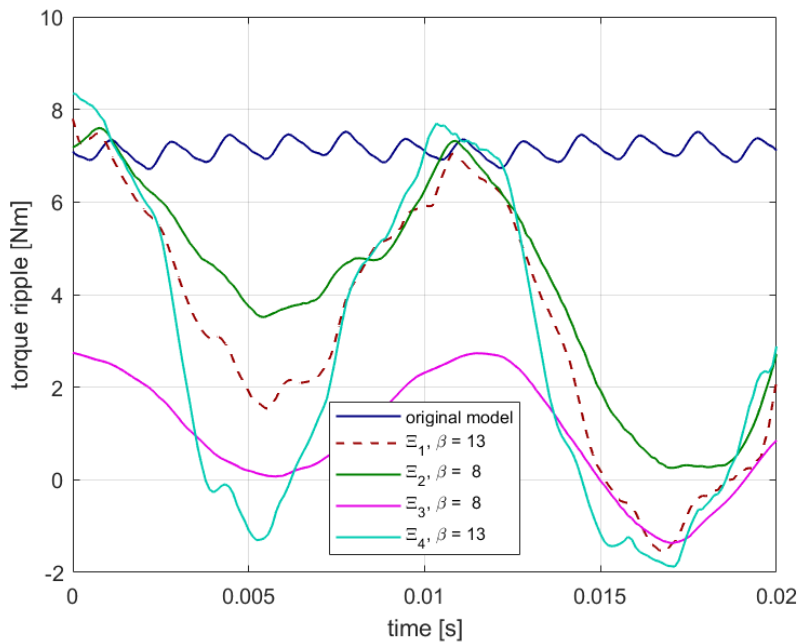


Figure 5.17: Torque plotted over one electrical period, here demonstrated as a function of time on the x-axis [52].

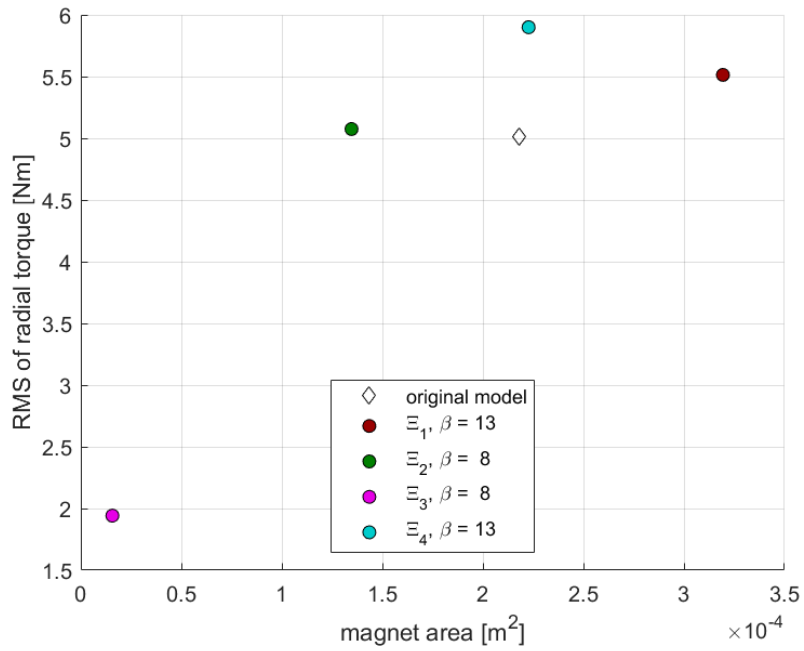
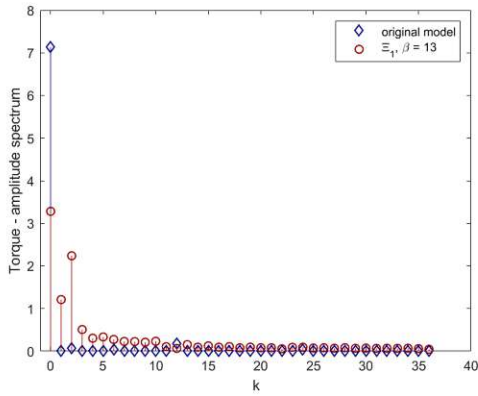
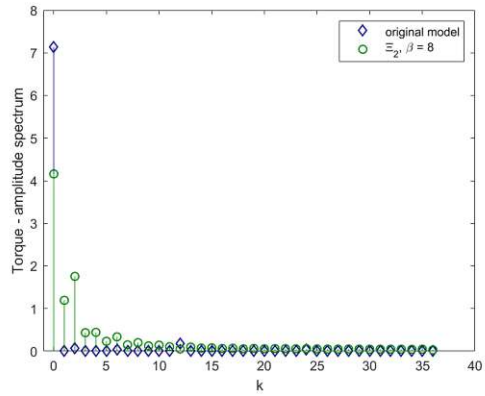


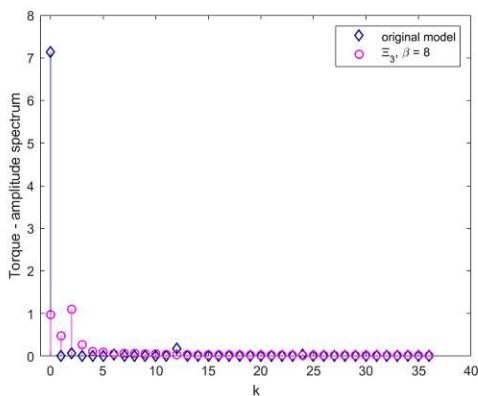
Figure 5.18: RMS calculation of torque of initial angle 20° for mechanical angle, plotted over the magnet area of the different models.



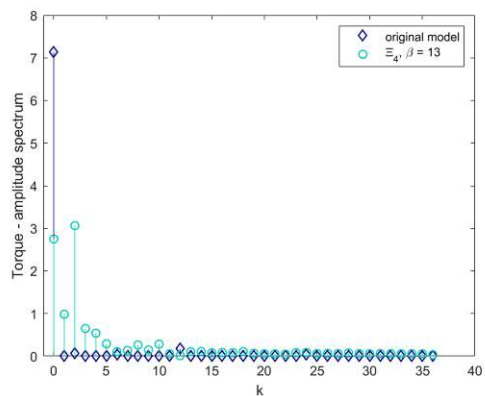
(a) Ξ_1 , projection slope $\beta = 13$.



(b) Ξ_2 , projection slope $\beta = 8$.



(c) Ξ_3 , projection slope $\beta = 8$.



(d) Ξ_4 , projection slope $\beta = 13$.

Figure 5.19: Plots of all observed cases for the rotor torque harmonics, always compared with the original model in with dark blue diamond symbols. The y-axis is scaled with the sampling period in COMSOL.

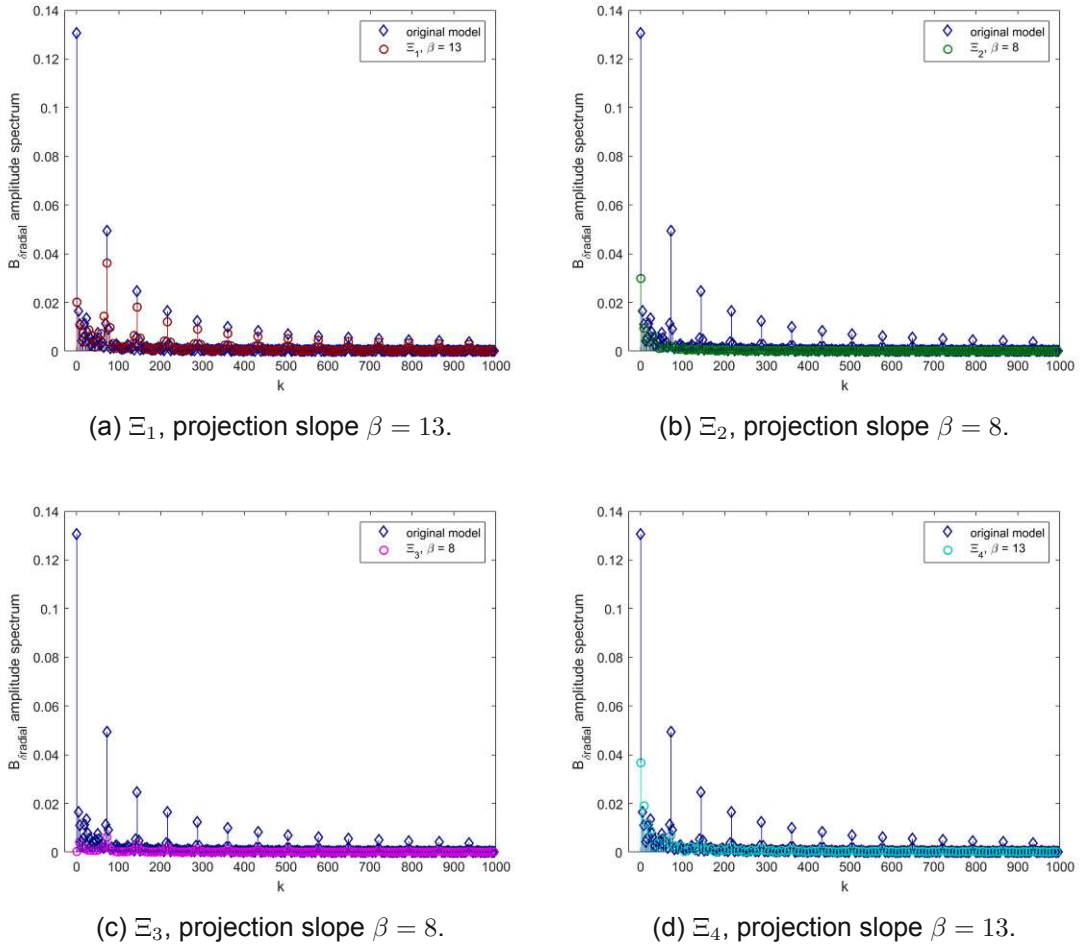


Figure 5.20: Plots of all observed cases for the rotor air gap flux density harmonics , always compared with the original model in with dark blue diamond symbols. The y-axis is scaled with the sampling period in COMSOL.

6 Conclusion and Outlook

6.1 Limitations of the thesis

Some limitations need to be mentioned here that might have influenced the outcome of this work. No other research papers in other languages than German or English were considered due to insufficient language skills. The aim for keeping the period under review reduced to the last eight years was mainly achieved, but for some basic laws of physics, no specific restrictions were made. Regarding certain scientific papers, only those that were supported by the Technical University of Vienna and Denmark or those that are publicly accessible were consulted. That specifically excludes all papers or articles where additional costs were needed and no library could have provided them.

Aside from this, another limitation was a prescribed time frame and cost limitations. Therefore it was not possible to realize a practical implementation of the model.

Besides this, efforts were made to include the recent state of research in the field of optimization methodologies for permanent magnet assemblies, but as of mentioned limitations, there might be other investigations possible for future research tasks, that are partly mentioned in 6.3.

6.2 Conclusion

This thesis presented a way of how to combine the Virtual Magnet Method and Topology Optimization. It could be shown that combining both methods lead to comparable results by using only each method separately.

With this work it could be shown that both optimization methods, which were previously only applied separately, showed combined comparable results where only each method was applied separately. By means of simplified geometries, the feasibility of the combination could be shown at the beginning. For each of the geometries investigated, other modifiable parameters were addressed. By means of changes within the default settings for the Topology Optimization, it was specifically observed whether there were changes in the results compared to the basic settings. Thus, the optimization solver MMA was examined for both variants SIMP and RAMP. Since both have a different way of using an iterative convergence procedure for a given design space and material distribution, very different results were obtained for some applications, e.g. for magnetic refrigeration.

In addition, some parameters had stronger effects on the change in the result than others, such as varying β , as it mainly influenced the gray-scaling. Other parameters had less influence when changing them, for example the initial value for the control variable θ , θ_0 did not bring any improvement. As well, θ_β and θ_{min} was used with its default value, as varying these two parameters too far away from the given value only made the iterative process ending with no useful results.

However, adapting the upper boundaries for maximum iteration number sometimes lead to varying solutions, as well as setting the optimality tolerance smaller to 0.001 helped improving. Changing the mesh set-up for specific areas within the observed geometries also helped to get different magnet shapes, as examined for the simplified motor model in chapter 4, as well as minimizing the plateaus in the objectives plotted over the iterations.

Using these findings from the simplified geometries, an attempt was made to apply both methods combined to a 2D model of an electrical machine in COMSOL Multiphysics to see if the application of both methods can result in a plausible rotor design. Thus, it could

be shown that aspects in Table 1 from [8] could thus be combined, as mentioned in chapter 1.

By combining both methods, it was possible to create different optimized magnet shapes for the motor model and at the same time to calculate the magnetization of those magnets. The results in chapter 5 were similar to the original model with respect to the magnetic flux density curve in the air gap, but with respect to the RMS of the torque, higher values could be achieved with some models, with partially reduced magnet material, like presented in figure 5.18.

From these results it can be concluded that the combination of both methods can definitely be applied to other geometries. If extensions are made as suggested in the next section, it can certainly be applied to other objects with permanent magnets.

6.3 Outlook

A number of recommendations for future research can be given here, as a matter of time, not every aspect could have been investigated with proper detail.

As already mentioned at the introduction chapter, as stated for many applications in [4], reducing the dependency of China's almost monopoly for permanent magnet market, it can be interesting to investigate ways to reduce the amount of material needed to still fulfill the objectives, but leave out any additional parts. Aside of this dependency, it is of great interest to reuse already used permanent magnets again. Very clear ideas of how to reuse permanent magnets of synchronous machines is given in [55]. Combining the idea of analysing the motor with finite element method there, but instead using the approach of the combination of both methods as within the thesis, it could be of great interest to see results when using approaches of [56]. In this work one part focused on designing a structure out of the model without adapting to predefined shapes or considering limitations in the manufacturing process. Hence there could be more degrees of freedom in terms of reusing magnets out of damaged motors and reusing them by simultaneously creating new advanced shapes, as using them in form of segmented magnets. This provides a good starting point to include concepts of using the printed frame in [56] for individual shapes of magnets by creating soft magnetic composites out of used permanent magnets. There might be a possibility to influence the amount of powdered magnet material by adding recycled polymers to it and fill it within the desired frame.

It is a question of future research to think of including complete new material that results in similar behaviour than permanent magnets to save further excavation of rare earth elements. One concrete example would be the synthetically generated alloy of nickel iron, called *tetrataenite*. It occurs within meteorites, where over millions of years a cooling process rearranges the crystal lattice of nickel and iron, stacking in a certain sequence so that magnetic characteristics are built up. Even though efforts were made in the 1960's to generate tetrataenite artificially, but did not work for mass production. By using phosphorus now, the process turned into a less cost-effective and complex [57].

Future research on using the Virtual Magnet Method as the segmented approach combined with Topology Optimization could be combined well with the proposal in the former paragraph to define certain magnet blocks, each of them magnetized differently, and then optimized with different varieties of Topology Optimization, as this thesis only examines the density approach.

Furthermore, other aspects of optimization can be considered, e.g. using three-dimensional models, including other physical parameters like acoustic phenomena or additional thermal losses that occur, specifically during continuous rating of electrical machines. As

stated in [58], the strong dependency of high temperatures and demagnetisation can drive investigations within optimized cooling system, as it clearly showed improvements.

Future research could as well include to research on building prototypes, e.g. for electrical machines and the designed rotor, to test the simulated motor and verify results for real life circumstances. Those aspect might be interesting to test within environments such as new models of wind turbines, as explained in [59]. An unconventional type of turbines with vertical axis rotation instead of horizontal axis rotation, but implying centrifugal force shutters, it might be of great interest to investigate a diverse rotor for this type of wind power plant.

Bibliography

- [1] Malcolm. McCaig. *Permanent magnets in theory and practice / Malcolm McCaig and Alan G. Clegg*. eng. 2nd ed. New York: Wiley, 1987. ISBN: 0470210036.
- [2] J.M.D. Coey. "Permanent magnetism". In: *Solid State Communications* 102.2-3 (Apr. 1997), pp. 101–105. ISSN: 00381098. DOI: 10.1016/S0038-1098(96)00712-0.
- [3] J.M.D. Coey. "Permanent magnet applications". In: *Journal of Magnetism and Magnetic Materials* 248.3 (Aug. 2002), pp. 441–456. ISSN: 03048853. DOI: 10.1016/S0304-8853(02)00335-9.
- [4] John Ormerod. "Permanent magnet markets and applications". In: *Modern Permanent Magnets*. Elsevier, 2022, pp. 403–434. DOI: 10.1016/B978-0-323-88658-1.00012-1.
- [5] A. R. Insinga et al. "Globally Optimal Segmentation of Permanent-Magnet Systems". In: *Physical Review Applied* 5.6 (June 2016), p. 064014. ISSN: 2331-7019. DOI: 10.1103/PhysRevApplied.5.064014.
- [6] A. R. Insinga et al. "Optimally Segmented Permanent Magnet Structures". In: *IEEE Transactions on Magnetics* 52.12 (Dec. 2016), pp. 1–6. ISSN: 0018-9464. DOI: 10.1109/TMAG.2016.2593685.
- [7] Thomas Forrister. *Simulation applications streamline the development of electrical vehicles*. Kassel, Dec. 2019. URL: https://www.comsol.de/story/download/677341/VW_MS19.pdf.
- [8] A.R. Insinga et al. "Optimal Segmentation of Three-Dimensional Permanent-Magnet Assemblies". In: *Physical Review Applied* 12.6 (Dec. 2019), p. 064034. ISSN: 2331-7019. DOI: 10.1103/PhysRevApplied.12.064034.
- [9] Siegmund Brandt and Hans Dieter Dahmen. *Elektrodynamik*. 4th ed. Berlin/Heidelberg: Springer-Verlag, 2005. ISBN: 3-540-21458-5. DOI: 10.1007/b138039.
- [10] Theodore Frankel. *The Geometry of Physics*. 3rd. Cambridge University Press, Nov. 2011. ISBN: 9781107016736. DOI: 10.1017/CBO9781139061377.
- [11] Adalbert Prechtl. *Vorlesungen ueber Elektrodynamik*. Vienna, 2010.
- [12] Andy Wolski. *Theory of Electromagnetic Fields*. June 2010. URL: <https://cas.web.cern.ch/sites/default/files/lectures/ebeltoft-2010/wolski-2.pdf>.
- [13] John David Jackson. *Classical Electrodynamics*. Illinois: John Wiley & Sons, Inc., Jan. 1962.
- [14] Adolf J. Schwab. *Begriffswelt der Feldtheorie*. 7th ed. Berlin, Heidelberg: Springer Berlin Heidelberg, 2013. ISBN: 978-3-642-34565-4. DOI: 10.1007/978-3-642-34566-1.
- [15] Izaak Neutelings. *Magnetic field of a current-carrying wire*. Mar. 2020. URL: https://tikz.net/magnetic_field_wire/.
- [16] Adolf J. Schwab. "Types of Vector Fields". In: *Field Theory Concepts*. Berlin, Heidelberg: Springer Berlin Heidelberg, 1988, pp. 15–18. DOI: 10.1007/978-3-642-48941-9{_}2.
- [17] Ao.Univ.Prof. DI Dr. Erich Schmidt. *Numerical Analysis of Electrical Machines and Devices*. Vienna, Oct. 2020.
- [18] COMSOL. *AC/DC Module User's Guide*. 2018. URL: <https://doc.comsol.com/5.4/doc/com.comsol.help.acdc/ACDCModuleUsersGuide.pdf>.
- [19] Jack Vanderlinde. *Classical Electromagnetic Theory*. 2nd ed. Dordrecht: Springer Netherlands, 2005, pp. XV–420. ISBN: 978-1-4020-2699-7. DOI: 10.1007/1-4020-2700-1.

- [20] Ao.Univ. Prof. Dr. Erich Schmidt. *Elektrische Maschinen*. TU Wien, Institut fuer Energiesysteme und elektrische Antriebe, 2021.
- [21] A. Wolski. "Maxwell's equations for magnets". In: *Proceedings of the CAS–CERN Accelerator School: Magnets*. Ed. by D. Brandt. Bruges, Belgium: CERN-2010-004, June 2009, pp. 1–38.
- [22] Th. Zickler. "Basic design and engineering of normal-conducting, iron-dominated electromagnets". In: *Proceedings of the CAS–CERN Accelerator School: Magnets*. Ed. by D. Brandt. Bruges, Belgium: CERN-2010-004, June 2009, pp. 65–102.
- [23] Gerhard Fasching. *Werkstoffe für die Elektrotechnik*. 4th ed. Vienna: Springer-Verlag, 2005. ISBN: 3-211-22133-6. DOI: 10.1007/b138728.
- [24] Adalbert Prechtel. *Vorlesungen über die Grundlagen der Elektrotechnik*. 2nd ed. Vienna: Springer Vienna, 2007. ISBN: 978-3-211-72455-2. DOI: 10.1007/978-3-211-72456-9.
- [25] Izaak Neutelings. *Magnetization of matter & hysteresis*. Mar. 2020. URL: <https://tikz.net/magnetization/>.
- [26] Izaak Neutelings. *Magnetization Plots*. Feb. 2020. URL: https://tikz.net/magnetization_plots/.
- [27] Andreas Binder. *Elektrische Maschinen und Antriebe*. Berlin, Heidelberg: Springer Berlin Heidelberg, 2017. ISBN: 978-3-662-53240-9. DOI: 10.1007/978-3-662-53241-6.
- [28] Benjamin Loubet. *Finding a Structure's Best Design with Topology Optimization*. Sept. 2015. URL: <https://www.comsol.de/blogs/finding-a-structures-best-design-with-topology-optimization/>.
- [29] Hanna Gothäll. *How to Use Topology Optimization Results as Model Geometries*. Jan. 2020. URL: <https://www.comsol.com/blogs/how-to-use-topology-optimization-results-as-model-geometries/>.
- [30] Ashok Dara, M. V. A. Raju Bahubalendruni, and A. Johnney Mertens. "Does Topology Optimization Exist in Nature?" In: *National Academy Science Letters* 45.1 (Feb. 2022), pp. 69–73. ISSN: 0250-541X. DOI: 10.1007/s40009-021-01050-1.
- [31] R. Bjørk and A.R. Insinga. "A topology optimized switchable permanent magnet system". In: *Journal of Magnetism and Magnetic Materials* 465 (Nov. 2018), pp. 106–113. ISSN: 03048853. DOI: 10.1016/j.jmmm.2018.05.076.
- [32] Ole Sigmund and Kurt Maute. "Topology optimization approaches". In: *Structural and Multidisciplinary Optimization* 48.6 (Dec. 2013), pp. 1031–1055. ISSN: 1615-147X. DOI: 10.1007/s00158-013-0978-6.
- [33] Martin P. Bendsøe and Ole Sigmund. *Topology Optimization*. Berlin, Heidelberg: Springer Berlin Heidelberg, 2004. ISBN: 978-3-642-07698-5. DOI: 10.1007/978-3-662-05086-6.
- [34] R. Bjørk et al. "Optimization and improvement of Halbach cylinder design". In: *Journal of Applied Physics* 104.1 (July 2008), p. 013910. ISSN: 0021-8979. DOI: 10.1063/1.2952537.
- [35] R. Bjørk, C.R.H. Bahl, and A.R. Insinga. "Topology optimized permanent magnet systems". In: *Journal of Magnetism and Magnetic Materials* 437 (Sept. 2017), pp. 78–85. ISSN: 03048853. DOI: 10.1016/j.jmmm.2017.04.028.
- [36] J. H. Jensen and M. G. Abele. "Maximally efficient permanent magnet structures". In: *Journal of Applied Physics* 79.2 (1996), p. 1157. ISSN: 00218979. DOI: 10.1063/1.360914.
- [37] Kristian Ejlebjærg Jensen. *Performing Topology Optimization with the Density Method*. Jan. 2019. URL: <https://www.comsol.com/blogs/performing-topology-optimization-with-the-density-method/>.

- [38] Walter Frei. *Using Data Filtering to Improve Model Performance*. Mar. 2021. URL: <https://www.comsol.de/blogs/using-data-filtering-to-improve-model-performance/>.
- [39] R. Rezaie et al. "Topology Optimization for Fused Deposition Modeling Process". In: *Procedia CIRP* 6 (2013), pp. 521–526. ISSN: 22128271. DOI: 10.1016/j.procir.2013.03.098.
- [40] Jaewook Lee et al. "Topology optimization for design of segmented permanent magnet arrays with ferromagnetic materials". In: *Journal of Magnetism and Magnetic Materials* 449 (Mar. 2018), pp. 571–581. ISSN: 03048853. DOI: 10.1016/j.jmmm.2017.10.109.
- [41] F. Saeidi et al. "Magnet design for an ultralow emittance storage ring". In: *Physical Review Accelerators and Beams* 19.3 (Mar. 2016), p. 032401. ISSN: 2469-9888. DOI: 10.1103/PhysRevAccelBeams.19.032401.
- [42] Masako Yamada et al. "Pulsed neutron-beam focusing by modulating a permanent-magnet sextupole lens". In: *Progress of Theoretical and Experimental Physics* 2015.4 (Apr. 2015). ISSN: 2050-3911. DOI: 10.1093/ptep/ptv015.
- [43] Jack T Tanabe. *Iron Dominated Electromagnets: Design, Fabrication, Assembly And Measurements*. WORLD SCIENTIFIC, May 2005. ISBN: 978-981-256-327-9. DOI: 10.1142/5823.
- [44] Daniel Brandt. "Proceedings of the 2009 CAS-CERN Accelerator School: Specialised course on Magnets, Bruges, Belgium, 16 - 25 Jun 2009". In: (May 2011).
- [45] Andrea Roberto Insinga. "Optimising Magnetostatic Assemblies". PhD thesis. Technical University of Denmark, 2016.
- [46] R. Bjork et al. "Improving Magnet Designs With High and Low Field Regions". In: *IEEE Transactions on Magnetics* 47.6 (June 2011), pp. 1687–1692. ISSN: 0018-9464. DOI: 10.1109/TMAG.2011.2114360.
- [47] Christian Wollblad. *Your Guide to Meshing Techniques for Efficient CFD Modeling*. June 2018. URL: <https://www.comsol.com/blogs/your-guide-to-meshing-techniques-for-efficient-cfd-modeling/>.
- [48] COMSOL Learning Center. *Basics of Meshing*. 2018. URL: <https://www.comsol.com/video-training/getting-started/building-the-mesh-for-a-model-geometry-in-comsol-multiphysics>.
- [49] Mohammad Farshadnia. *Advanced Theory of Fractional-Slot Concentrated-Wound Permanent Magnet Synchronous Machines*. Singapore: Springer Singapore, 2018. ISBN: 978-981-10-8707-3. DOI: 10.1007/978-981-10-8708-0.
- [50] Rolf Fischer. *Elektrische Maschinen*. Vol. 14. Muenchen: Hanser, 2009.
- [51] Rahul Bhat. *Analyzing Electric Motor and Generator Designs with COMSOL®*. Feb. 2021. URL: <https://www.comsol.com/blogs/analyzing-electric-motor-and-generator-designs-with-comsol/>.
- [52] COMSOL Application Gallery. *Permanent Magnet Motor in 2D*. 2023. URL: https://www.comsol.com/model/download/1032531/models.acdc.pm_motor_2d_introduction.pdf.
- [53] Xiaokun Zhao et al. "Optimization Design and Performance Analysis of a Reverse-Salient Permanent Magnet Synchronous Motor". In: *Machines* 10.3 (Mar. 2022), p. 204. ISSN: 2075-1702. DOI: 10.3390/machines10030204.
- [54] COMSOL doc. *Computing Electromagnetic Forces and Torques*. 2021. URL: <https://doc.comsol.com/6.0/doc/com.comsol.help.acdc/acdc Ug modeling.06.20.html#595010>.
- [55] Zheng Li et al. "Recycling and remanufacturing technology analysis of permanent magnet synchronous motor". In: *Clean Technologies and Environmental Policy* 24.6 (Aug. 2022), pp. 1727–1740. ISSN: 1618-954X. DOI: 10.1007/s10098-022-02279-0.

- [56] Taehoon Jung, Jaejoon Lee, and Jaewook Lee. “Design and Fabrication of Magnetic System Using Multi-Material Topology Optimization”. In: *IEEE Access* 9 (2021), pp. 8649–8658. ISSN: 2169-3536. DOI: 10.1109/ACCESS.2021.3049271.
- [57] Yurii P. Ivanov et al. “Direct Formation of Hard Magnetic Tetrataenite in Bulk Alloy Castings”. In: *Advanced Science* 10.1 (Jan. 2023). ISSN: 2198-3844. DOI: 10.1002/advs.202204315.
- [58] Meiwei Zhang et al. “Health diagnosis of permanent magnets under different cooling system effectiveness in high-speed permanent magnet motors for electric vehicles”. In: *Journal of Power Electronics* 23.3 (Mar. 2023), pp. 533–542. ISSN: 1598-2092. DOI: 10.1007/s43236-022-00547-2.
- [59] Pia Gärtner. *Jungforscher für emissionslose Windturbine ausgezeichnet*. Vienna, Mar. 2023. URL: <https://www.derstandard.at/story/2000143792706/burgenlaenderjungforscher-fuer-vertikale-windturbine-ausgezeichnet>.

List of Figures

2.1	Cylinder with surface area A and normal vector \hat{n} defines the boundary conditions for B , the bottom rectangle for H with the perpendicular vector \hat{s} [13]	6
2.2	Example for an irrotational field H caused by the direct current I , depending on the distance vector r from the wire. Figure adapted from [14] and [15].	7
2.3	Schematic figure for representing the magnetic vector potential A and the relation to the vector field B [14].	8
2.4	Schematic figure of MH curve and significant marks, adaption from figure in [23], [25]	13
2.5	Approximated behaviour of ferromagnetic material, figures adapted from [23] and [26]	14
2.6	Hysteresis curve for rare-earth permanent magnets, adapted from [27]. . .	15
3.1	Virtual Magnet Method applied on the circular area for an optimized field in the y direction over an averaged field in the inner circle [8]	19
4.1	Schematic explanation of area correlation for Virtual Magnet Method [5] . .	23
4.2	Illustration of the analytical solution of the Helmholtz filter equation by a one-dimensional Heaviside function [37]	25
4.3	This figure represents an MBB (Messerschmitt-Bolkow-Blohm) beam. The left side displays the not-filtered control variable θ_f , the right side shows the filtered θ_f [37], [39]	25
4.4	This figure represents an MBB (Messerschmitt-Bolkow-Blohm) beam. The left side displays the filtered control variable θ_f , the right side shows θ with reduced gray-scaling [37], [39].	26
4.5	Illustration of the analogon to the Hilbert space expressions	27
4.6	This schematic figure serves as a model for the sextupole magnet [6]. The orange area in the middle defines the virtual magnet, the blue circle around represents the design area, in this case the real permanent magnet. The circle segment should demonstrate the sector that is used for applying Topology Optimization Method for the two models, as a symmetric object is observed. The proper boundary conditions are mentioned for the sector sides.	29
4.7	Ideal field distribution for the skewed field in the region R_g of a sextupole magnet with switched signs for x and y component to adjust the plots between topology optimization and virtual magnet method results.	30
4.8	Mesh setup for applying Virtual Magnet Method. A refinement number of 3 was applied to the areas that are analysed.	30
4.9	Sextupole Magnet optimized in permanent magnet material usage with the Virtual Magnet Method for a skewed field. The contour plot, here demonstrated with grey-colored lines, represent the z -component of the magnetic vector potential A_z . The black arrows demonstrate the magnetic flux density within the design area in its x and y direction. The colour bar serves as a demonstration of the norm of the magnetic flux density, given in Tesla.	31

4.10	Sextupole Magnet optimized in permanent magnet material usage with the Virtual Magnet Method for a skewed field, however with a hexagonal shape inside for the virtual magnet area R_g . The contour plot, here demonstrated with grey-colored lines, represent the z-component of the magnetic vector potential A_z . The black arrows demonstrate the magnetic flux density within the design area in its x and y direction. The colour bar serves as a demonstration of the norm of the magnetic flux density, given in Tesla.	32
4.11	A cutout of the skewed field is shown here. The contour plot, here demonstrated with grey-colored lines, represent the z-component of the magnetic vector potential A_z . The green arrows are covered by the blue arrows, the red arrows are too small to be shown within the same scaling.	33
4.12	Mesh setup for applying Topology Optimization Method for the 30° sector for Sextupole design. A refinement number of 2 was applied to the areas that are analysed, the iron core around the design area was not taken into account.	33
4.13	Sextupole Magnet analysed with the Topology Optimization Method with SIMP algorithm: The colour bar serves as a demonstration of the norm of the magnetic field, given in Tesla. The black arrows in cone-shape show the plotted objective function in the region R_g . The white arrows represent the remanence flux density of the magnetic field in the design area R_m . The projection point $\theta_\beta = 0.5$ and the initial value for the control variable was set to $\theta_0 = 0.5$ were used for all cases.	44
4.14	Sextupole Magnet analysed with the Topology Optimization Method with SIMP algorithm: The colour bar here serves as the indicator between magnet material above 0.5 and iron under this threshold level.	45
4.15	Objective function evaluations plotted over the total iterations made for the individual cases that were mentioned in table 4.2.	46
4.16	This schematic figure serves as a model for the quadrupole and sextupole magnet [6]. The orange area in the middle defines the virtual magnet, the blue circle around represents the design area, in this case the real permanent magnet, and the grey square around serves as an iron yoke. The circle segment should demonstrate the sector that is used for applying Topology Optimization Method for the two models, as a symmetric object is observed. The proper boundary conditions are mentioned for the sector sides.	46
4.17	Ideal not-skewed field distribution in the center of the quadrupole magnet geometry. To have a comparison to the plots with TOM, for the y component a minus sign was added to let the field arrows point inwards the inner circle.	47
4.18	Mesh setup for Virtual Magnet Method for the quadrupole geometry. As of symmetry reasons, not the whole geometry is shown here. The refinement number of 3 was applied on the areas R_g and R_m	47
4.19	Quadrupole Magnet optimized in permanent magnet material usage with the Virtual Magnet Method for a not-skewed field. The contour plot, here demonstrated with grey-colored lines, represent the z-component of the magnetic vector potential A_z . The black arrows demonstrate the magnetic flux within the design area in its x and y direction. The colour bar serves as a demonstration of the norm of the magnetic flux density, given in Tesla.	48

4.20	Quadrupole Magnet optimized in permanent magnet material usage with the Virtual Magnet Method for a not-skewed field for a pentagonal shaped R_g . The contour plot, here demonstrated with grey-colored lines, represent the z-component of the magnetic vector potential A_z . The black arrows demonstrate the magnetic flux within the design area in its x and y direction. The colour bar serves as a demonstration of the norm of the magnetic flux density, given in Tesla.	48
4.21	A cutout of the not-skewed field of the circular R_g in figure 4.21a and of the pentagonal shaped R_g in figure 4.21b. The contour plot, here demonstrated with grey-colored lines, represent the z-component of the magnetic vector potential A_z	49
4.22	Comparison of virtual magnet method results with uniform field distribution. As the previous example, a pentagonal virtual magnet area was chosen to show the limits of the method.	49
4.23	Mesh setup for applying Topology Optimization Method for the 45° sector for the quadrupole design. A refinement number of 2 was applied to the areas that are analysed, the iron core around the design area was not taken into account.	50
4.24	Quadrupole Magnet analysed with the Topology Optimization Method with SIMP algorithm: The colour bar serves as a demonstration of the norm of the magnetic field, given in Tesla. The red arrows show the plotted objective function in the region R_g . The white arrows represent the remanence flux density of the magnetic field in the design area R_m . The projection point $\theta_\beta = 0.5$ and the initial value for the control variable was set to $\theta_0 = 0.5$ were used for all cases.	51
4.25	Quadrupole Magnet analysed with the Topology Optimization Method with SIMP algorithm: The colour bar here serves as the indicator between magnet material above 0.5 and iron under this threshold level.	52
4.26	Objective function evaluations plotted over the total iterations made for the individual cases that were mentioned in table 4.4.	53
4.27	This schematic figure serves as a model for magnet refrigeration [6]. The orange areas on the sides define the virtual magnet, the blue circle around represents the design area, in this case the real permanent magnet, and the grey circle in the middle serves as the iron core.	53
4.28	Mesh defined for analysis in 4.28a, 4.28b and ideal field plot.	54
4.29	Magnetic refrigeration optimized in permanent magnet material usage with the Virtual Magnet Method. The contour plot, here demonstrated with grey-colored lines, represent the z-component of the magnetic vector potential A_z . The black arrows demonstrate the magnetic flux within the design area in its x and y direction. The colour bar serves as a demonstration of the norm of the magnetic flux density, given in Tesla.	55
4.30	Mesh setup for applying Topology Optimization Method for the 90° sector for magnetic refrigeration design. A refinement number of 2 was used here as well.	55
4.31	Magnetic refrigeration analysed with Topology Optimization Method with SIMP algorithm and the combination with VMM. The colour bar serves as a demonstration of the norm of the magnetic field, given in Tesla. The black arrows represent the flux density of the magnetic field in the design area R_m . The projection point θ_β and initial value for the control variable θ_0 were set to 0.5 and used for all cases.	56

4.32	Magnetic flux density plots for the observed cases mentioned in table 4.6 for the VMM, the SIMP algorithm and the combined approaches. The plots were taken along the middle line displayed in figure 4.28c and 4.29b. $p_{SIMP} = def$ means the predefined value which is automatically set by COMSOL and the angle θ is defined at the high field region direction and counting counterclockwise.	57
4.33	Objective plots for the observed cases mentioned in table 4.6 for the SIMP algorithm.	57
4.34	Magnet shape for magnetic refrigeration analysed with Topology Optimization Method with SIMP algorithm and the combination with VMM.	58
4.35	Magnetic refrigeration analysed with Topology Optimization Method with RAMP algorithm and the combination with VMM. The colour bar in 4.31 serves as a demonstration of the norm of the magnetic field, given in Tesla. The black arrows represent the flux density of the magnetic field in the design area R_m . The projection point θ_β and initial value for the control variable θ_0 were set to 0.5 and used for all cases.	59
4.36	Magnet shape for magnetic refrigeration analysed with Topology Optimization Method with RAMP algorithm and the combination with VMM.	60
4.37	Magnetic flux density plots for the observed cases mentioned in table 4.7 for the VMM, the RAMP algorithm and the combined approaches. The plots were taken along the middle line displayed in figure 4.28c and 4.29b, defining the angle θ at the high field region direction and counting counterclockwise.	61
4.38	Objective plots for the observed cases mentioned in table 4.7 for the RAMP algorithm.	61
4.39	Schematic for simple electric motor model, inspired by the motor model of [5].	62
4.40	Ideal field distribution for simple motor model, plotted within the region of R_g	62
4.41	Mesh setup for Virtual Magnet Method for simple motor model. The refinement of the mesh was done within the areas R_g and R_m	62
4.42	Simplified motor model optimized in permanent magnet material usage with the Virtual Magnet Method. The contour plot, here demonstrated with grey-colored lines, represent the z-component of the magnetic vector potential A_z . The black arrows demonstrate the magnetic flux within the design area in its x and y direction. The colour bar serves as a demonstration of the norm of the magnetic flux density, given in Tesla.	63
4.43	Mesh refinement number 1.	63
4.44	Simple Motor model analysed with Topology Optimization Method with a mesh refinement number of 1 and the combination with VMM. The colour bar serves as a demonstration of the norm of the magnetic field, given in Tesla. The black arrows represent the remanent flux density of the magnetic field in the design area R_m as they could not be illustrated in white because of visibility on the colour-bar. The cone-shaped arrows represent the desired field in region R_g . The projection point θ_β and initial value for the control variable θ_0 were set to 0.5 and used for all cases.	64
4.45	Total radial component of radial magnetic flux density - plots for the observed cases mentioned in table 4.9 for the mesh refinement number 1.	65
4.46	First harmonic of the radial component of radial magnetic flux density - plots for the observed cases mentioned in table 4.9 for the mesh refinement number 1.	65

4.47	Residuals of the radial component of radial magnetic flux density - plots for the observed cases mentioned in table 4.9 for the mesh refinement number 1.	66
4.48	Objective plots for the observed cases mentioned in table 4.9 for the mesh refinement number 1.	66
4.49	Relative error plots for the observed cases mentioned in table 4.9 for the mesh refinement number 1.	67
4.50	Simple Motor model analysed with Topology Optimization Method with a mesh refinement number of 1 and the combination with VMM. The colour bar serves as a demonstration of the magnet and iron area with the threshold of 0.5. The projection point θ_β and initial value for the control variable θ_0 were set to 0.5 and used for all cases.	68
4.51	Mesh refinement number 2.	69
4.52	Simple Motor model analysed with Topology Optimization Method with a mesh refinement number of 2 and the combination with VMM. The colour bar serves as a demonstration of the norm of the magnetic field, given in Tesla. The black arrows represent the remanent flux density of the magnetic field in the design area R_m as they could not be illustrated in white because of visibility on the colour-bar. The cone-shaped arrows represent the desired field in region R_g . The projection point θ_β and initial value for the control variable θ_0 were set to 0.5 and used for all cases.	70
4.53	Total radial component of radial magnetic flux density - plots for the observed cases mentioned in table 4.10 for the mesh refinement number 2.	71
4.54	First harmonic of the radial component of radial magnetic flux density - plots for the observed cases mentioned in table 4.10 for the mesh refinement number 2.	71
4.55	Residuals of the radial component of radial magnetic flux density - plots for the observed cases mentioned in table 4.10 for the mesh refinement number 2.	72
4.56	Objective plots for the observed cases mentioned in table 4.10 for the mesh refinement number 2.	72
4.57	Relative error plots for the observed cases mentioned in table 4.10 for the mesh refinement number 2.	73
4.58	Simple Motor model analysed with Topology Optimization Method with a mesh refinement number of 1 and the combination with VMM. The colour bar serves as a demonstration of the magnet and iron area with the threshold of 0.5. The projection point θ_β and initial value for the control variable θ_0 were set to 0.5 and used for all cases.	74
5.1	Overview over different types of synchronous machines and their relation between their inductance [20].	76
5.2	Magnetic circuit representing a simplified machine model [27].	76
5.3	Model for 6 pole embedded permanent magnet rotor with axes d, q [49],[20].	78
5.4	Schematic figure for PM rotor optimization.	79
5.5	Sector plots of all observed cases for the rotor model. The black arrows this time show the magnetization that resulted from the Virtual Magnet Method. The contour line signifies the boundary between iron and magnet area.	84
5.6	Objectives of designed rotor models, plotted over iterations.	85
5.7	Relative error plots of objective 1 and 2, for better visibility it was plotted separately from the other two error plots.	85

5.8	Relative error plots of objective 3 and 4, for better visibility it was plotted separately from the other two error plots.	86
5.9	2D - permanent magnet motor model in COMSOL, taken from [51].	86
5.10	BH curve for the soft iron used in the COMSOL model.	87
5.11	Comparing magnet shape (in magenta) within designed rotor , implemented in the motor model, with original model.	88
5.12	Comparing field plots of stationary analysis of original model with imported rotor models, at $t = 0$	89
5.13	Comparing field plots of stationary analysis of original model with imported rotor models by more detailed plot, at $t = 0$	90
5.14	Radii shown that are used for Arkkio's method.	91
5.15	Torque plotted for the initial mechanical angle with 20° , for an angle of 72° , which refers to exactly a period of one pole pair.	91
5.16	Radial component of the magnetic flux density, plotted over the arc length along the continuity line between rotor and stator, demonstrated as radial angle on the x-axis, for time $t = 0$ [52].	92
5.17	Torque plotted over one electrical period, here demonstrated as a function of time on the x-axis [52].	92
5.18	RMS calculation of torque of initial angle 20° for mechanical angle, plotted over the magnet area of the different models.	93
5.19	Plots of all observed cases for the rotor torque harmonics, always compared with the original model in with dark blue diamond symbols. The y-axis is scaled with the sampling period in COMSOL.	94
5.20	Plots of all observed cases for the rotor air gap flux density harmonics , always compared with the original model in with dark blue diamond symbols. The y-axis is scaled with the sampling period in COMSOL.	95

List of Tables

4.1	Chosen measurements for geometry of sextupole magnet in COMSOL. The idea of taking one sector for Topology Optimization approach was given by [40], the sizes were inspired by [41], the general geometrical shape by [42].	29
4.2	Representation of the calculated values of the multipole expansion 4.12a ,4.12c and the magnetic efficiency factor 3.6. For the analysis of TOM, the SIMP algorithm was used and changes of β and p_{SIMP} were made, the initial value $\theta_0 = 0.5$ and the projection point $\theta_\beta = 0.5$ was set by default and not changed in this case. The used optimality tolerance for TOM was 0.1, and a maximum of 100 iterations was set as a restriction.	32
4.3	Chosen measurements for geometry of quadrupole magnet in COMSOL. The idea of taking one sector for Topology Optimization approach was given by [40], the sizes were inspired by [41].	34
4.4	Representation of the calculated values of the multipole expansion 4.12a ,4.12c and the magnetic efficiency factor 3.6. For the analysis of TOM, the SIMP algorithm was used and changes of β and p_{SIMP} were made, the initial value $\theta_0 = 0.5$ and the projection point $\theta_\beta = 0.5$ was set by default and not changed in this case. The used optimality tolerance for TOM was 0.001, and a maximum of 100 iterations was set as a restriction.	35
4.5	Chosen measurements for geometry of magnetic refrigeration in COMSOL. The measurements were chosen according to [40]. The idea of taking one sector for Topology Optimization approach was given by [46].	36
4.6	Results of VMM and TOM with SIMP algorithm and combined approach. The best result regarding the tradeoff between both calculations was highlighted in yellow.	38
4.7	Results of VMM and TOM with RAMP algorithm and combined approach. The best result regarding the trade-off between both calculations was highlighted in yellow.	39
4.8	Chosen measurements for geometry of the simplified motor model in COMSOL. The measurements were chosen according to . The idea of taking one sector for Topology Optimization approach was given by [46], as it can be applied as well on a symmetric composition as it is given here.	40
4.9	Representation of the calculated figure of merit M for the mesh refinement 1 in COMSOL. For the analysis of TOM, the SIMP algorithm was used and changes of β and p_{SIMP} were made, the initial value $\theta_0 = 0.5$ and the projection point $\theta_\beta = 0.5$ was set by default and not changed in this case. The used optimality tolerance for TOM was 0.001, and a maximum of 100 iterations was set as a restriction.	41
4.10	Representation of the calculated figure of merit M for the number of mesh refinement 2 in COMSOL. The refinement process did not change any result from the virtual magnet method compared to the prior refinement number, so it only affected the results for Topology Optimization. For the latter, SIMP algorithm was used and changes of β and p_{SIMP} were made, the initial value $\theta_0 = 0.5$ and the projection point $\theta_\beta = 0.5$ was set by default and not changed in this case. The used optimality tolerance for TOM was 0.001, and a maximum of 100 iterations was set as a restriction.	42

5.1	Chosen measurements for rotor design.	79
5.2	Measurements for COMSOL geometry of the motor model [52].	80

Die approbierte gedruckte Originalversion dieser Diplomarbeit ist an der TU Wien Bibliothek verfügbar
The approved original version of this thesis is available in print at TU Wien Bibliothek.

Technical
University of
Denmark

Anker Engelunds Vej, Building 301
2800 Kgs. Lyngby
Tlf. 4525 1700

<https://www.energy.dtu.dk/>